

Single Spin Asymmetry in J/ψ Production from $p + p$, $p + \text{Al}$, and $p + \text{Au}$
Collisions with Transversely Polarized Proton Beams at $\sqrt{s_{NN}} = 200$ GeV

Chen Xu, B.S., M.S.

A dissertation submitted to the Graduate School

in partial fulfillment of the requirements

for the degree

Doctor of Philosophy

Major Subject: Physics

New Mexico State University

Las Cruces New Mexico

December 2018

“Single Spin Asymmetry in J/ψ Production from $p+p$, $p+Al$, and $p+Au$ Collisions with Transversely Polarized Proton Beams at $\sqrt{s_{NN}} = 200$ GeV,” a dissertation prepared by Chen Xu in partial fulfillment of the requirements for the degree, Doctor of Philosophy, has been approved and accepted by the following:

Loui Reyes
Dean of the Graduate School

Stephen Pate
Chair of the Examining Committee

Date

Committee in charge:

Dr. Stephen Pate, Chair

Dr. Vassili Papavassiliou

Dr. Michael Engelhardt

Dr. Hongmei Luo

DEDICATION

to Bingqing Cai

ACKNOWLEDGMENTS

I would like to thank my advisor, Stephen Pate, for his encouragement, interest, and patience. Personally, I would like to thank him for supporting me on any decisions I have made either on my researches or careers.

I would like also thank Dr. Xiaorong Wang, Dr. Jin Huang, Dr. Haiwang Yu and Dr. Vassili Papavassiliou for offering me suggestions and help for finishing my data analysis. I am grateful to my panel of committee members Dr. Michael Engelhardt and Dr. Hongmei Luo who spent their valuable time in evaluating my project.

My special thanks should be given to my wife Bingqing Cai and my daughter Jolene Xu who inspire me and offer me endless power to move forward.

ABSTRACT

SINGLE SPIN ASYMMETRY IN J/ψ PRODUCTION FROM $P + P, P + \text{AL}$,

and $P + \text{AU}$ COLLISIONS WITH TRANSVERSELY POLARIZED PROTON

BEAMS AT $\sqrt{s_{NN}} = 200$ GEV

BY

CHEN XU, B.S., M.S.

Doctor of Philosophy

New Mexico State University

Las Cruces, New Mexico, 2017

Dr. Stephen Pate, Chair

I report the transverse single-spin asymmetries in J/ψ production at forward and backward rapidity, $1.2 < |y| < 2.2$, as a function of J/ψ transverse momentum (p_T) and Feynman- x (x_F). The data analyzed were recorded by the PHENIX experiment at RHIC in 2015 from $p+p$, $p+\text{Al}$, and $p+\text{Au}$ collisions with transversely polarized proton beams at $\sqrt{s_{NN}} = 200$ GeV. At this collision energy, single-spin asymmetries for heavy-flavor particle production in $p+p$ collisions provide access to the spin-dependent gluon distribution and higher-twist correlation

functions inside the nucleon. Proton+nucleus collisions offer an excellent opportunity to study nuclear effects on the correlation functions. The data indicate negative asymmetries at the two-standard-deviation level, in the p +Au data for $p_T < 2 \text{ GeV}/c$ at both forward and backward rapidity, while in $p+p$ and $p+\text{Al}$ collisions the asymmetries are consistent with zero within the range of experimental uncertainties.

CONTENTS

LIST OF TABLES	xi
LIST OF FIGURES	xxii
1 INTRODUCTION	1
1.1 Overview	1
1.2 Quantum Chromodynamics	2
1.3 The Structure of Proton	5
1.4 Deep Inelastic Scattering	8
1.5 Unpolarized parton distribution	10
1.6 Polarized parton distributions	13
1.7 Transverse Single Spin Asymmetry	15
2 EXPERIMENT SETUP AT PHENIX	22
2.1 The Relativistic Heavy Ion Collider (RHIC)	22
2.1.1 RHIC-AGS complex	23
2.1.2 Spin Dynamics and Siberian Snakes	24
2.1.3 Polarimeters	26
2.1.4 Spin Rotators	30
2.2 PHENIX	30
2.2.1 PHENIX Magnet System	33

2.2.2	Global detectors	36
2.2.3	Central Arm Detectors	38
2.2.4	Forward arm detectors	40
3	Data and Analysis	55
3.1	Muon Arm Quality Assurance (QA)	55
3.1.1	Run selection with $p + p$ data	59
3.1.2	Run selection with $p + \text{Au}$ data	64
3.1.3	Run selection with $p + \text{Al}$ data	65
3.2	Event and Track Selection	65
3.3	J/ψ Transverse Single Spin Asymmetry	68
3.4	Background Fraction	69
3.5	Inclusive and Background A_N extraction	90
3.5.1	Maximum Likelihood method	90
3.5.2	Azimuthal Fitting method with Spin Analyzer	92
3.5.3	Maximum Likelihood method with $p + p$ data	94
3.5.4	Azimuthal Fitting method with $p + p$ collisions	95
3.5.5	Maximum Likelihood method with $p + \text{Au}$ data	98
3.5.6	Azimuthal Fitting method with $p + \text{Au}$ collisions	109
3.5.7	Maximum Likelihood method with $p + \text{Al}$ data	111
3.5.8	Azimuthal Fitting method with $p + \text{Al}$ collisions	116
3.6	Crosschecks	118

3.6.1	A crosscheck for Spin Analyzer using standalone code with $p + p$ data	119
3.6.2	Cross check for $p + \text{Au}$ data with standalone code	124
3.6.3	Fill-by-Fill A_N estimation with Maximum Likelihood method	127
3.6.4	Cross check for $p + \text{Au}$ data from other collaborators	127
3.6.5	Crosscheck with BBC counts	129
3.7	$J/\psi A_N$	133
3.8	Systematic Uncertainty Study	136
3.8.1	Shuffling result for transverse single spin asymmetry A_N .	136
3.9	Systematic uncertainty from different invariant mass fitting methods	144
3.9.1	Combining Systematic Uncertainty from different sources .	148
4	Final Result and Discussion	151
4.1	Combined result in $p + p$ data for <i>Blue</i> and <i>Yellow</i> beams	151
4.2	Finalized result for $A_N^{J/\psi}$ with Run15 data	154
4.3	Further Study on $p + \text{Au}$ data for lower p_T bin	155
4.3.1	A_N in three and four p_T bins	159
4.3.2	A_N with binning of number of FVTX Tracklets and BBC centrality	160
5	Conclusion	163
	REFERENCES	165

LIST OF TABLES

1	Parameters of hadron absorbers in MuID.	48
2	Design parameters of FVTX.	53
3	Background Fraction in p_T bins for $p + p$ data	88
4	Background Fraction in p_T bins for $p + \text{Au}$ data	88
5	Background Fraction in p_T bins for $p + \text{Al}$ data	89
6	Background Fraction in x_F bins for $p + p$ data	89
7	Background Fraction in x_F bins for $p + \text{Au}$ data	89
8	Background Fraction in x_F bins for $p + \text{Al}$ data	89
9	Blue and yellow beam polarization in $p + p$ and $p + A$ collisions. .	92
10	List of Inclusive and background A_N from Maximum Likelihood for Blue beam with $p + p$ data	96
11	List of Inclusive and background A_N from Maximum Likelihood for Yellow beam with $p + p$ data	97
12	$A_N^{Inc.}$ in different p_T and x_F bins with $p\text{Au}$ data	108
13	$A_N^{Bgr.}$ in different p_T and x_F bins with $p\text{Au}$ data	108
14	$A_N^{Inc.}$ in different p_T and x_F bins with $p + \text{Al}$ data	115
15	$A_N^{Bgr.}$ in different p_T and x_F bins with $p + \text{Al}$ data	115
16	$A_N^{J/\psi}$ in different p_T and x_F bins for Blue beam with $p + p$ data .	133

17	$A_N^{J/\psi}$ in different p_T and x_F bins for Yellow beam with $p + p$ data	134
18	$A_N^{J/\psi}$ in different p_T and x_F bins for Blue beam with $p + \text{Al}$ data .	134
19	$A_N^{J/\psi}$ in different p_T and x_F bins for Blue beam with $p + \text{Au}$ data	134
20	Background Fraction with CB + Gaussian + Pol3 for $p + p$ data .	145
21	Background Fraction with CB + Gaussian + Pol3 for $p + \text{Au}$ data	146
22	Background Fraction with CB + Gaussian + Pol3 for $p + \text{Al}$ data	147
23	$A_N^{J/\psi}$ vs. x_F in forward and backward rapidity for $p + p$, $p + \text{Al}$ and $p + \text{Au}$ collision data.	157
24	$A_N^{J/\psi}$ vs. x_F in forward and backward rapidity for $p+p$, $p+\text{Al}$ and $p+\text{Au}$ collision data.	158

LIST OF FIGURES

1	The Standard Model	3
2	Q^2 dependence of $F_2(x, Q^2)$ at various x measured extensively at HERA (H1 and ZEUS), SLAC, CERN and BCDMS [35].	6
3	Proton in the Baryon-Octet system.	7
4	Deep inelastic scattering.	8
5	Hadronic tensor $W^{\mu\nu}$ in the parton model, and its relation with the forward Compton scattering amplitude and its factorized handbag structure.	11
6	Parton distribution functions extracted from F_2 [38]	12
7	The distortion in the distribution of unpolarized partons in momentum space with the spin of proton is along Y direction.	20
8	The Brookhaven hadron facility complex including the AGS Booster, the AGS, and RHIC.	23
9	(a) p-C polarimeters at IP12 interaction point, (b) different asymmetries from different combination of detectors	28
10	Detector setup of the jet polarimeter at RHIC. The six detectors are centered with respect to the interaction point [47].	29
11	The PHENIX coordinate system.	32

12	Pseudo-rapidity(η) and azimuthal angle (ϕ) coverage for the PHENIX central and forward detector subsystems.	33
13	The PHENIX detector. The upper panel shows a beam view of the PHENIX central arm detectors. The lower panel shows a side view of the PHENIX global and muon arm detectors.	34
14	The PHENIX Central Arm and Muon Arm magnets.	35
15	Central Magnet and Muon Magnet field lines shown on a cutaway drawing of the PHENIX magnets. The beams travel along the Z -axis in this figure and collide at $Z = 0$	36
16	Top view of the ZDC size and location.	38
17	Mechanical design of a single layer of the ZDC.	39
18	The South Muon Arm tracking spectrometer.	42
19	Four segments called quadrants in station 1.	44
20	Induced charges collected by cathode strips and signals are generated by readout system.	45
21	Schematic diagram on how cathodes and anodes distribute within one gap.	46
22	Measurement of position resolution obtained in cosmic-ray tests of a station 2 octant. The projection error is $131 \mu\text{m}$	47
23	A drawing of one gap of the MuID. A gap consists of 4 large panels and 2 small panels as shown.	50

24	A drawing of Iarocci streamer tubes in the MuID.	51
25	Half of FVTX assembled. Half-disks corresponding to the 4 stations of each arm with the VTX barrels in the center are shown. The total length is 80 cm.	54
26	Number of hit in each plane for Run 432008 in North arm with $p + p$ data.	57
27	The top (bottom) plot shows the number of hot (dead) planes in each run for North arm with $p + p$ data.	58
28	Number of hit in each packet for Run 432008 in North arm with $p + p$ data.	59
29	The top (bottom) plot shows the number of hot (dead) packets in each run for South arm with $p + p$ data.	60
30	Number of cluster distribution for North arm with $p + p$ data. . .	61
31	Cluster width distribution for South arm in station 1 with $p + p$ data. .	61
32	Dimuon production rate distribution for North arm with $p + p$ data. .	62
33	δp_x and δp_y are obtained by finding the difference between input and output p_x , p_y in PYTHIA6 simulation. A 2σ cut (0.3 GeV) is made.	67
34	p_T distribution for North arm (top) and South arm (bottom) in $p + p$ data.	68

35	MuTr mass spectrum fits with GPR background estimation for $p_T = 0 - 10$ GeV bin for the north(top) and south(bottom) arm with $p + p$ data	73
36	MuTr mass spectrum fits with GPR background estimation for $p_T = 0 - 2$ GeV bin for the north(top) and south(bottom) arm with $p + p$ data	74
37	MuTr mass spectrum fits with GPR background estimation for $p_T = 2 - 10$ GeV bin for the north(top) and south(bottom) arm with $p + p$ data	75
38	MuTr mass spectrum fits with GPR background estimation for $x_F = 0.05 - 0.11$ bin for the north(top) and south(bottom) arm with $p + p$ data	76
39	MuTr mass spectrum fits with GPR background estimation for $x_F = 0.11 - 0.30$ bin for the north(top) and south(bottom) arm with $p + p$ data	77
40	MuTr mass spectrum fits with GPR background estimation for $p_T = 0 - 10$ GeV bin for the north(top) and south(bottom) arm with $p + \text{Au}$ data	78
41	MuTr mass spectrum fits with GPR background estimation for $p_T = 0 - 2$ GeV bin for the north(top) and south(bottom) arm with $p + \text{Au}$ data	79

42	MuTr mass spectrum fits with GPR background estimation for $p_T = 2 - 10$ GeV bin for the north(top) and south(bottom) arm with $p + \text{Au}$ data	80
43	MuTr mass spectrum fits with GPR background estimation for $x_F = 0.05 - 0.11$ bin for the north(top) and south(bottom) arm with $p + \text{Au}$ data	81
44	MuTr mass spectrum fits with GPR background estimation for $x_F = 0.11 - 0.30$ bin for the north(top) and south(bottom) arm with $p + \text{Au}$ data	82
45	MuTr mass spectrum fits with GPR background estimation for $p_T = 0 - 10$ GeV bin for the north(top) and south(bottom) arm with $p + \text{Al}$ data	83
46	MuTr mass spectrum fits with GPR background estimation for $p_T = 0 - 2$ GeV bin for the north(top) and south(bottom) arm with $p + \text{Al}$ data	84
47	MuTr mass spectrum fits with GPR background estimation for $p_T = 2 - 10$ GeV bin for the north(top) and south(bottom) arm with $p + \text{Al}$ data	85
48	MuTr mass spectrum fits with GPR background estimation for $x_F = 0.05 - 0.11$ bin for the north(top) and south(bottom) arm with $p + \text{Al}$ data	86

49	MuTr mass spectrum fits with GPR background estimation for $x_F = 0.11 - 0.30$ GeV bin for the north(top) and south(bottom) arm with $p + \text{Al}$ data	87
50	Beam polarization setup for polarized protons in Run15.	95
51	$p + p$ Inclusive and background A_N with $0 < p_T < 2$ GeV bin in North arm	99
52	$p + p$ Inclusive(left) and background(right) A_N with $2 < p_T < 10$ GeV bin in North arm	100
53	$p + p$ Inclusive(left) and background(right) A_N with $0 < p_T < 2$ GeV bin in South arm	101
54	$p + p$ Inclusive(left) and background(right) A_N with $2 < p_T < 10$ GeV bin in South arm	102
55	pp Inclusive(top plot)&background(bottom plot) A_N with one x_F bin	103
56	This plot shows FVTX_X vs. FVTX_Z distribution in $p + p$ collisions. The intense green band is perpendicular to the x -axis which indicates that $p + p$ collisions in Run15 were along the z -axis.	105
57	This plot shows FVTX_X vs. FVTX_Z distribution in $p + \text{Au}$ collision. The intense green band indicates that $p + \text{Au}$ collisions were not exactly along the z -axis.	106

58	Epsilon scanning with $p+\text{Au}$ dataset. Top (bottom) left: epsilon scanning for inclusive (background) A_N in North arm with $0.05 < x_F < 0.11$. Top (bottom) right: epsilon scanning for inclusive (background) A_N in South arm with $0.05 < x_F < 0.11$.	107
59	$p+\text{Au}$ Inclusive(left) and background(right) A_N with $0 < p_T < 2\text{GeV}$	109
60	$p + \text{Au}$ Inclusive(left) and background(right) A_N with $2 < p_T < 10\text{GeV}$	110
61	$p + \text{Au}$ Inclusive(left) and background(right) A_N with $0.05 < x_F < 0.11$	110
62	$p + \text{Au}$ Inclusive(left) and background(right) A_N with $0.11 < x_F < 0.30$	111
63	A_N for all x_F before tilt angle correction.	112
64	Epsilon scanning with $p+\text{Al}$ dataset. Top left and right plots show the epsilon scanning for inclusive A_N in North arm with $0 < p_T < 2$ GeV and $2 < p_T < 10$ GeV respectively. Bottom left and right plots show the epsilon scanning for background A_N in North arm with $0 < p_T < 2$ GeV and $2 < p_T < 10$ GeV respectively.	113

65	Epsilon scanning with $p+Al$ dataset. Top left and right plots show the epsilon scanning for inclusive A_N in South arm with $0 < p_T < 2$ GeV and $2 < p_T < 10$ GeV respectively. Bottom left and right plots show the epsilon scanning for background A_N in South arm with $0 < p_T < 2$ GeV and $2 < p_T < 10$ GeV respectively.	114
66	$p+Al$ Inclusive(left) and background(right) A_N with $0 < p_T < 2$ GeV	116
67	$p+Al$ Inclusive(left) and background(right) A_N with $2 < p_T < 10$ GeV	117
68	$p+Al$ Inclusive(left) and background(right) A_N with $0.05 < x_F < 0.11$	117
69	$p+Al$ Inclusive(left) and background(right) A_N with $0.11 < x_F < 0.30$	118
70	Inclusive and background A_N got from standalone code with $0 < p_T < 2$ GeV bin in North arm with $p+p$ data	120
71	Inclusive and background A_N got from standalone code with $2 < p_T < 10$ GeV bin in North arm with $p+p$ data	121
72	Inclusive and background A_N got from standalone code with $0 < p_T < 2$ GeV bin in South arm with $p+p$ data	122
73	Inclusive and background A_N got from standalone code with $2 < p_T < 10$ GeV bin in South arm with $p+p$ data	123
74	Inclusive and background A_N got from standalone code with $0 < p_T < 2$ GeV with $p+Au$ data	124
75	Inclusive and background A_N got from standalone code with $2 < p_T < 10$ GeV with $p+Au$ data	125

76	Inclusive and background A_N got from standalone code with combined x_F bin with $p + \text{Au}$ data	126
77	Fill-by-fill Inclusive and background A_N from Maximum Likelihood method with $p + \text{Au}$ data	128
78	Comparing inclusive A_N from different cut sets with Sanghoon and Marie using $p + \text{Au}$ data	129
79	BBCin cross check with $p + p$ data: A 2-D plot filled with BBCin counts reading from Spin Database. X-axis is RHIC crossing number and Y-axis is Run ID number.	130
80	The left plot(North arm) and right plot(South arm) show dimuon yields for each bunch in each run in $p + \text{Au}$ collisions. The X axis is PHENIX crossing number and Y axis is run sequence number.	131
81	$p + \text{Au}$ BBCin cross check: A 2-D plot filled with BBCin counts read from Spin Database. X-axis is RHIC crossing number and Y-axis is Run ID number.	132
82	$A_N^{J/\psi}$ vs. p_T in $p + p$ collisions.	135
83	$A_N^{J/\psi}$ vs. x_F in $p + p$ collisions.	135
84	$A_N^{J/\psi}$ vs. p_T in $p + \text{Au}$ collisions.	136
85	$A_N^{J/\psi}$ vs. x_F in $p + \text{Au}$ collisions.	137
86	$A_N^{J/\psi}$ vs. p_T in $p + \text{Al}$ collisions.	138
87	$A_N^{J/\psi}$ vs. x_F in $p + \text{Al}$ collisions.	139

99	CB+Gaussian+Pol3 fitting in North and South arm for different p_T bins with $p + \text{Al}$ data	152
100	CB+Gaussian+Pol3 fitting in North and South arm for different x_F bins with $p + \text{Al}$ data	153
101	Backward ($x_F < 0$) and forward ($x_F > 0$) $A_N^{J/\psi}$ vs. p_T for the $p + p$, $p + \text{Al}$ and $p + \text{Au}$ collision data. The gray boxes show the systematic uncertainty. The value of p_T for $p + \text{Al}$ and $p + \text{Au}$ have been shifted horizontally for clarity.	155
102	$A_N^{J/\psi}$ vs. x_F for the $p + p$, $p + \text{Al}$ and $p + \text{Au}$ collision data. The gray boxes show the systematic uncertainty. The value of x_F for $p + \text{Al}$ and $p + \text{Au}$ have been shifted horizontally for clarity.	156
103	Inclusive A_N with three p_T bins.	159
104	Inclusive A_N with four p_T bins.	160
105	FVTX Tracklets distribution for the dimuons that pass the dimuon event cuts with $p + \text{Au}$ data	161
106	Inclusive A_N vs. nFVTXTracklets. The first point(star point) is the combined inclusive A_N in lower p_T bin with $p + \text{Au}$ data	161
107	BBC centrality distribution for the dimuons that pass the dimuon event cuts with $p + \text{Au}$ data	162
108	Inclusive A_N vs. BBC centrality. The first point (star point) is the combined inclusive A_N for the first p_T	163

1 INTRODUCTION

1.1 Overview

Philosophers and scientists believe that nature is governed by fundamental principles. Basic theories can be built on these fundamental principles and proved or falsified by observations which rely on carefully designed experiments. This thesis is to report an experimental work to further understand how the fundamental building components of matter, quarks and gluons, come together to form the proton, one of the simplest composite systems.

The fundamental theory for the basic constituents of matter and the interactions among them is called the Standard Model, where the fundamental ingredients of matter are quarks and leptons and their interactions are mediated by gauge bosons. Figure 1 shows all the fundamental particles that are found in the Standard Model. The fundamental interactions are categorized in four types by their respective force carriers and strength: gravity, electromagnetic force, weak interactions and strong interactions. The graviton, the mediator of gravity, is still under exploration. All other three interactions can be described by different representations in quantum field theory. The Quantum Electrodynamics (QED) with U(1) group was initially used to describe the electromagnetic interaction

and, later, a new theory called electroweak theory was discovered to unified the electromagnetic and the weak interactions at a higher energy scale under $SU(2)$ representation. The strong interaction, on the other hand, is described by Quantum Chromodynamics (QCD) with $SU(3)$ group. In QCD theory, quarks are binding together via exchanging gluons which dominates the contribution to the mass of baryonic matter.

1.2 Quantum Chromodynamics

The fundamental theory for describing the strong interaction is called Quantum Chromodynamics (QCD). Similar to QED where the electromagnetic interaction is mediated by photons, the interactions among quarks are mediated by a gauge boson called the gluon and each quark carries ‘color’ charges. In the theory of QED, photons can not interact with each other, while in QCD gluons take on different color charges and can interact among themselves via exchanging gluons. According to the color confinement nature of strong interaction in QCD theory, color charged particles, such as quarks and gluons, cannot be isolated, and therefore cannot be directly observed in normal conditions below the Hagedorn temperature of approximately 2 trillion kelvin [53]. In the QCD theory, the coupling between two color charged particles becomes stronger as their separation distance increases. As a result, it is energetically favorable to create another pair of color charged particles which combine with each of the original pair to form colorless

Standard Model of Elementary Particles

three generations of matter (fermions)					
	I	II	III		
mass	$\approx 2.4 \text{ MeV}/c^2$	$\approx 1.275 \text{ GeV}/c^2$	$\approx 172.44 \text{ GeV}/c^2$	≈ 0	SCALAR BOSONS
charge	2/3	2/3	2/3	0	
spin	1/2	1/2	1/2	0	
	u	c	t	g	
	up	charm	top	gluon	
QUARKS	d	s	b	γ	
	down	strange	bottom	photon	
LEPTONS	e	μ	τ	Z	
	electron	muon	tau	Z boson	
	ν_e	ν_μ	ν_τ	W	
	electron neutrino	muon neutrino	tau neutrino	W boson	
GAUGE BOSONS					

Figure 1: The Standard Model

particles. Another property of QCD theory related to the quark confinement is called “asymptotic freedom” which states that the interaction strength of colored objects decreases when they are closer [54]. The theoretical advantage of the asymptotic freedom property of QCD is that, at short distance scale, the calculations of the cross section can be performed perturbatively, in terms of the coupling constant $\alpha_s(Q)$, order by order. As it has been shown in [42], the scattering cross-section between quarks and gluons can be calculated at next-to-next-to-leading order (NNLO). The perturbative part of the cross-section is only one piece of information needed to calculate the cross-section for the entire scattering process. There are additional non-perturbative parts which account for the distribution of the partons (Parton Distribution Function) in the ingoing hadrons and the fragmentation (Fragmentation Function) of the outgoing colored parton. In order to address the non-perturbative parts, a theorem called factorization theorem has been developed. The factorization theorem systematically separates the calculation of cross-section in a high energy process into a short distance part (which can be calculated analytically) and a long distance non-perturbative functions which contains parameters that can be determined by the experiments. The factorization could be very powerful because of the universality of these non-perturbative functions which has been shown in figure 2. The universality theorem states that the non-perturbative functions got from one process can be used in other processes. One of the common examples is the unpolarized production cross-section

of hadrons and jets in high energy collisions experiments where the differential cross-section can be described as

$$E_{bh} \frac{d\sigma^3}{d^3 p_h} = \sum_{abc} \int dx_a dx_b \frac{dz}{z} f_{a/A}(x_a) f_{b/B}(x_b) \sigma(a + b \rightarrow c + X) D_{h/c}(z), \quad (1)$$

where $f_{a/A}(x_a)$ and $f_{b/B}(x_b)$ are the Parton Distribution Functions (PDFs) mentioned above, which describe the probability of finding parton a(b) carrying momentum fraction $x_a(x_b)$ in parent nucleon A(B). σ is the hard-scattering part of the process which can be calculated via perturbative QCD. $D_{h/c}$ represents the probability that parton c fragments into a hadron h, and z is the fraction of the momentum of parton c taken by h.

1.3 The Structure of Proton

Based on the outcome of the Geiger-Marsden experiment which was designed by Rutherford in 1917, physicists believed that the most of the atomic mass was concentrated at the center of an atom and the proton was thought as an fundamental particle without substructures. As more hadrons were discovered in the following decades, it became clear that they could not all be elementary. One of the successful methods to categorize those particles is the so-called “Eightfold way” proposed by Murray Gell-Mann [50] and Yuval Ne’eman. This method was based on the hypothesis that more fundamental particles called quarks exist and the three flavors (up, down and strange) follow the SU(3) symmetry. As shown

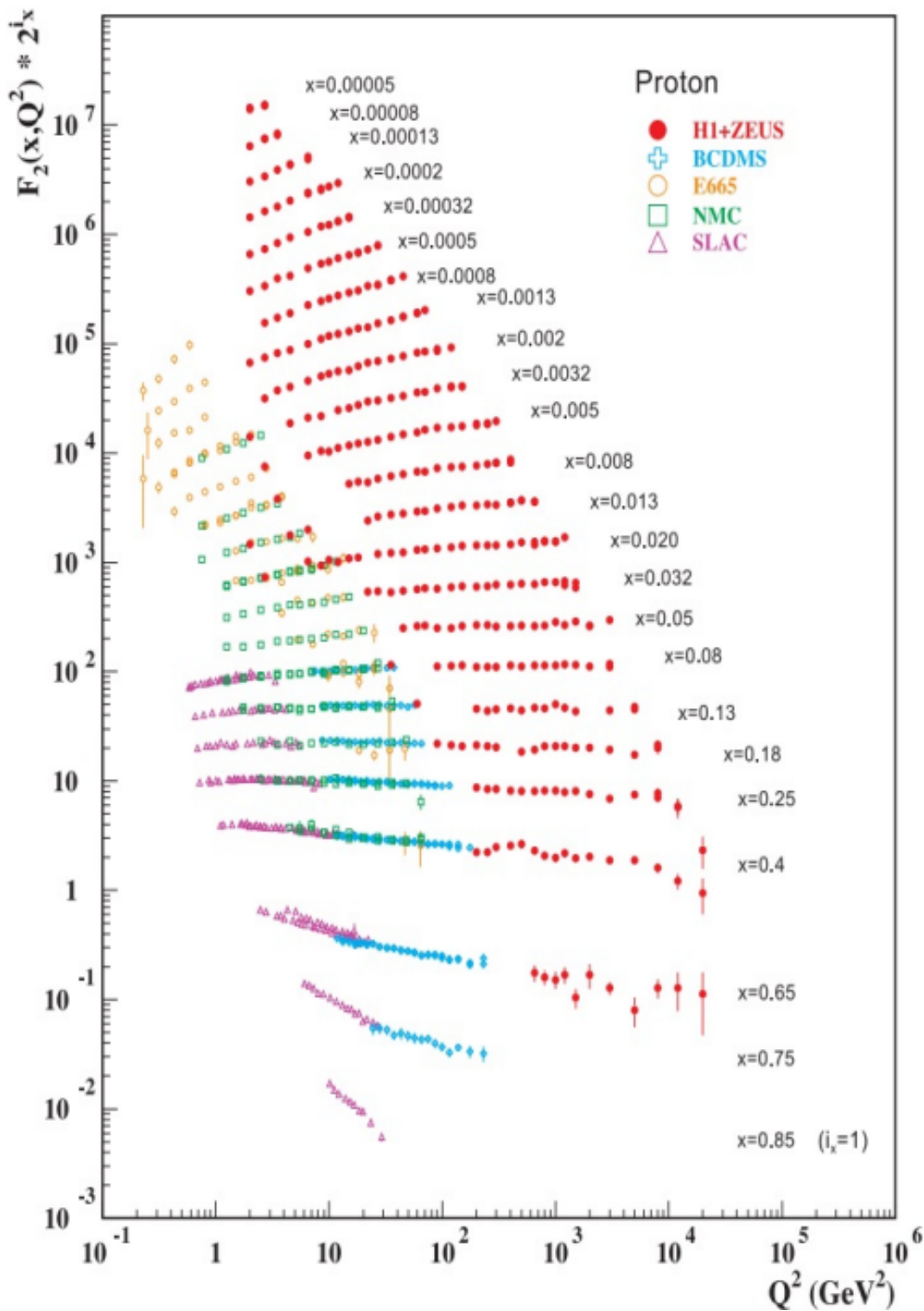


Figure 2: Q^2 dependence of $F_2(x, Q^2)$ at various x measured extensively at HERA (H1 and ZEUS), SLAC, CERN and BCDMS [35].

in figure 3, the proton belongs to the baryon octet family and it is made of three valence quarks: two up quarks and one down quark. In 1968, the deep inelastic scattering experiment carried out at Stanford Linear Accelerator Center confirmed the existence of the quarks. Additionally, the charm, bottom and top quark were found subsequently.

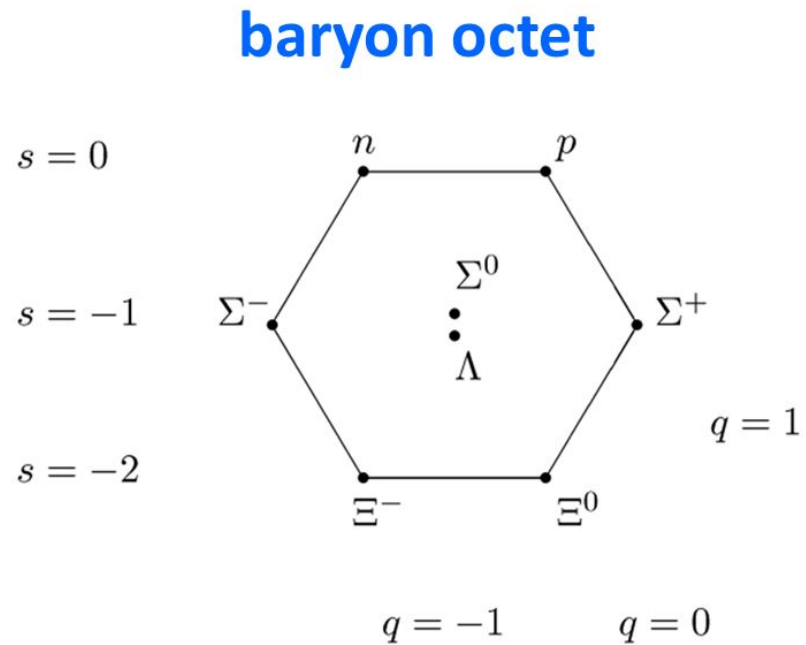


Figure 3: Proton in the Baryon-Octet system.

1.4 Deep Inelastic Scattering

Deep Inelastic Scattering (DIS) is a powerful tool to explore the structure of the proton. In a DIS process, a lepton (electron or muon) collides with a proton and the outcome particles are measured. The large momentum transfer via an intermediate virtual photon is sensitive to the dynamics and structures at short distance scales. Therefore, the detection of point-like particles like quarks becomes possible. The other advantage of such DIS process is that the lepton carries no color charge which makes the interactions between lepton and proton purely electromagnetic in the leading order. By treating the quark struck by the virtual photon as a free quark, the interaction between virtual photon and quark is simplified as two point-like free particle interaction which can be easily calculated.

Take the process in figure 4 as an example. The 4-momentum of the lepton

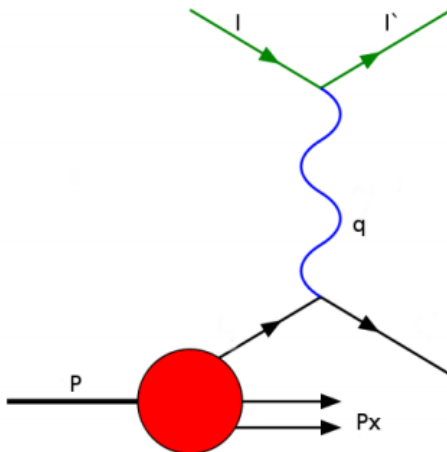


Figure 4: Deep inelastic scattering.

before and after the DIS scattering is denoted as l and l' respectively. The 4-momentum of the virtual photon is q . P and P_x are the 4-momentum of the proton before and after the scattering. The DIS process is usually described by the following invariants:

$$q^2 = (l - l')^2 = -2EE'(1 - \cos(\theta)) \quad (2)$$

$$\nu = \frac{P * q}{M} \quad (3)$$

$$x = \frac{Q^2}{2P * q} = \frac{Q^2}{2M * \nu} \quad (4)$$

$$y = \frac{P * q}{P * l} \quad (5)$$

where θ is the scattering angle of the outgoing lepton, ν is the energy of the virtual photon in the lab frame, M is the mass of the proton, x is the Bjorken scaling variable, y is the inelasticity, and $Q^2 = -q^2$. At high energies, in the infinite momentum frame, the Bjorken limit is satisfied where ν and $Q^2 \rightarrow \infty$ and x is fixed. Under the Bjorken limit, the DIS cross-section can be written as [33]:

$$d^3\sigma = \frac{1}{4P \cdot Q^4} \frac{e^4}{L_{\mu\nu}} W^{\mu\nu} 2\pi \frac{d^3l'}{(2\pi)^3 2E'} \quad (6)$$

where $L_{\mu\nu}$ is the lepton tensor which depends on the spin and momentum of the incoming and outgoing lepton. The lepton tensor can be calculated perturbatively via Feynman diagrams. The $W^{\mu\nu}$ is the hadronic tensor which describes the structure of the proton. This part is corresponding to the non-perturbative part

of the process. $W_{\mu\nu}$ can be rewritten as following:

$$W_{\mu\nu} = W_{\mu\nu}^S(q, P) + iW_{\mu\nu}^A(q; P, s) \quad (7)$$

where $W_{\mu\nu}^S(q, P)$ and $W_{\mu\nu}^A(q; P, s)$ are the symmetric and anti-symmetric part of $W_{\mu\nu}$ that facilitate the calculation of polarized and unpolarized cross-sections.

Similar tricks can also be applied on the leptonic tensor $L_{\mu\nu}$:

$$L_{\mu\nu} = L_{\mu\nu}^S(l, l') + iL_{\mu\nu}^A(l, s_l; l') \quad (8)$$

Then equation 6 can be written as following [33]:

$$\frac{d^2\sigma}{dE'd\Omega} = \frac{\alpha_{em}^2}{2MQ^4}(L_{\mu\nu}^{(S)}W^{\mu\nu(S)} - L_{\mu\nu}^{(A)}W^{\mu\nu(A)}) \quad (9)$$

1.5 Unpolarized parton distribution

By averaging over the incoming lepton and proton spins, one can get the unpolarized cross-section in equation 9:

$$\frac{d^2\sigma^{unp}}{dE'd\Omega} = \frac{\alpha_{em}^2}{2MQ^4}L_{\mu\nu}^{(S)}W^{\mu\nu(S)} = \frac{4\alpha_{em}^2 E'^2}{Q^4}(2W_1 \sin^2 \theta/2 + W_2 \cos^2 \theta/2) \quad (10)$$

Here W_1 and W_2 are introduced in $W_{\mu\nu}^{(S)}$.

$$\frac{1}{2M}W_{\mu\nu}^{(S)} = (-g_{\mu\nu} + \frac{q_\mu q_\nu}{q^2})W_1(P \cdot q, q^2) + \frac{1}{M^2}(P_\mu - \frac{P \cdot q}{q^2}q_\mu)(P_\nu - \frac{P \cdot q}{q^2}q_\nu)W_2(P \cdot q, q^2) \quad (11)$$

One can also introduce the dimensionless structure functions F_1 and F_2 related to W_1 and W_2 :

$$F_1(x, Q^2) = MW_1(\nu, Q^2) \quad (12)$$

$$F_2(x, Q^2) = \nu W_2(\nu, Q^2) \quad (13)$$

which in the Bjorken limit, are depend only on x as we shall see figure 2.

In the quark-parton model of nucleon, the unpolarized quark/parton distribution functions can be described by the unpolarized structure functions. According to this model, in the kinematical region of $Q^2 \rightarrow \infty$ and $E \rightarrow \infty$, the proton behaves as a gas of free partons. In that case, the probability of recovering a proton in the final state is very low. So in the calculation of the DIS cross section, the hadronic tensor $W^{\mu\nu}$ is calculated basing on the parton model graph shown in figure 5.

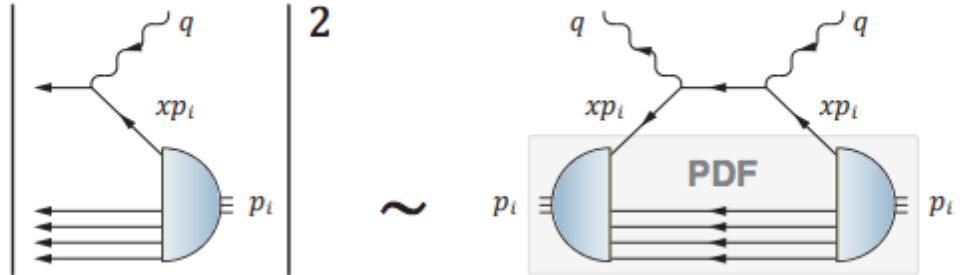


Figure 5: Hadronic tensor $W^{\mu\nu}$ in the parton model, and its relation with the forward Compton scattering amplitude and its factorized handbag structure.

As it has been shown in figure 6, gluons are dominant in low- x region and gluons split into quark anti-quark pairs which causes the structure function F_2 to increase with Q^2 .

Also from the right panel of figure 6, the density of gluons is increasing within

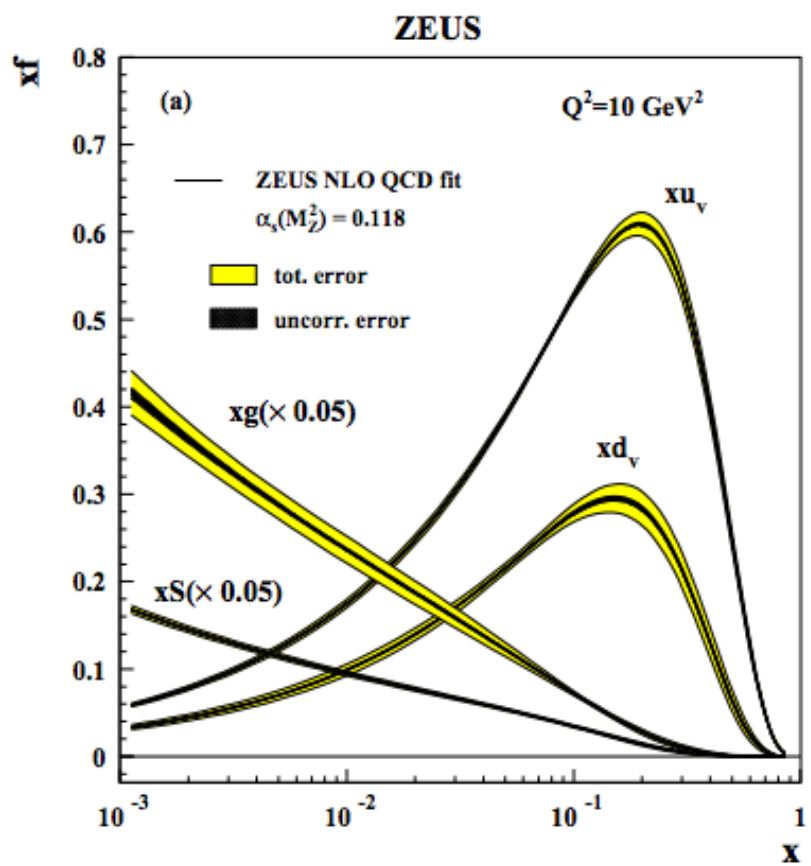


Figure 6: Parton distribution functions extracted from F_2 [38]

lower x region which means, at certain point, the gluon distribution has to saturate. But it is difficult to observe the gluon saturation effects due to the limited machine capability and detector acceptance. So in the recent decades, the low- x phenomena in nucleon and heavy nucleus is a major research.

1.6 Polarized parton distributions

In order to fully understand the structure of the proton, scientists moved the step forward to extract the spin information in proton. The polarized parton distribution function is trying to explain in which way the spin and orbital motion of its constituents contribute to the proton spin. One of the few theories on the market is proposed by Ji [56] which states that:

$$\frac{1}{2} = J_q + J_g = \frac{1}{2}\Delta\Sigma + J_q + L_g \quad (14)$$

where J_q and J_g are the total angular momentum. In Ji's theory work, J_q and J_g can be measured in deeply virtual Compton scattering process. But problems were arise when further decomposition of J_q and J_g were studied. L_q cannot be simply interpreted as quark orbital angular momentum because the quark-gluon interactions are involved. On the other hand, one cannot decompose J_g in a gauge invariant way into gluon spin and orbital angular momentum.

The other one is called the Jaffe-Manohar sum rule [55] which decomposes the proton spin into the quark spin $\Delta\Sigma$, gluon spin ΔG , and orbital angular

momentum of quarks and gluons L_q and L_g :

$$\frac{1}{2} = \frac{1}{2}\Delta\Sigma + \Delta G + L_q + L_g \quad (15)$$

The difference of cross sections with opposite target spin polarizations is given by:

$$d\sigma(\mathbf{S}) - d\sigma(-\mathbf{S}) \sim \frac{2\alpha^2}{MQ^4} \frac{E'}{E} L_{\mu\nu}^{(A)} W^{\mu\nu(A)} \quad (16)$$

where the asymmetric part of hadron tensor can be expressed as two spin-dependent structure functions G_1 and G_2 :

$$\begin{aligned} \frac{1}{2M} W_{\mu\nu}^{(A)}(q; p, S) &= \epsilon_{\mu\nu\alpha\beta} q^\alpha M S^\beta G_1(p \cdot q, q^2) \\ &+ \epsilon_{\mu\nu\alpha\beta} q^\alpha [(p \cdot q) S^\beta + (S \cdot q) p^\beta] \frac{W_2(p \cdot q, q^2)}{M} \end{aligned} \quad (17)$$

Similar with the case in unpolarized structure, one can introduce a dimensionless structure functions g_1 and g_2 related to G_1 and G_2 :

$$g_1(x, Q^2) = \frac{(p \cdot q)^2}{\nu} G_1(\nu, Q^2) \quad (18)$$

$$g_2(x, Q^2) = \nu(p \cdot q) G_2(\nu, Q^2) \quad (19)$$

In the longitudinal polarized spin asymmetries in DIS experiments, the longitudinal polarized spin asymmetry is defined as follow:

$$A_{long} = \frac{d\sigma^{\leftarrow\rightarrow} - d\sigma^{\leftarrow\leftarrow}}{d\sigma^{\leftarrow\rightarrow} + d\sigma^{\leftarrow\leftarrow}} \quad (20)$$

where \leftarrow and \Rightarrow indicate the polarization direction of the lepton beam and the hadron target respectively. A measurement of A_{long} will provide the information on g_1 , because the contribution from g_2 is approximately zero [34].

The DIS experiment results indicate that quark and anti-quark contributions ($\Delta\Sigma$) to proton spin is only about 20-35%. The remaining contribution, based on this model, comes from ΔG , L_q and L_g [27, 2, 11, 12, 19, 4, 1, 29, 28, 80, 22, 15, 21].

In order to have a fuller understanding of proton structure, beyond the unpolarized and longitudinally polarized PDFs, one also needs to study the transversely polarized PDFs. One of the main reason is based on the fact that the spatial rotation transformations do not commute with the boost transformation. In that case, the proton structure measured by longitudinally polarized beams and targets are not equivalent to the transversely polarized case. To that end, we tried to extract proton's transverse spin structure by measuring the transverse single spin asymmetry in $p p$ and pA collisions.

1.7 Transverse Single Spin Asymmetry

In polarized $p+p$ collisions, the transverse single spin asymmetry (TSSA), A_N , is defined as the amplitude of the azimuthal angular modulation of the outgoing particle's scattering cross section with respect to the transverse spin direction of the polarized proton. Early theoretical predictions which were purely based on perturbative calculations showed that the TSSA should be inversely proportional

to the hard scale of the scattering [58], and if applied to the reactions at RHIC energies, the asymmetry would be very small, of order 10^{-4} . However, the experimental asymmetries of light-flavored hadrons turned out to be much larger, of order 10^{-1} [63, 31].

In order to explain what has been observed in experiments, several theoretical frameworks [75, 76, 40, 46, 68] were developed in the 1990s. In the collinear factorization framework, contributions from multi-parton correlations to the transverse-spin-dependent cross section were introduced through three types of spin-momentum correlations: (1) twist-3 correlation functions of a polarized hadron $\phi_{a/A}^{(3)}(x_1, x_2, \vec{s}_\perp)$ convolved with leading-twist correlation functions of an unpolarized hadron $\phi_{b/B}(x')$ and with leading-twist parton fragmentation functions $D_{c \rightarrow C}(z)$, (2) transversity parton distribution functions $\delta q_{a/A}(x, \vec{s}_\perp)$ convolved with twist-3 correlation functions of an unpolarized hadron $\phi_{b/B}^{(3)}(x'_1, x'_2)$ and leading-twist parton fragmentation functions $D_{c \rightarrow C}(z)$, and (3) transversity parton distribution functions $\delta q_{a/A}(x, \vec{s}_\perp)$ convolved with leading-twist correlation functions of an unpolarized hadron $\phi_{b/B}(x')$ and with twist-3 fragmentation functions $D_{c \rightarrow C}^{(3)}(z_1, z_2)$ [69]:

$$\begin{aligned}
A_N \propto & \sum_{abc} \phi_{a/A}^{(3)}(x_1, x_2, \vec{s}_\perp) \otimes \phi_{b/B}(x') \otimes \hat{\sigma} \otimes D_{c \rightarrow C}(z) + \\
& \sum_{abc} \delta q_{a/A}(x, \vec{s}_\perp) \otimes \phi_{b/B}^{(3)}(x'_1, x'_2) \otimes \hat{\sigma}' \otimes D_{c \rightarrow C}(z) + \\
& \sum_{abc} \delta q_{a/A}(x, \vec{s}_\perp) \otimes \phi_{b/B}(x') \otimes \hat{\sigma}'' \otimes D_{c \rightarrow C}^{(3)}(z_1, z_2).
\end{aligned} \tag{21}$$

In this notation, a/A means the distribution of parton a in hadron A , b/B means the distribution of parton b in hadron B and $c \rightarrow C$ means the fragmentation of parton c into hadron C . Additionally, x is the Bjorken parton momentum fraction of the incoming hadron; z is the fraction of the outgoing partonic momentum carried by the detected hadron; \vec{s}_\perp is the transverse spin of the incoming hadron; $\hat{\sigma}$, $\hat{\sigma}'$, and $\hat{\sigma}''$ are the partonic hard-scattering cross sections of a process where higher twist is associated with the incoming polarized or unpolarized hadron, or outgoing partons, respectively. Non-zero values for $\phi_{a/A}^{(3)}(x_1, x_2, \vec{s}_\perp)$ and $D_{c \rightarrow C}^{(3)}(z_1, z_2)$ in Eq. 21 account for the large A_N observed in experiment, where $\phi_{a/A}^{(3)}(x_1, x_2, \vec{s}_\perp)$ corresponds to initial-state effects [68] and $D_{c \rightarrow C}^{(3)}(z_1, z_2)$ to final-state effects [62].

Initial-state effects are described by the twist-3 three-parton correlation functions $\phi_{a/A}^{(3)}(x_1, x_2, \vec{s}_\perp)$ and $\phi_{b/B}^{(3)}(x'_1, x'_2)$ which measure the quantum interference between two scattering amplitudes of the incoming hadron [60], while final-state effects are related to twist-3 fragmentation functions $D_{c \rightarrow C}^{(3)}(z_1, z_2)$ which describe the process in which the outgoing parton fragments into a final-state hadron [60]. At RHIC energies, heavy quark production, such as J/ψ production, is dominated

by gluon-gluon interactions; since the gluon transversity distribution does not exist, the second and third terms of Eq. 21 are zero. This means that heavy flavor A_N is free from final-state effects and is sensitive to initial-state effects, such as the gluon Qiu-Sterman and tri-gluon correlations which correspond to the factor $\phi_{a/A}^{(3)}(x_1, x_2, \vec{s}_\perp)$ in Eq. 21 [59].

In the case of high energy hadronic collisions, a non-vanishing SSA is generated by a parton-level spin flip and a phase difference between the scattering amplitude and the corresponding complex conjugate. In the context of the QCD collinear factorization framework, the parton-level spin flip is generated by the interference between the active single parton and a two-parton composite state of the scattering amplitude. On the other hand, the phase difference is achieved by the interference between the real and imaginary part of the partonic scattering amplitude [68, 69, 71]. For the Qiu-Sterman correlation, the quantum interference is between a quark state of momentum fraction x and a quark-gluon composite state with the same momentum fraction where either the gluon or quark carries the total momentum of the quark-gluon composite state [61]. In the tri-gluon correlation, the two parton composite state is composed of two gluons instead of a quark and gluon as described above for the Qiu-Sterman correlation [60, 37]. The collinear factorization framework has been widely used to describe the TSSAs measured at RHIC [6, 3, 5, 13, 8, 9, 16, 30].

An alternative treatment is known as the Transverse-Momentum-Dependent

(TMD) formalism. In this formalism, the cross section is factorized into hard-scattering cross sections and TMD parton distribution and fragmentation functions (PDFs and FFs) [25]. For the TMD approach to be valid in the context of $p+p$ collisions, Q^2 must be large, in order to use perturbative QCD, while the transverse momentum must satisfy $p_T \ll Q$ and not be much larger than the intrinsic, parton transverse momentum k_T , so that effects of the latter remain visible [41]. One of the TMD PDFs, called the Sivers function [75], is widely used in describing the TSSAs that were observed in different processes [18, 14, 51, 44, 65]. The Sivers function, denoted by $f_{1T}^\perp(x, \mathbf{k}_\perp^2)$, describes the distortion in the distribution of unpolarized partons with momentum fraction x and transverse momentum \mathbf{k}_\perp in a transversely polarized hadron. As shown in figure 7, the distortion in the distribution of unpolarized partons is described by the orbital angular motion of the parton inside proton correlates with the spin of the proton. This distorted distribution of unpolarized partons causes an azimuthal anisotropy in the distribution of parton transverse momenta in the polarized hadron which gives rise to the non-zero TSSA. As it has been described above, at low p_T , the non-perturbative TMD Sivers function will be responsible for its SSA, while twist-3 dominates the contributions to the SSA when $p_T \sim Q$. At intermediate p_T , one can see the transition between these two frameworks and a relation between Sivers Function and Qiu-Sterman Function has been shown in Ref. [36].

With increasing experimental information on the quark Sivers function during

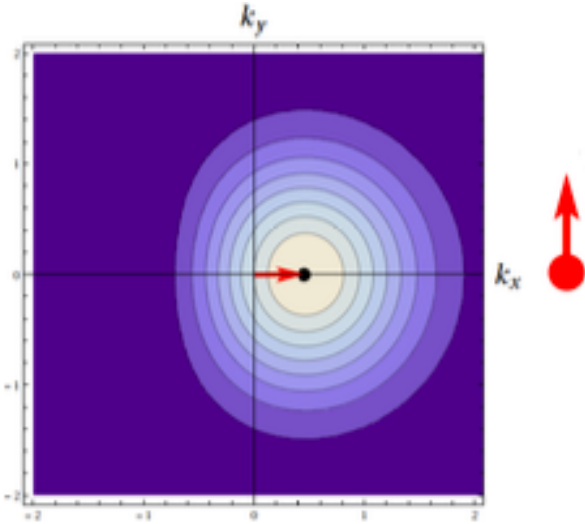


Figure 7: The distortion in the distribution of unpolarized partons in momentum space with the spin of proton is along Y direction.

the last ten years, our understanding of this quantity has matured [26, 23, 39, 78, 24], while the gluon Sivers function is still relatively unknown. The transversely polarized $p + p$ collisions studied at RHIC present a very good opportunity to study the gluon Sivers function as gluon-gluon interactions are dominant in $p + p$ collisions at RHIC energies. PHENIX has measured the TSSA for J/ψ production at central and forward rapidities [7] and, at small p_T values, where the J/ψ mass becomes the large scale Q in TMD factorization, the result has been compared to a gluon Sivers function derived in the context of the Color Evaporation Model in [52].

In proton-nucleus ($p+A$) collisions, the increase of the atomic number results in increasing gluon occupancy and therefore gluon saturation effects may become

important in the small x region. In the Regge-Gribov limit, the properties of saturated gluons in the infinite-momentum frame can be described by the Color Glass Condensate (CGC) which has been applied to a variety of processes such as $e + p$, $e + A$, $A + A$, and $p + A$ collisions [49]. The quark and gluon distribution functions for large nuclei were computed first in Ref. [64] in the weak coupling limit. Using the CGC framework, one can describe the rescatterings of the outgoing parton within the nucleus. In the coherent QCD multiple scattering framework [70], it has been shown that at low p_T the rates of single and double hadron production are highly suppressed and the amount of suppression grows with rapidity and centrality; meanwhile, at high p_T , such nuclear modification effects become less pronounced as we enter the perturbative region in a dilute nuclear medium. For the computation of TSSAs, a hybrid approach has been widely used in photon, γ -jet and di-jet production [74, 73, 82, 81]. The hybrid approach treats the gluon distribution inside the heavy nucleus in the CGC framework and utilizes the twist-3 formalism for the proton side. The resummation of the power corrections in $p + A$ reactions shifts the nuclear PDF to higher x [70]. The new PHENIX $p + A$ collision data offer the opportunity to quantify how this shift in x affects the twist-3 description of the TSSAs discussed above.

2 EXPERIMENT SETUP AT PHENIX

In order to explore the structure of protons, high energy collisions are required as well as sophisticated detector arrays. The muons which are the final-state particles of interest in this analysis were detected and recorded by the Pioneering High Energy Nuclear Interaction eXperiment (PHENIX) detector at the Relativistic Heavy Ion Collider (RHIC) in the year 2015 (Run 15). In the first part of this chapter, a brief introduction of RHIC is made followed by the description of PHENIX detector systems. The triggering and data acquisition (DAQ) will be described in the last section.

2.1 The Relativistic Heavy Ion Collider (RHIC)

The Relativistic Heavy Ion Collider (RHIC) is located at Brookhaven National Laboratory in Upton, New York. RHIC was built for two main purposes; one is to explore the possible quark and gluon deconfinement, which is also known as Quark-Gluon Plasma (QGP), by colliding gold nuclei to reach high energy density and temperature conditions. The other one is to investigate the spin puzzle by colliding a polarized proton beam with a proton or other heavy ion beam, such as aluminum or gold. The center of mass energy of the collisions ranges from 62.4 GeV to 510 GeV. The lay-out of the Brookhaven accelerator complex with the highlight of the components required for polarized beam acceleration is shown in

Fig 8.

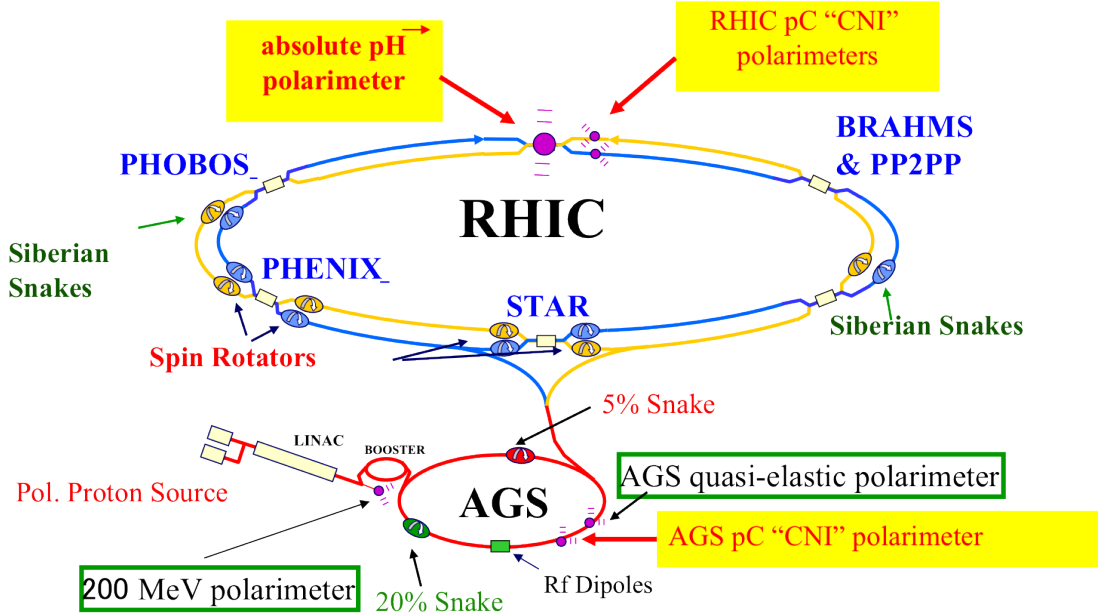


Figure 8: The Brookhaven hadron facility complex including the AGS Booster, the AGS, and RHIC.

2.1.1 RHIC-AGS complex

In the case of the collisions involving polarized protons at RHIC, to achieve reasonable measurement statistics requires the bunch intensity to be 2×10^{11} protons per bunch. Considering some losses during the transfer to RHIC, the Alternating Gradient Synchrotron (AGS) will need to have a bunch intensity around 4×10^{11} . In order to meet the requirement of the bunch intensity, the optically pumped polarized ion source has been installed. Under the normal operation condition, the source should generate $500 \mu\text{A}$ in a single $300 \mu\text{s}$ pulse. A pulse of polarized H^-

ions from the source are accelerated to 200 GeV using the 200 MHz LINAC with an efficiency of about 50%. Then the AGS Booster will capture the strip-injected H⁻ ions. As it has been mentioned above, the number of polarized protons for each bunch in Booster is 4×10^{11} . Having been accelerated to 1.5 GeV kinetic energy in the Booster, each bunch of polarized protons is then transferred to the AGS, where it is accelerated to 25 GeV.

2.1.2 Spin Dynamics and Siberian Snakes

An understanding of the evolution of spin during acceleration and the tools to control it are required in order to accelerate the polarized beams to achieve high energy and high intensity polarized proton collisions. It has been proved that the evolution of the spin direction of a polarized proton beam in external magnetic fields can be described by the Thomas-BMT equation [32]:

$$\frac{d\vec{P}}{dt} = - \left(\frac{e}{\gamma m} \right) \left[G\gamma \vec{B}_\perp + (1+G)\vec{B}_\parallel \right] \times \vec{P} \quad (22)$$

where \vec{P} is the polarization vector in the frame that moves with the particle, $G = 1.7928$ is the anomalous magnetic moment of the proton and $\gamma = E/m$. If a pure vertical magnetic field is applied, this precession equation looks quite similar to the Lorentz force equation which describes the evolution of the orbital motion of charged particle in an external magnetic field:

$$\frac{d\vec{v}}{dt} = - \left(\frac{e}{\gamma m} \right) \left[\vec{B}_\perp \right] \times \vec{v} \quad (23)$$

So in a pure vertical magnetic field, the orbital motion completes a cycle $G\gamma$ times slower than the spin. Namely, the factor $G\gamma$ gives the number of full spin precessions for every full revolution. This number is also called the spin tune ν_{sp} which is approximately 478 for a proton with energy of 250 GeV.

The presence of numerous depolarizing resonances make the acceleration of polarized beams in circular accelerators complicated since a depolarizing resonance is crossed whenever the spin precession frequency equals the frequency with which spin-perturbing magnetic fields are encountered during acceleration. There are two main types of depolarizing resonances: imperfection resonances, which is caused by the misalignments and errors of magnets, and intrinsic resonances, caused by the focusing fields.

As it has been shown in the previous paragraph, the resonance conditions are described by the spin tune ν_{sp} . During the acceleration in the cycle, the stable spin direction is along the main vertical magnetic field. However, when the resonance arise where the ν_{sp} is very close to a integer, the stable spin direction is perturbed away from the original direction by the resonance driving fields. Analytically, in the case of acceleration of a polarized beam via an isolated resonance, the final polarization can be calculated [48] and is given by

$$\frac{P_f}{P_i} = 2 \exp \left(-\frac{\pi |\epsilon|^2}{2\alpha} \right) - 1, \quad (24)$$

where P_i and P_f are the polarizations before and after the resonance crossing,

respectively, the resonance strength ϵ is obtained from the spin rotation of the driving fields and α is the change of the spin tune per radian of the orbit angle.

The Eq. 24 shows that when $\alpha \gg |\epsilon|^2$, the polarization before and after the resonance crossing remains the same. In order to achieve this, the “Siberian Snake” [45] is introduced. It generates a 180° spin rotation along a horizontal axis which makes the spin rotation much larger than the spin rotation caused by the resonance driving fields. In that case, the beam polarization is preserved during the acceleration.

2.1.3 Polarimeters

At the experimental end, the beam polarization measurement in RHIC provides the beam polarization value (P_B) which acts as a normalization factor when a physics asymmetry is calculated from the raw (measured) asymmetry. There are two types of polarimeters installed in RHIC, in order to measure the vertical component of the proton beam polarization: the Proton-Carbon (p-C) polarimeter [57] and the Hydrogen-Jet (H-Jet) polarimeter [66, 79]. They are installed in the 12 o’clock area (IP12) in the RHIC ring. The H-Jet polarimeter measures the polarization of both beams because it is located at the collision point. Two identical p-C polarimeters are mounted on the separated blue and yellow beams.

Generally speaking, by obtaining the asymmetry in the left and right scattering cross section with a known analyzing power A_P , one can measure the vertical beam

polarization (P_B) using the following equation:

$$P_B = \frac{1}{A_p(x_F, p_T)} \frac{Ed^3\sigma_L/dp^3 - Ed^3\sigma_R/dp^3}{Ed^3\sigma_L/dp^3 + Ed^3\sigma_R/dp^3}, \quad (25)$$

which can be rewritten as a function of the number of scatters left and right normalized by luminosity (N_L and N_R):

$$P_B = \frac{1}{A_p} \frac{N_L - N_R}{N_L + N_R}, \quad (26)$$

A_p can be known from experiment or theory.

The proton-carbon (pC) polarimeter is used to measure the relative polarization of each beam because (1) the analyzing power in the Coulomb-nuclear interference region was measured by the AGS experiment E950 [20], the value of which is about 0.01 and (2) the large cross section of proton-carbon elastic scattering provides fast feedback on the beam polarization. The term “Coulomb-nuclear interference” (CNI) is used to describe this process because it originates from interference between electromagnetic and hadronic elastic scattering amplitudes.

Figure 9 shows the pC polarimeter located at IP12 and the asymmetries that can be measured with different combinations among six silicon detectors which are positioned at the azimuthal angles of 45° , 90° and 135° on both left and right sides with respect to the beam and each silicon detector is located at 18.5 cm from the carbon ribbon target. There are 4×10^6 recoiled carbons collected by the pC polarimeters per one scanning within about one minute which makes the pC polarimeter capable to measure the beam polarization for multiple times during

one fill. The fast measurement of the beam polarizations using pC polarimeter provides immediate information on the beam polarization qualities, such as the beam stability and decay.

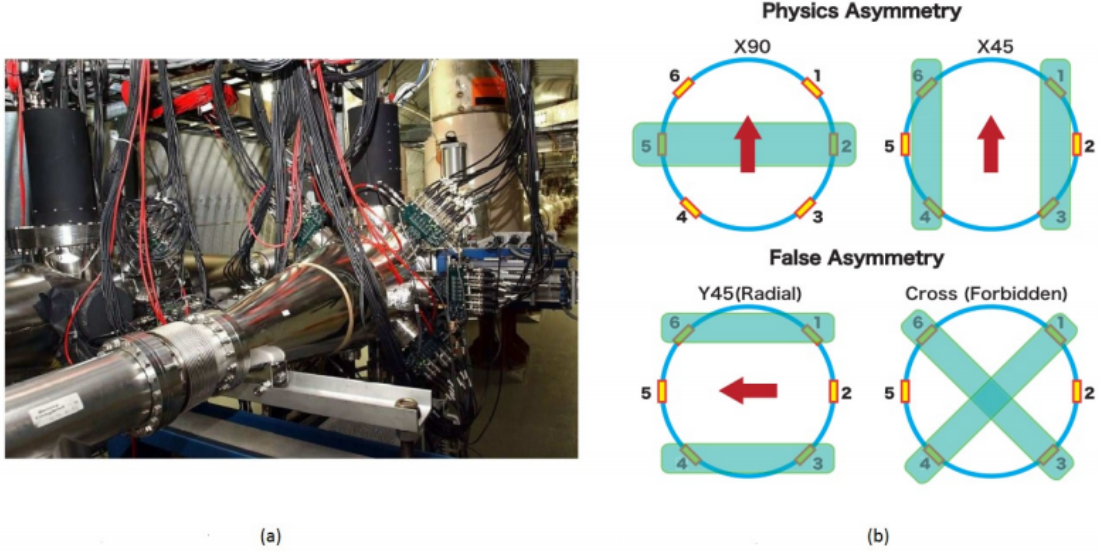


Figure 9: (a) p-C polarimeters at IP12 interaction point, (b) different asymmetries from different combination of detectors

The Hydrogen jet polarimeter (H-jet polarimeter) shown in figure 10, instead of measuring the relative polarization as pC polarimeter does, measures the absolute polarization of the beam. Although the analyzing power for proton-proton elastic scattering can not be measured or calculated in a high precision, the polarization of hydrogen-jet-target is precisely known ($> 90\%$) with the uncertainty better than 2% in absolute polarization. This can be used as an alternative method to get the beam polarization. In this case, there are two asymmetries that can

be measured: the asymmetry corresponding to the polarized target (ε_{tgt}) and the asymmetry corresponding to the polarized beam (ε_{beam}). In both cases, the analyzing power are the same. Therefore, the beam polarization can be calculated as shown in Eq. 27.

$$A_N = \frac{\varepsilon_{tgt}}{P_{tgt}} = \frac{\varepsilon_{beam}}{P_{beam}} \Rightarrow P_{beam} = P_{tgt} \frac{\varepsilon_{beam}}{\varepsilon_{tgt}} \quad (27)$$

By applying the measured P_{beam} back to Eq. 26, the analyzing power of the process can be measured and reference [67] shows the result of measurement of the analyzing power using the jet polarimeter.

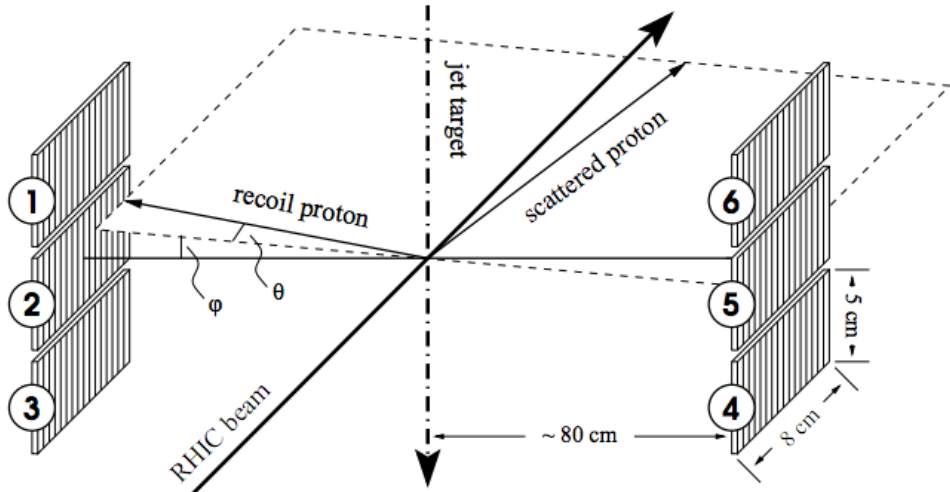


Figure 10: Detector setup of the jet polarimeter at RHIC. The six detectors are centered with respect to the interaction point [47].

2.1.4 Spin Rotators

The stable polarized beam direction in the process of acceleration and storage is given by the cross product of the proton's momentum and the ring radius. In that case of studying longitudinal spin asymmetry, the spin direction of the beam needs to be rotated before reaching the interaction point. Both the radial and longitudinal spin can be achieved by the spin rotator dipole magnets which is commissioned in 2003. The spin rotators are located outside the interaction regions of both PHENIX and STAR which enable both facilities to choose their experiment design, either longitudinally or transversely polarized collisions, independently.

2.2 PHENIX

The Pioneering High Energy Nuclear Interaction eXperiment (PHENIX) is located at the 8 o'clock intersection point at RHIC. With a collection of specialized detector subsystems, PHENIX is efficient to detect photons, leptons and hadrons with excellent particle identification capability. Other than that, the subsystems in PHENIX are capable to deal with both high-multiplicity heavy-ion collisions and high event-rate collisions such as $p + p$ and $p + A$ collisions.

The definition of a global coordinate system used in the PHENIX experiment is shown in figure 11. The origin point $(0, 0, 0)$ is defined as the geometrical

center of the interaction region. The z -axis is along the beam-line with positive direction pointing to the north. The positive x -axis direction is defined in the western direction, and positive y -axis is pointing upward. The coordinate system in PHENIX is right-handed. The azimuthal angle ϕ is measured counter-clockwise relative to the positive x -axis in the xy -plane and the polar angle θ is the opening angle between the positive z -axis and the vector to be measured. In the context of accelerator physics, rapidity y is a widely used quantity that defines as following:

$$y = \frac{1}{2} \ln\left(\frac{E + p_z c}{E - p_z c}\right) \quad (28)$$

The rapidity is very useful when dealing with a Lorentz transforming parallel to the beam axis with velocity $v = \beta c$. The equation for the transformation on rapidity is particularly simple:

$$y' = y - \tanh^{-1}\beta \quad (29)$$

The simple form of Lorentz transformation for y shown in equation 29 has an important consequence that, in the case of two particles ejected after a collision, the difference of y between two ejected particles are invariant with respect to Lorentz boosts along the z -axis:

$$y'_1 - y'_2 = y_1 - \tanh^{-1}\beta - (y_2 - \tanh^{-1}\beta) = y_1 - y_2 \quad (30)$$

For highly relativistic particles, the rapidity is approximately equal to pseudora-

pidity, the definition of which is shown as following:

$$\eta = -\ln[\tan(\theta/2)] \quad (31)$$

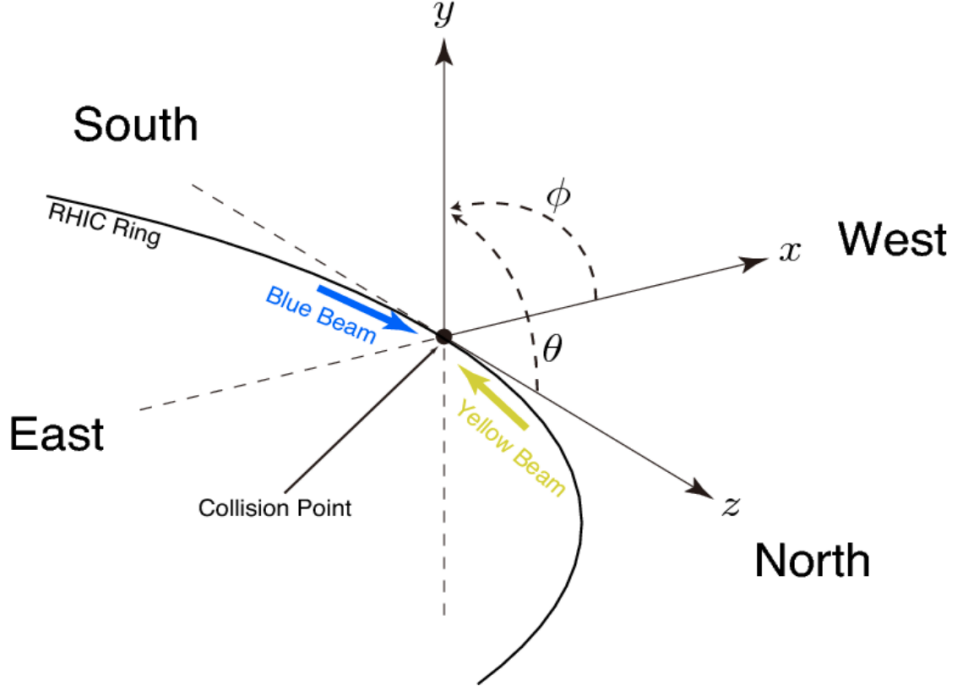


Figure 11: The PHENIX coordinate system.

There are three main groups in the PHENIX detector subsystems: global detectors, central arm detectors and muon arm detectors. The function of global detectors is for event characterization and triggering. The central arms (East and West), which cover $2 \times (\pi/2)$ in azimuthal angle ϕ and with a pseudo-rapidity coverage of $|\eta| < 0.35$, are mainly used for photon, electron and hadron detection. Two muon arms (North and South) with a full azimuthal coverage and a pseudo-rapidity coverage of $1.2 < \eta < 2.4$ (North) and $-2.2 < \eta < -1.2$ (South) are

mainly for muon detection in the forward and backward rapidities. Figure 12 shows the acceptance coverage for central and forward detector subsystems. There are three magnets used for momentum measurement of charged particles: the central magnet and two muon magnets. The schematic review of the PHENIX detector setup is shown in figure 13.

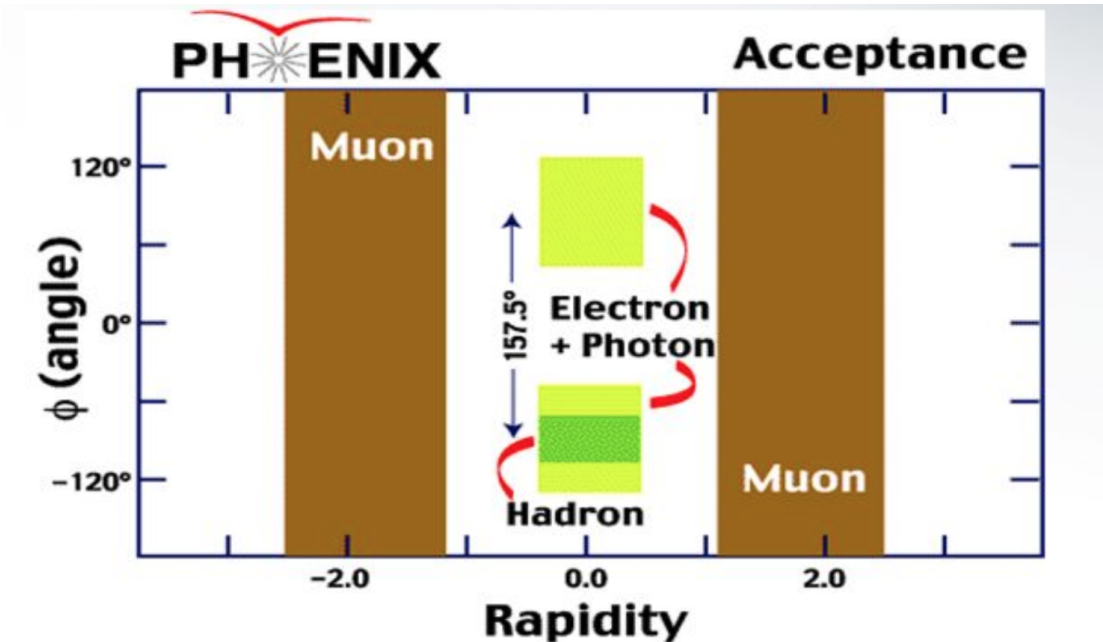


Figure 12: Pseudo-rapidity(η) and azimuthal angle (ϕ) coverage for the PHENIX central and forward detector subsystems.

2.2.1 PHENIX Magnet System

The PHENIX magnet system is composed of three spectrometer magnets with warm iron yokes and water-cooled copper coils which is shown in figure 14. The energy of Central Magnet is provided by two pairs of concentric coils which gener-

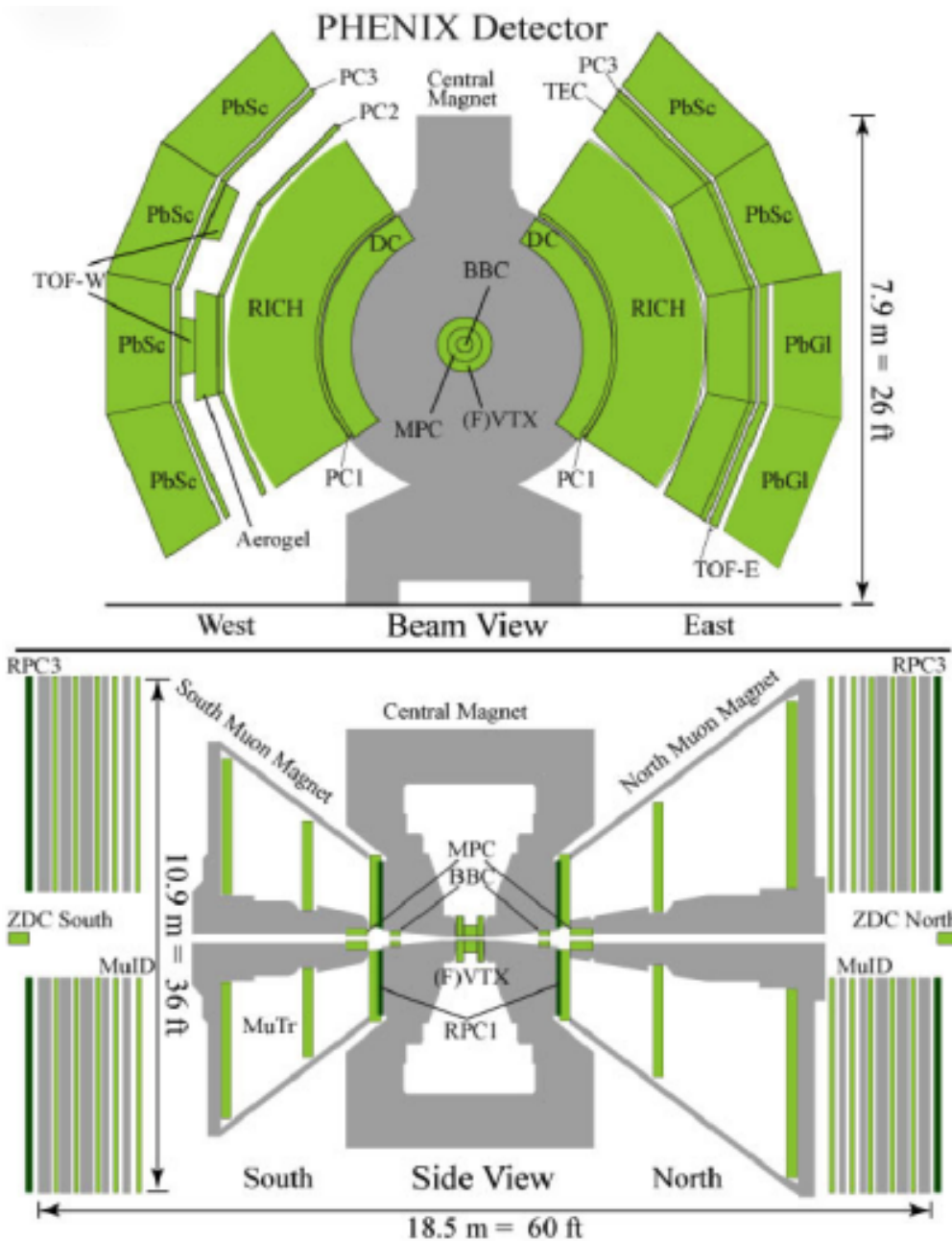


Figure 13: The PHENIX detector. The upper panel shows a beam view of the PHENIX central arm detectors. The lower panel shows a side view of the PHENIX global and muon arm detectors.

ates a field around the interaction vertex that is parallel to the beam. The north and south Muon Magnets (MMN and MMS) use solenoid coils to provide a radial magnetic field for muon analysis. The Muon Magnets covers a pseudo-rapidity interval of 1.1 to 2.4 for North arm and that of -2.2 to -1.1 for South arm. Both Muon Magnets cover the full azimuth. The Main Magnet coils are wound on cylindrical surfaces at the end of large tapered pistons. All the three magnets provide a field integral of about 0.8 Tesla-meters. Figure 15 shows the magnets distribution inside the central and forward detector subsystems.

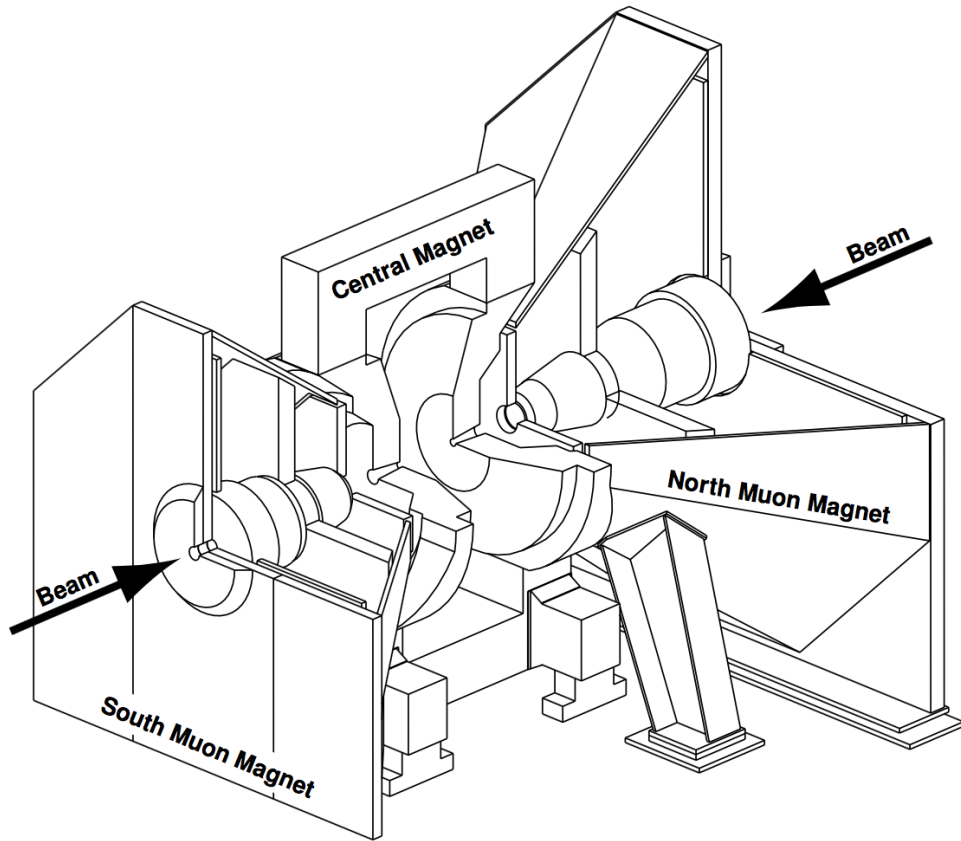


Figure 14: The PHENIX Central Arm and Muon Arm magnets.

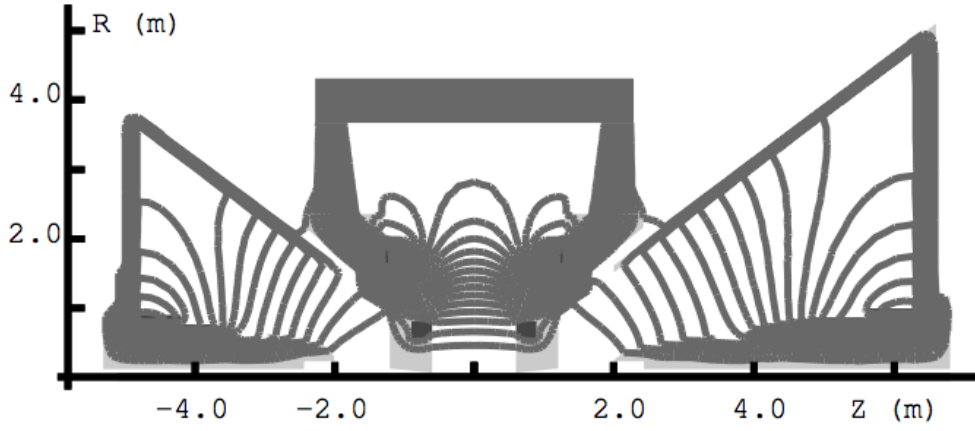


Figure 15: Central Magnet and Muon Magnet field lines shown on a cutaway drawing of the PHENIX magnets. The beams travel along the Z -axis in this figure and collide at $Z = 0$.

2.2.2 Global detectors

The Beam Beam Counters (BBC) and the Zero Degree Calorimeters (ZDC) are commonly used by all measurements in PHENIX for event characterization and triggering and are categorized as the global detectors. Both detectors either alone or combined with other triggers in PHENIX play an essential role in determining whether an interesting event has occurred during a collision or not.

Two BBC are located, one to the North and one to the South, at 144 cm from the interaction point along the beam line with full azimuthal coverage and rapidity coverage of $|\eta| \in [3.1, 3.9]$. Each BBC has 64 elements consisting of a

quartz Cherenkov radiator and a mesh-dynode PMT. The BBCs also serve as an interaction vertex finder with resolution along the beam direction of about 2 cm in $p+p$ collisions and in addition play the role of a luminosity detector [10]. For each collision, two times are measured by BBC: the average time of arrival at north arm (t_N) and south arm (t_S). The time of interaction (t_0) and the beam-beam collision point along the z -axis are determined from these times:

$$z_{BBC} = c(t_N - t_S)/2 \quad (32)$$

$$t_0 = (t_N + t_S)/2 \quad (33)$$

This vertex calculation serves as a minimum bias trigger. The resolution of the z_{BBC} vertex measurement is about 5 cm.

The Zero Degree Calorimeter (ZDC) is hadronic calorimeter for tagging neutrons in forward rapidity at PHENIX. Similar to the BBC, the ZDC also consists of two arms but much farther from the interaction point; approximately 18 m away with pseudo-rapidity range of $|\eta| > 6$. As shown in figure 16, the ZDC is sitting behind the DX dipole magnets which sweep away most of the charged particles which makes ZDC capable to serve as a trigger for neutral particles with a long lifetime, such as neutrons and photons. Within each layer of ZDC, there is an absorber composed of copper-tungsten together with a PMT which collects and amplifies the light signal guided along optical fibers. In order to exclude the charged particles that reach the ZDC, an additional charged particle identifier is

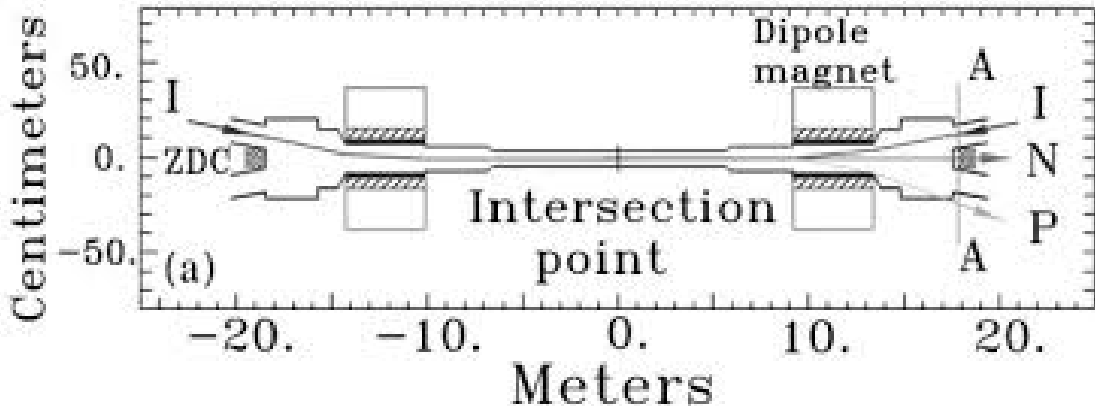


Figure 16: Top view of the ZDC size and location.

placed between the front of the ZDC and the interaction point. Another detector, called Shower Maximum Detector (SMD), [WHAT IS SMD AND HOW DOES IT WORK? [MD]] are layers of position sensitive hodoscopes mounted between the first two layers of the ZDC. The purpose of the SMD is to measure the centroid of showers in the ZDC in 2 coordinates-x and y. The position resolution of the collision vertex provided by SMD is approximately 1 cm in the transverse plane. ZDC also serves as a local level-1 triggering detector and luminosity monitor. Figure 17 shows the mechanical design of a single layer of the ZDC.

2.2.3 Central Arm Detectors

The central arm detector system contains two subsystems: the East and West Arms which are located in the central rapidity range $|\eta| < 0.35$. The azimuthal coverage for tracking provided by the Drift Chamber and the Pad Chamber is approximately $\pi/2$. The particle identification is performed by using ring imaging

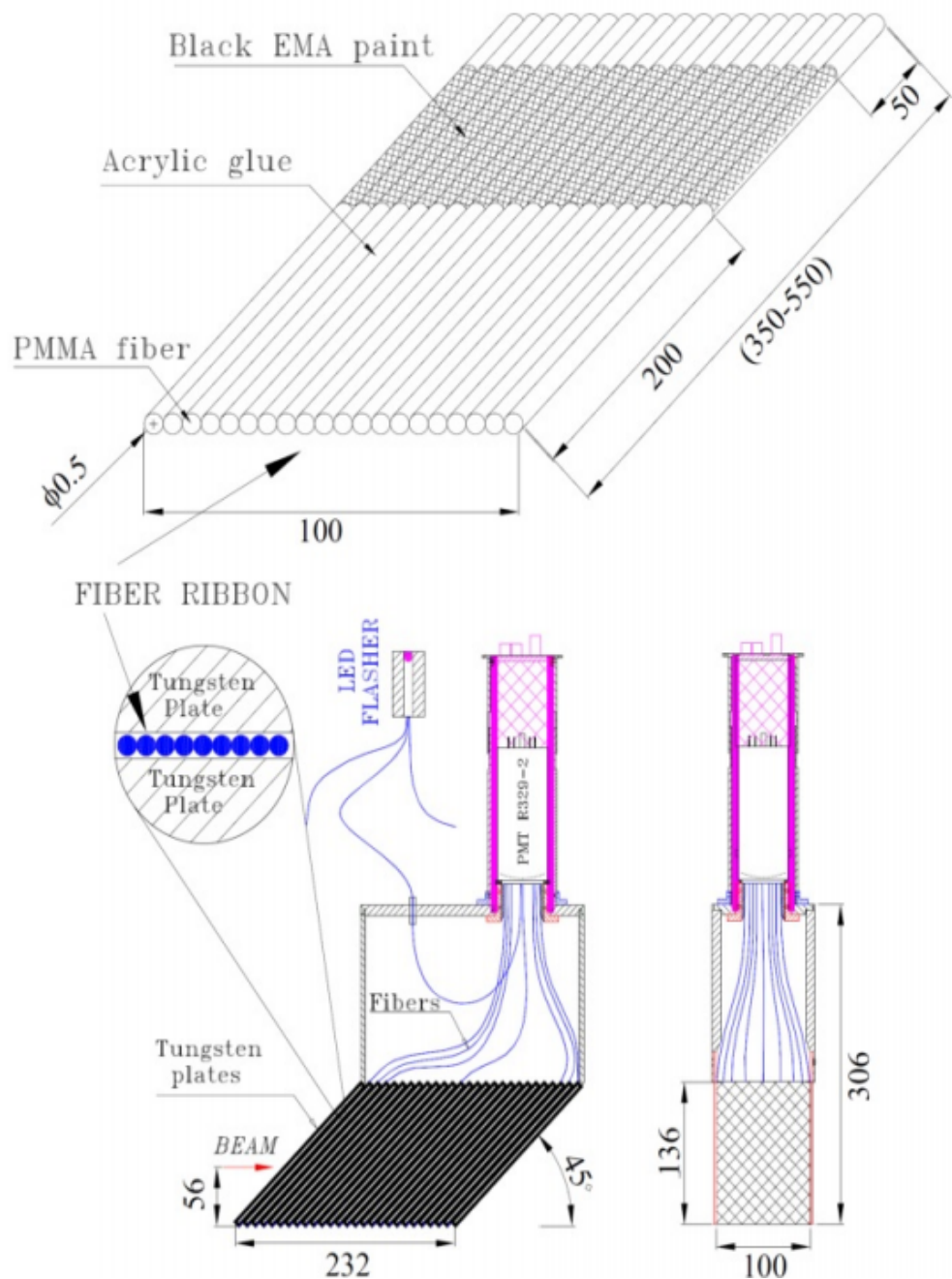


Figure 17: Mechanical design of a single layer of the ZDC.

Cerenkov detectors, and time-of-flight detectors with a resolution of about 100 ps. Additionally, there are two electromagnetic calorimeters (EmCal) consisting of lead glass and lead scintillator technologies with 4 sectors in each arm. The rapidity acceptance of the EmCal is $|\eta| < 0.375$ with an azimuthal coverage of $\pi/2$ in each arm.

The central arm detectors are focused on providing high resolution tracking with segmented electromagnetic calorimetry which, in the context of high occupancy in heavy ion collisions, is very suitable. The typical processes covered by the central arm detectors are two photons from π^0 decay, direct photons and electron pairs decayed from J/ψ . As it has been shown in figure 13, the central arm detector system consists of Silicon Vertex Tracker, Drift Chambers, Pad Chambers, Ring Imaging Cerenkov Detectors, Aerogel Cherenkov detectors, Time Expansion Chamber and Electromagnetic Calorimeters. Since this paper is not about the central arm analysis, we will not discuss central arm detector systems in detail.

2.2.4 Forward arm detectors

The forward arm detectors consist of Muon Tracker (MuTr), Muon ID (MuID), RPC and FVTX. The MuTr combined with the MuID is called the Muon Arm which is main detector system used for this analysis. In addition to that, the PHENIX Muon Arms also provide a means of studying vector meson production, the Drell-Yan process (with dimuon decay channel) and heavy quark production.

The MuTr plays the role as tracking detector of the muon arms. The design specifications of the Muon Arm Tracker were driven by the research requirements:

1. Capable to separate J/ψ from ψ' and $\Upsilon(1S)$ from $\Upsilon(2S, 3S)$.
2. provide a large enough signal-to-background and acceptance for vector mesons to be able to do statistically significant physics measurements within 1 year of RHIC running.
3. have low enough occupancy to be able to reconstruct tracks efficiently in central Au+Au events.
4. perform well in the lower occupancy with higher event rate $p+p$ and $p+A$ physics programs.

Muon Tracker (MuTr) Each MuTr arm contains three stations of cathode-strip readout tracking chambers inside the Muon Magnets described in the previous section. From smaller to larger $|z|$, the stations are called Station 1, 2, and 3. The rapidity coverage of MuTr for North and South Arm is slightly different. For South MuTr, the rapidity coverage is $-2.2 < \eta < -1.1$, while it is $1.1 < \eta < 1.2$ for North MuTr and they both cover the full azimuthal angle. The z -position of the three stations, from Station 1 to 3, is -1.80, -3.00 and -4.60 m for South Arm and 1.80, 3.47 and 6.12 m for the North Arm, respectively.

In the first station in each arm, there are four identical segments called “quadrants”, while, in second and third stations, there are eight segments called “oc-

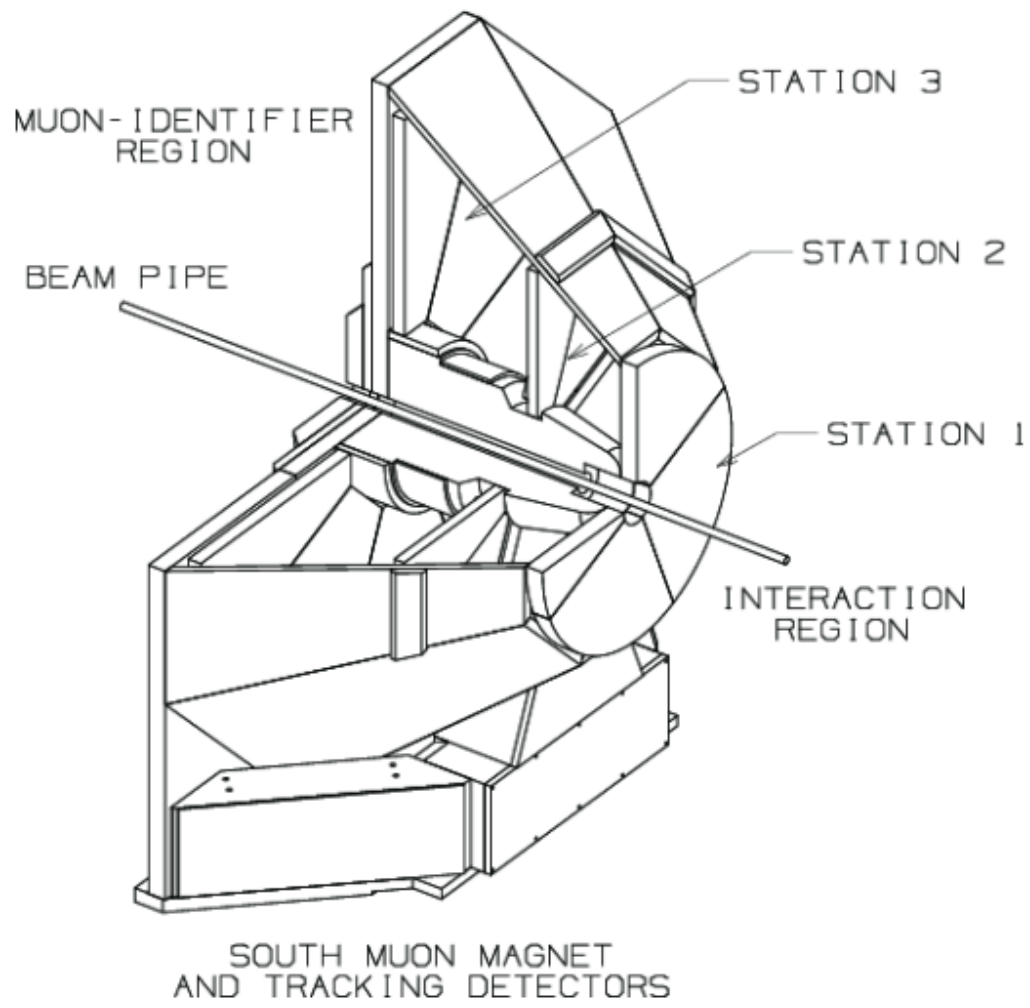


Figure 18: The South Muon Arm tracking spectrometer.

tants”. As it is shown in figure 19, the station 1 tracking chambers are located closest to the interaction region and have the smallest areas. Therefore, the station 1 has the highest occupancy per strip because of which station 1 has the most stringent requirements on dead regions within the acceptance (95% active area). The station 2 octant cathodes consisted of etched 25 micron copper coated mylar foils which makes station 2 maintain good momentum resolution with about 0.3 GeV in both x and y directions.

There are three “gaps” in the MuTr detectors in stations 1 and 2, and two gaps in station 3. Each gap contains a pair of cathode readout planes on either side of on anode wire plane. In order to determine the 2-D hit position in $x - y$ plane, half of the cathode planes have strips perpendicular to the anode wires and the other half have strips at stereo angles between 0 and ± 11.25 deg with respect to the perpendicular strips as it has been show in figure 21. The gaps are filled with a gas mixture: 50% Ar, 30% CO₂ and 20% CF₄. When a track pass through a gap, the gas within it will be ionized. As shown in figure 20, the induced charges will drift to the cathode and form an induced charge distribution. Then the cathodes are read out by the Muon Tracking Front End Electronics (FEE). On both sides of the station 2 chamber, there is a scintillator which was used to provide a trigger for cosmic rays passing through the chamber. With the data collected from this trigger, one can search for clusters in each cathode readout plane. Then the centroid strip position is extracted by fitting the clusters. 5 out

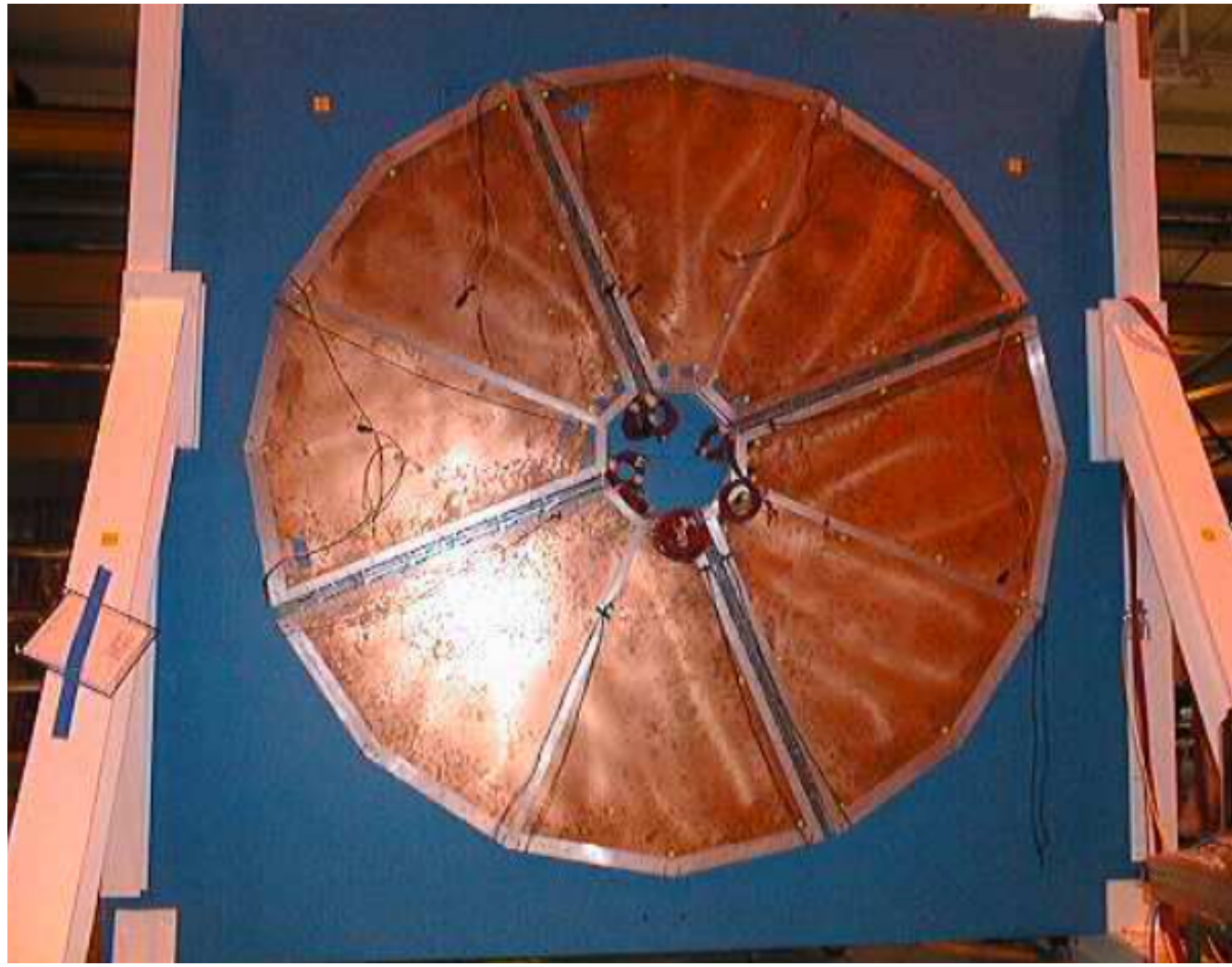


Figure 19: Four segments called quadrants in station 1.

of 6 of the readout planes were fit with a straight line which is projected to the sixth readout plane. A cut that only select tracks approximately perpendicular to the surface of the chamber was applied and the difference between the projected straight-line fit and the position measured by the sixth plane was plotted. As shown in the figure 22, the position resolution of a track in a gap is with high accuracy of about $130 \mu\text{m}$.

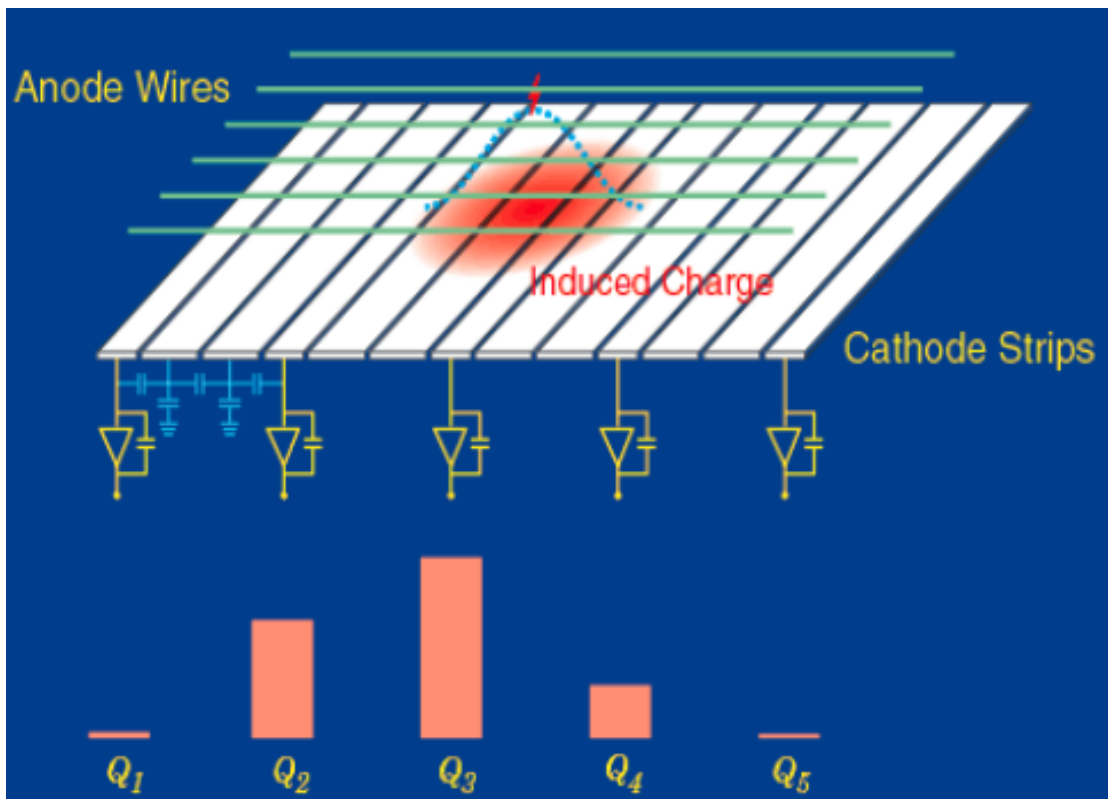


Figure 20: Induced charges collected by cathode strips and signals are generated by readout system.

The Muon Tracking Front End Electronics is the interface between the muon

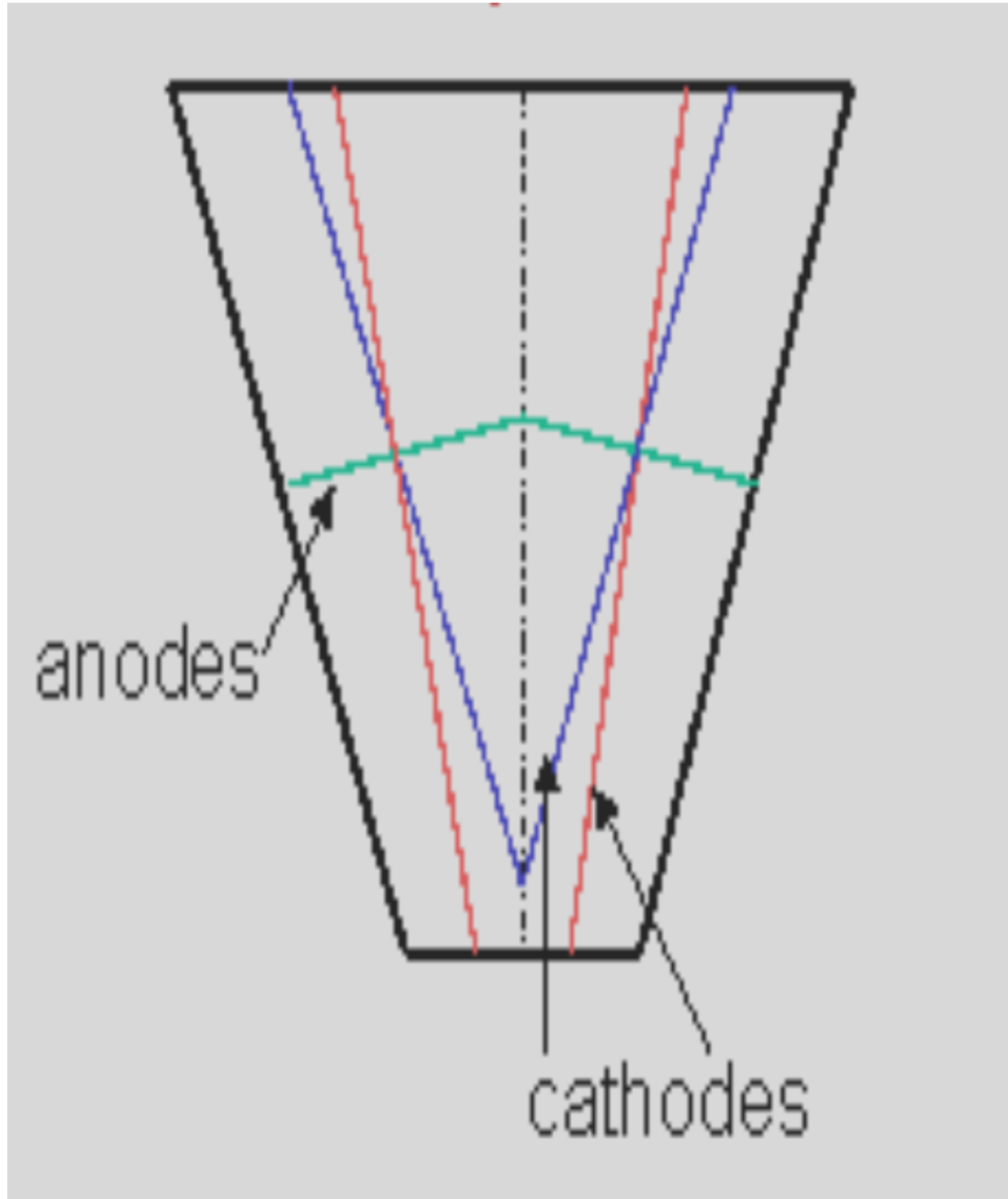


Figure 21: Schematic diagram on how cathodes and anodes distribute within one gap.

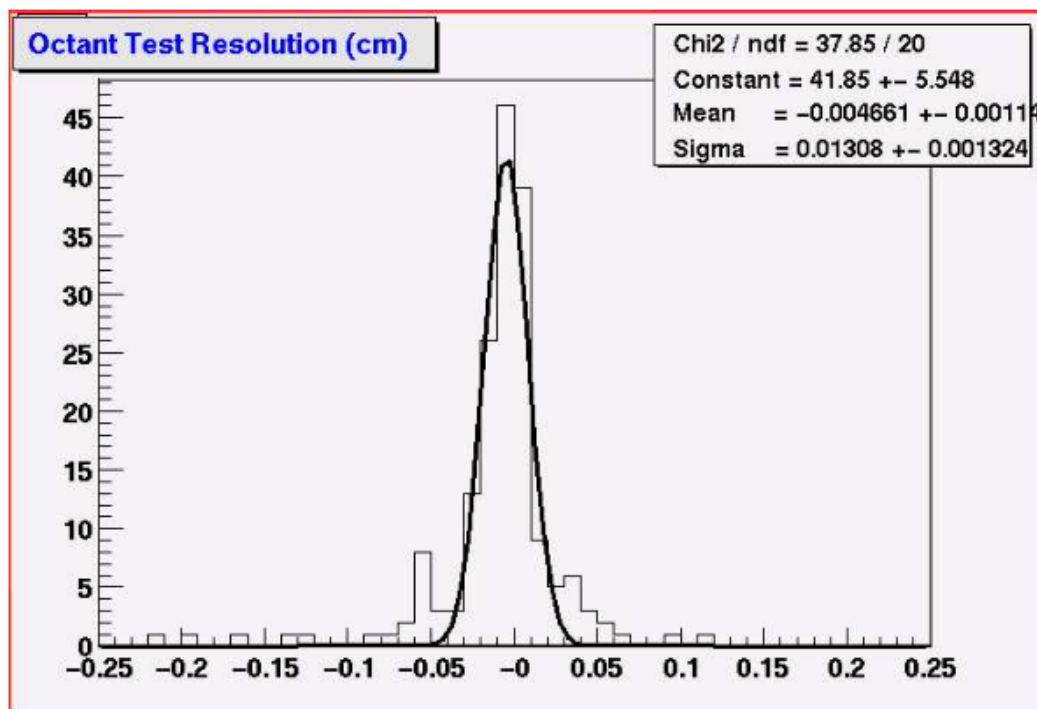


Figure 22: Measurement of position resolution obtained in cosmic-ray tests of a station 2 octant. The projection error is $131 \mu\text{m}$.

Table 1: Parameters of hadron absorbers in MuID.

Location	Material	South Thickness (cm)	North Thickness (cm)	$\lambda_I/\cos\theta$
1st Layer	Steel	10	10	0.6
2nd Layer	Steel	10	10	0.6
3rd Layer	Steel	20	20	1.2
4th Layer	Steel	20	20	1.2
5th Layer	Steel	20	20	1.2

chambers and the PHENIX online Data Acquisition (DAQ) system. The hit information from the chamber cathodes are continuously amplified and stored by the electronics. After a trigger signal sent out by the PHENIX granule timing module (GTM), stored samples from all channels are digitalized and the information are sent to next level data collection module for further processing.

Muon Identifier (MuID) The MuID is a trigger detector with five layers of plastic proportional tubes of the Iarocci type located behind the MuTr in each muon arm. Also it provides the seed for the offline tracking. Doing μ/π separation is the main purpose of MuID. For this reason, each detector layer is sandwiched by steel absorbers which are used to reduce the number of hadrons relative to the number of muons. Each layer is called a “gap”, the width and height of which is about 15 m and 10 m, respectively. Table 1 shows the thickness of each steel absorber wall with the corresponding radiation length.

Within each gap, there are 4 large panels as well as 2 small ones which have been shown in figure 23 and each panel has horizontal and vertical arrays of tubes called “two-packs”. The panel is composed of an aluminum frame wire chamber called Iarocci streamer tube which is shown in figure 24. An Iarocci tube consists of nine 9×9 mm wire cells put side-by-side with either 2.5 or 5.6 m length. There is an anode wire in each cell with a square cathode surrounding. The non-flammable mixture of 92% CO₂ and 8% Isobutane is filled in the MuID with uniform flow to all panels. There are 6340 tubes total in two muon arms (3170 for each arm).

Resistive Plate Chambers (RPC) were installed in 2009 (RPC3) and 2011 (RPC1) in PHENIX for providing dedicated triggers for the W boson measurement. RPC1 is installed right before MuTr station 1 and RPC3 is right behind MuID as shown in the lower plot in figure 13.

When the beam energy is very high (in RHIC Run 2013, the center of mass energy of proton-proton collisions was 510 GeV), the luminosity is so high that in every 106 ns (one bunch crossing time), at least one collision occurs. Therefore, in order to prevent bunch crossing timing mixups by BBCs between neighboring beam crossings, a faster timing is provided by the RPC.

Forward Vertex Detector (FVTX) is one of the PHENIX forward arm upgrades in 2012. The purpose of introducing FVTX is to enhance the PHENIX muon arms capability by providing precise tracking of charged particles before interacting with the hadron absorbers.

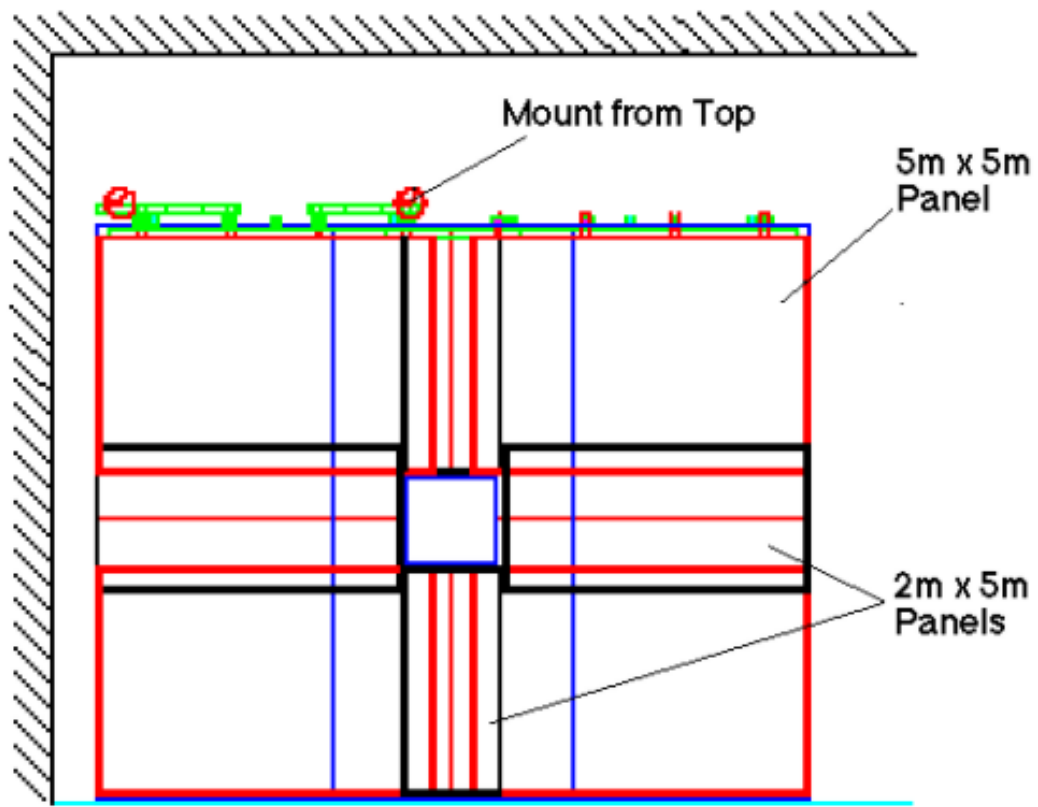
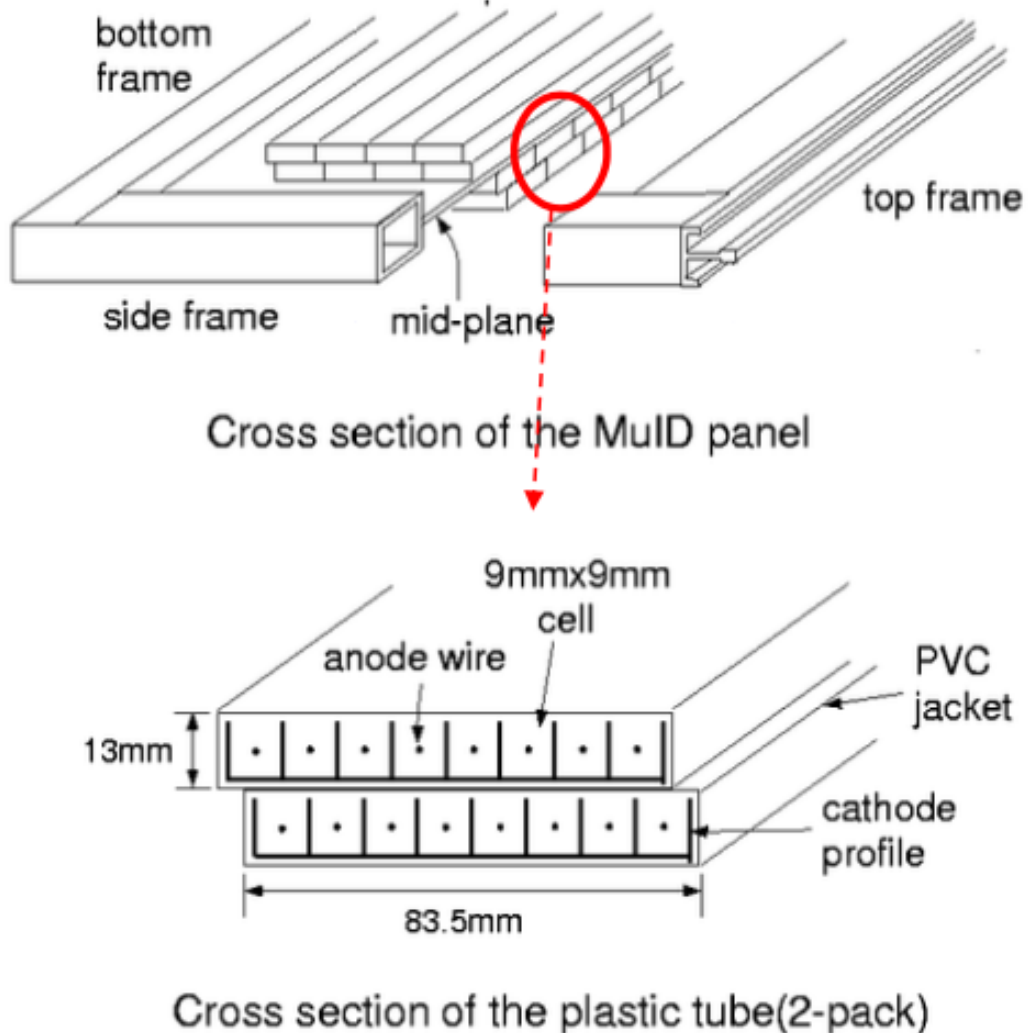


Figure 23: A drawing of one gap of the MuID. A gap consists of 4 large panels and 2 small panels as shown.



Cross section of the plastic tube(2-pack)

Figure 24: A drawing of Iarocci streamer tubes in the MuID.

FVTX is a silicon detector composed of two arms located on both end of VTX (a 4-layer barrel silicon vertex detector in the central arms). The rapidity coverage $1.2 < |\eta| < 2.4$ is very close to the existing south and north PHENIX muon arm rapidity coverage. There are four stations for each FVTX arm labeled as Station 0, 1, 2 and 3 as shown in figure 25. Within each station, there are $24 + 24$ silicon sensors (wedges) attached at the front and back side of the disk plane. The size of the wedges in station 0 is smaller than station 1, 2 and 3. Each wedge consists of two columns of mini-strips with $75 \mu\text{m}$ pitch in radial direction and 3.75 degree pitch in ϕ direction. There are 1.08 million mini-strips in total for FVTX and a group of 128-channel front end readout ASICs called FPHX chips are bonded to the mini-strips for signal transportation. Table 2 shows the summary of FVTX design parameters.

Table 2: Design parameters of FVTX.

Parameter	Design
Rapidity coverage	$1.2 < \eta < 2.4$
Polar angle coverage	360°
Strip pitch (μm)	75
Strip ϕ coverage	3.75°
Number of sensor wedges in a station	48
Strips per column for small and large sensor wedges	640, 1664
Inner radius of sensor wedges (mm)	44.0
Outer radius of sensor wedges (mm)	100.6, 170.0, 170.0, 170.0
Mean z -position of stations (mm)	201.1, 261.4, 321.7, 382.0
Nominal operating sensor bias (V)	+70

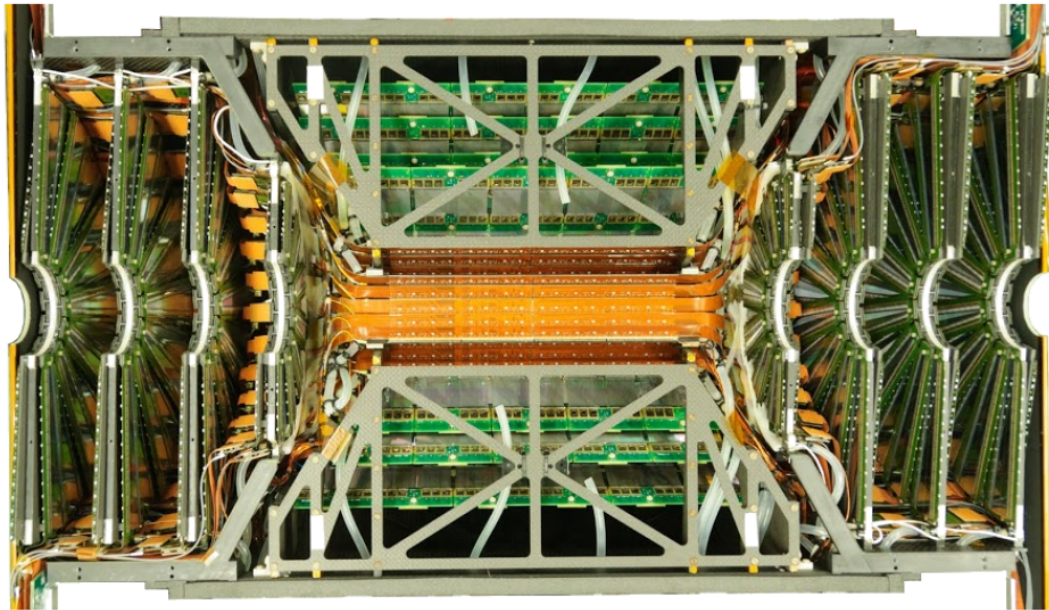


Figure 25: Half of FVTX assembled. Half-disks corresponding to the 4 stations of each arm with the VTX barrels in the center are shown. The total length is 80 cm.

3 Data and Analysis

3.1 Muon Arm Quality Assurance (QA)

Since the kinematic information for each J/ψ is reconstructed from the paired muons, the data of which are recorded by Muon Arm, it is essential to guarantee that the Muon Arm is performing well when taking the data. In this section, the PHENIX Muon Arm Quality Assurance (QA) procedure will be discussed. In order to check the Muon Arm detector status quantitatively, PHENIX has its own QA data file which stores information related with the quality of the Muon Arm performance.

This QA work has been done for $p+p$, $p+Al$ and $p+Au$ data. For each data set, we check the distributions of hot/dead planes, hot/dead packets, cluster number and cluster width. Suspicious runs are flagged for further investigation by the following criteria:

1. A plane is one half of with gap within one octant in Muon Tracker. Therefore, there are 48 planes in station 1 and 2, 32 planes in station 3. Figure 26 shows the average number of hits per event for each plane in station 1 in north arm. Hot planes are defined as number of hits more than 1 standard deviation away from the mean number of hits over all planes and dead packets are defined as no hits at all. Figure 27 shows the hot and dead planes distribution in north arm with $p + p$ data. A threshold at 2 for both hot

and dead planes are set.

2. A packet is a stream of data that stores the information of hits from a specific area of the Muon Tracker. There are 192 packets for north arm and 168 packets for south arm. Figure 28 shows the number of hit per event in each packet. Hot packets are defined as number of hits more than 2 standard deviation away from the mean hits of all the packets and dead packets are defined as no hits at all in the packets. Figure 29 shows the hot and dead packets distribution in south arm with $p+p$ data. A threshold at 5 for both hot and dead packets are set.
3. Cluster number: A cluster is a bunch of electrons ionized by a charged particle and detected by a cathode in Muon Tracker. Count the number of cluster in each Muon arm station cluster number. The distribution of cluster number for all runs are shown in figure 30. Runs with zero or very high cluster number were flagged out.
4. Mean cluster width: The clusters width is the width of cluster distribution which follows a Landau distribution. Mean cluster width is the average cluster width in one station within one run. The runs with low (less than 1) or zero cluster width were flagged out. Figure 31 shows the mean cluster width distribution for station 1 in south arm.
5. Dimuon production rate distribution (figure 32)for each run: Runs within

three standard deviation around over all mean dimuon production rate were kept. In Dimuon production rate case, unlike sign charge and BBC Z vertex less than 30 cm cuts were applied for each arm. Then get the total number of dimuon within the invariant mass range from 2 GeV to 5 GeV. This number is treated as total number of dimuon. On the other hand, live trigger count of "BBCLL1(>0 tubes) novertex" got from PHENIX Run15 control log were treated as total number of events. The production rate is the number of dimuon divided by live trigger count of "BBCLL1(>0 tubes) novertex" for each run.

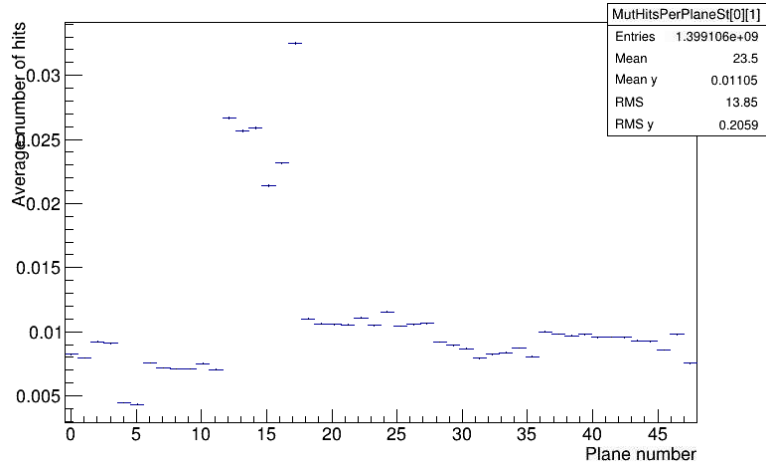


Figure 26: Number of hit in each plane for Run 432008 in North arm with $p + p$ data.

For the runs flagged out in the first step, the QA Mutr Radial hits plots were checked. Also, the relevant shift leader comments as well as trigger live time were reviewed. Runs with low trigger live time (less than 30%) were rejected. After an

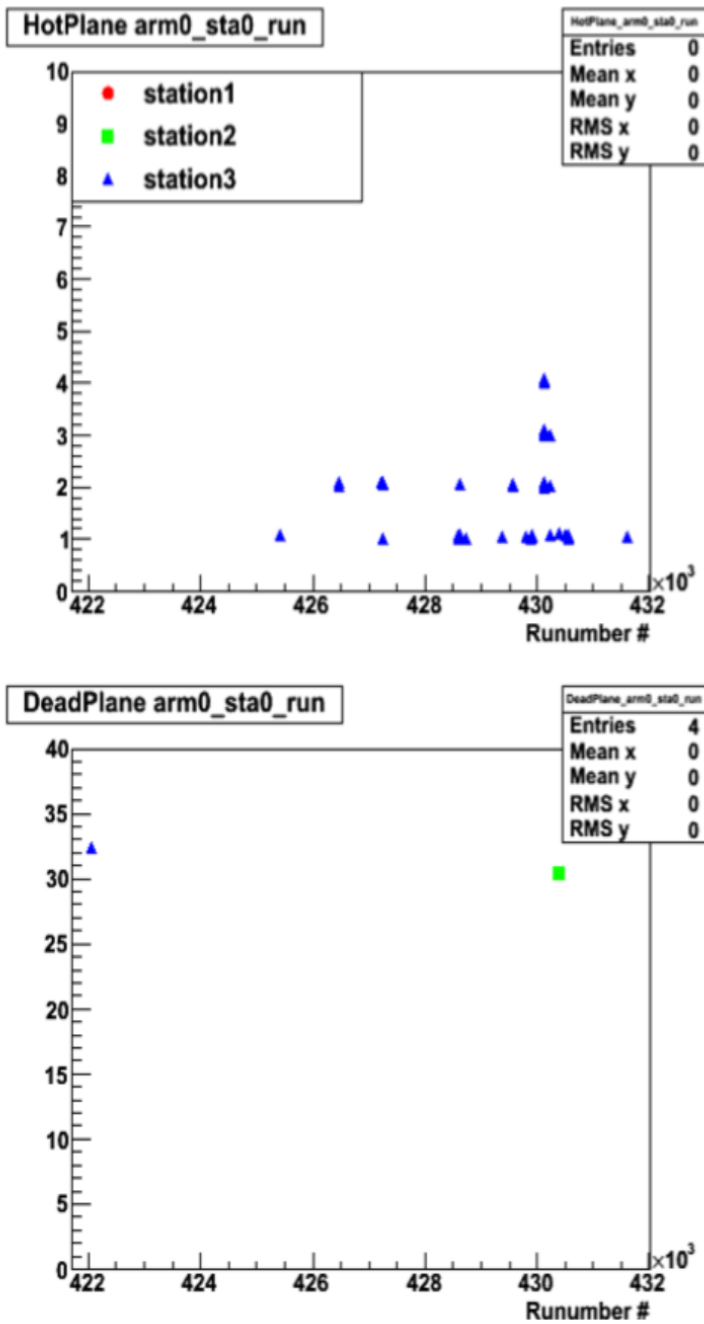


Figure 27: The top (bottom) plot shows the number of hot (dead) planes in each run for North arm with $p + p$ data.

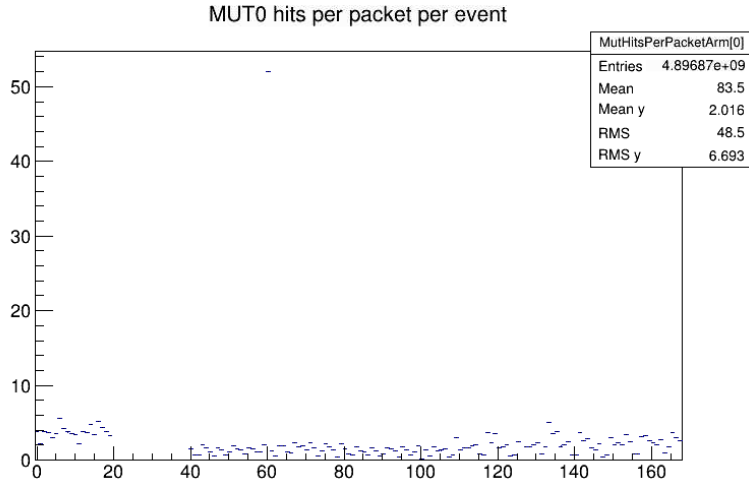


Figure 28: Number of hit in each packet for Run 432008 in North arm with $p + p$ data.

initial run duration time cut at around 10 mins, 751 runs remained for $p + p$ data.

In the next step, the flagged runs with reasonable QA Mutr Radial hit plot will be kept .

Since this analysis involves spin information which is stored in the PHENIX Spin Database, any runs with missing spin and/or luminosity information will be also removed from the dataset.

3.1.1 Run selection with $p + p$ data

The following runs were excluded:

- Removed runs due to the missing of Spin patterns or BBCin count in Spin Database:

424877 425011 425403 425747 425763 427129 427136 427137 428265 428607 428717

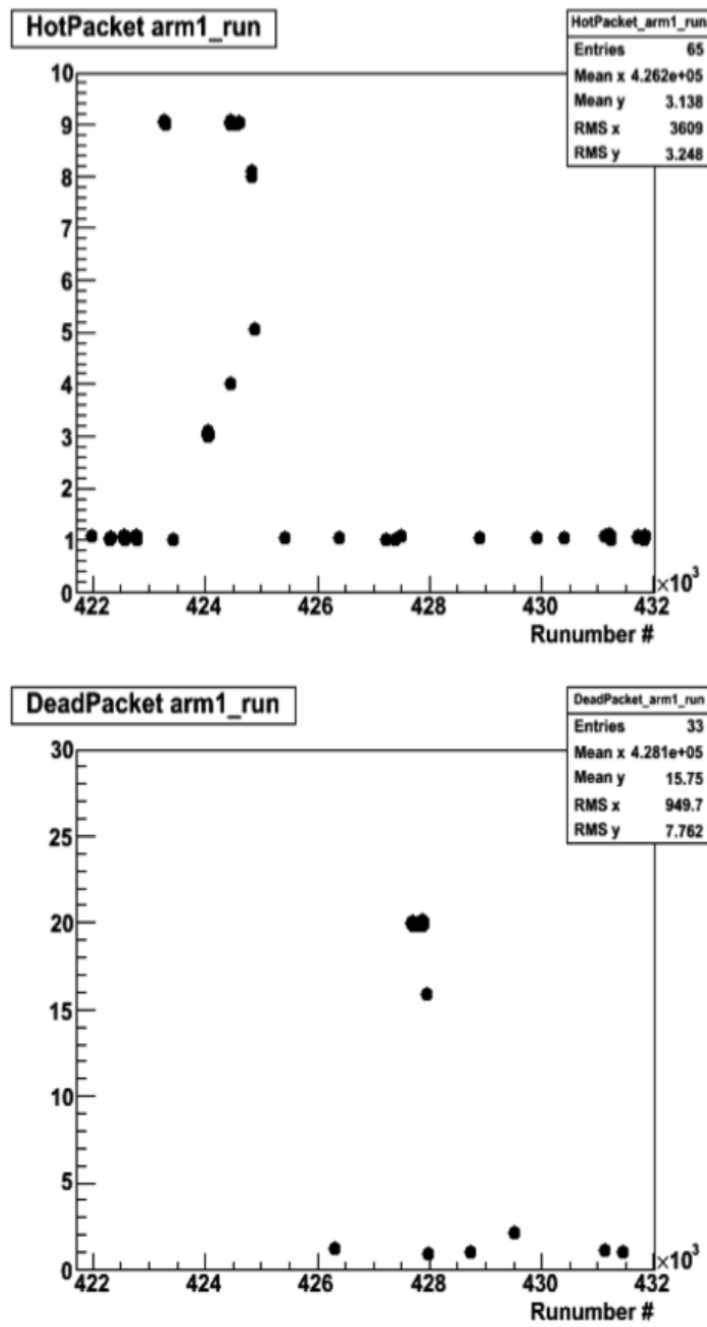


Figure 29: The top (bottom) plot shows the number of hot (dead) packets in each run for South arm with $p + p$ data.

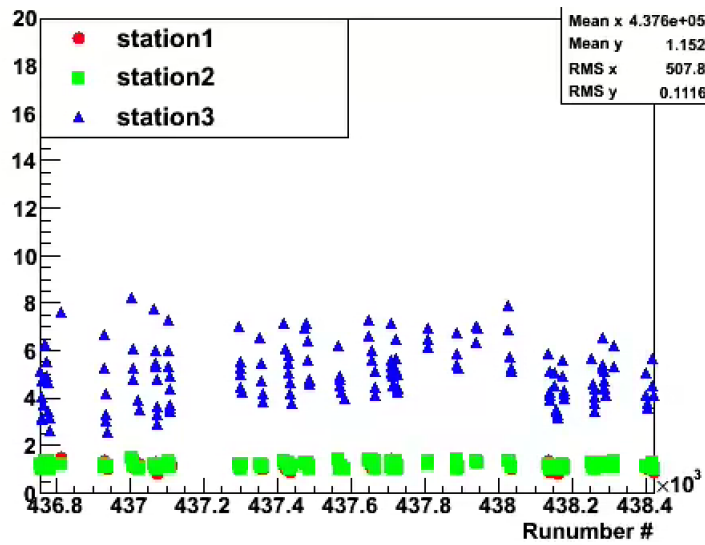


Figure 30: Number of cluster distribution for North arm with $p + p$ data.

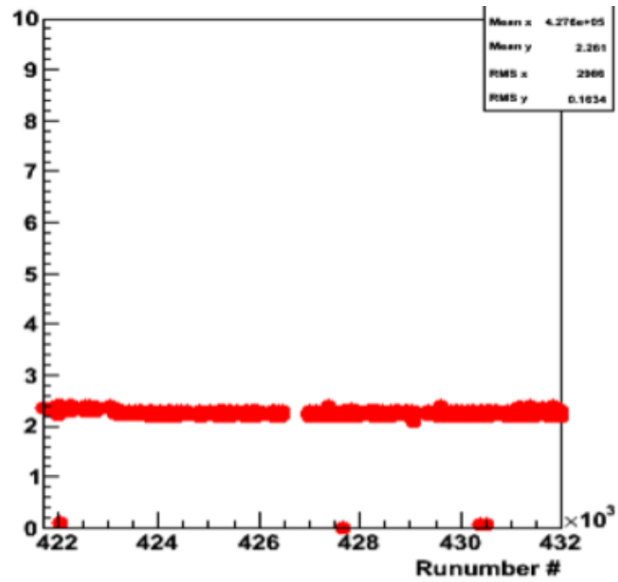


Figure 31: Cluster width distribution for South arm in station 1 with $p + p$ data.

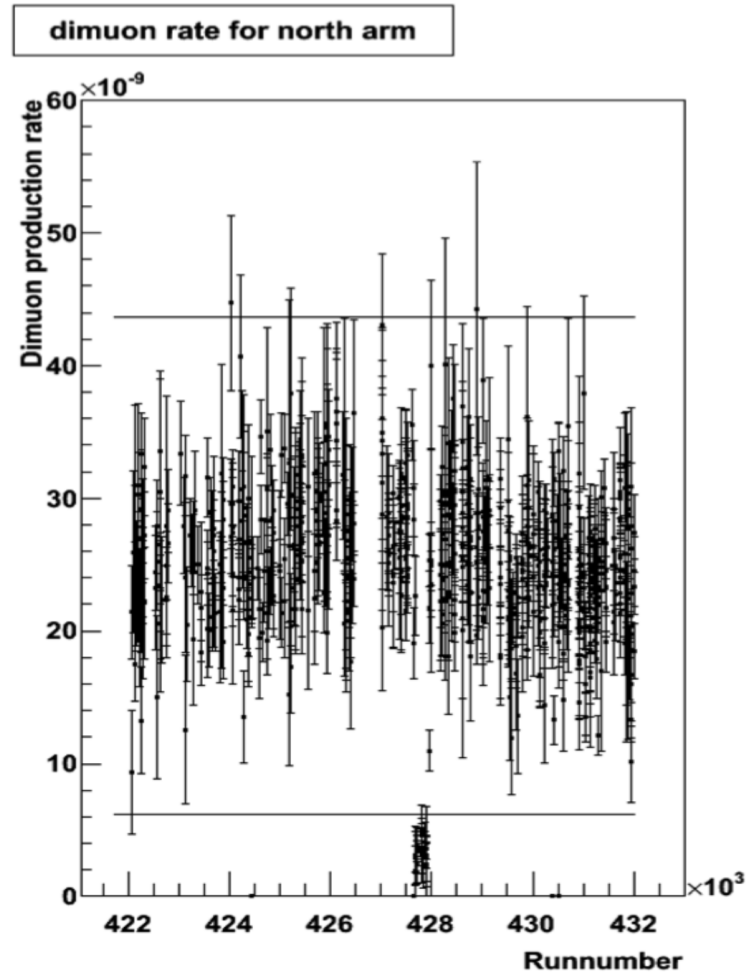


Figure 32: Dimuon production rate distribution for North arm with $p + p$ data.

429503 429590 430607 431026 431932

- Removed runs due to abnormal BBCin count in Spin Database:

426308 426353 431831 431832 431833 431834 431835 431837 431840 431845 431846
431859 431860 431886 431888

- Removed runs due to Zero BBCin count in Spin Database:

426313 426315 426316 426319 426320 431854

- Removed runs due to high number of dead packets, or dimuon yield per minimum bias events is too low or too high:

427670 427671 427672 427673 427674 427708 427710 427711 427712 427713 427805
427806 427807 427811 427813 427814 427815 427829 427878 427879 427881 427882
427885 427886 427887 427964 430402 430519 427656 425423 429886 429887 430402
430519 427656

- Removed runs due to increasing polarization in same fill:

424227

- Removed runs due to no diumion events after BBC z-vertex and dimuon charge cuts:

424439

- Removed runs due to short duration (less than about 10 mins):

422074 422084 422319 422531 422562 422640 423041 423311 423546 423549 423576
 424443 424627 424759 424886 425168 425290 425583 425688 426443 427129 427136
 427264 427362 427366 427377 427657 427658 427673 427709 427810 427883 427968
 427979 428211 428255 428260 428264 428266 428318 428323 428324 428451 428601
 428728 428730 428733 428737 428754 428758 428892 429022 429024 429127 429365
 429595 429678 429680 429696 429798 429888 430119 430121 430136 430137 430239
 430494 430522 430563 430594 430600 430905 430906 431125 431137 431437 431608
 431609 431836 431839 431844 431894

3.1.2 Run selection with $p + \text{Au}$ data

The following runs were excluded:

- Removed runs due to missing Spin patterns and BBCin count in Spin Database:

432641 433266 434147 434148 434150 434151 434699 434909 434982 434983 435939
 434980 434981 434984

- Removed runs due to abnormal BBCin count in Spin Database:

435361

- Removed runs due to increasing polarization in same fill:

434360 434362 434363 434364 435525 435526 435527 435528 435529 435530 435601
 435606 435826 435828 435832 435836 435841

3.1.3 Run selection with $p + \text{Al}$ data

The following runs were excluded:

- Removed runs due to abnormal BBCin count in Spin Database:

437101 437714 438033 438153

- Removed runs due to high number of dead packets, or dimuon yield per minimum bias events is too low or too high:

South Arm: 437353 437356 437358 437361 437362 437417 437421 437430 437431

437433 437434 437435 437440 437474 437478 437483 437484 437486 437487 437488

437568 437569 437572 437573 437574 437575 437583 437649 437650 437658 437659

North Arm: 437433

3.2 Event and Track Selection

Having finished the quality assurance described in the previous section, a set of analysis cuts are placed on a track by track basis. The same cuts are applied for $p + p$, $p + \text{Al}$ and $p + \text{Au}$ cases. The purpose of applying the cuts is to reduce the background under the J/ψ mass region as much as possible. The kinematic variables, their descriptions and the basic single muon cuts applied in this analysis are listed as follows:

- $DG0 < 25 \text{ cm (N), } DG0 < 30 \text{ cm (S)}$: Distance between the projected MuTr track and the MuID road at the gap 0 z position in cm.

- $DDG0 < 10$: Deviation of the slopes of the MuTr track and the MuID road at the gap 0 z position in degrees.
- MuonID hits > 5 : Number of MuID hits recorded.
- MuTr hits > 9 : Number of MuTr hits recorded.
- last gap > 2 : MuID gap that the muon penetrates which ensure muons going through all MuID steel.
- MuTr $DCA_r < 10$: The distance of closest approach between a muon track and the beam line.
- same event == 1: Single-track candidates for dimuon reconstruction come from one event (collision).

The kinematic and track quality cut and their descriptions for dimuon are listed as follows:

- BBC z -vertex: $-30 < z < 30$ cm: BBC-determined z component of interaction vertex position.
 - charge = 0: The total charge of paired dimuon.
 - $0.42 \text{ GeV} < p_T < 10 \text{ GeV}$: The transverse momentum of dimuon.
 - $p_z < 100 \text{ GeV}$: The longitudinal momentum of dimuon.
 - Forward and backward pseudo-rapidity ($1.2 < |y| < 2.2$): Pseudorapidity of the muon track falls within forward arm acceptance.
 - vertex $\chi^2 < 5$: Track fit quality to the primary vertex.
- A $p_T < 0.42 \text{ GeV}$ low side cut is applied considering the resolution of forward

muon arms. The resolution is obtained from PYTHIA6 simulation where the difference between input and output p_x and p_y distributions are plotted and shown in figure 33.

In order to check how this low side p_T cut would effect the statistics, the p_T distribution plots have been drawn in figure 34. These plots show that the low side p_T cut will just cut off less than 1% of the dimuons.

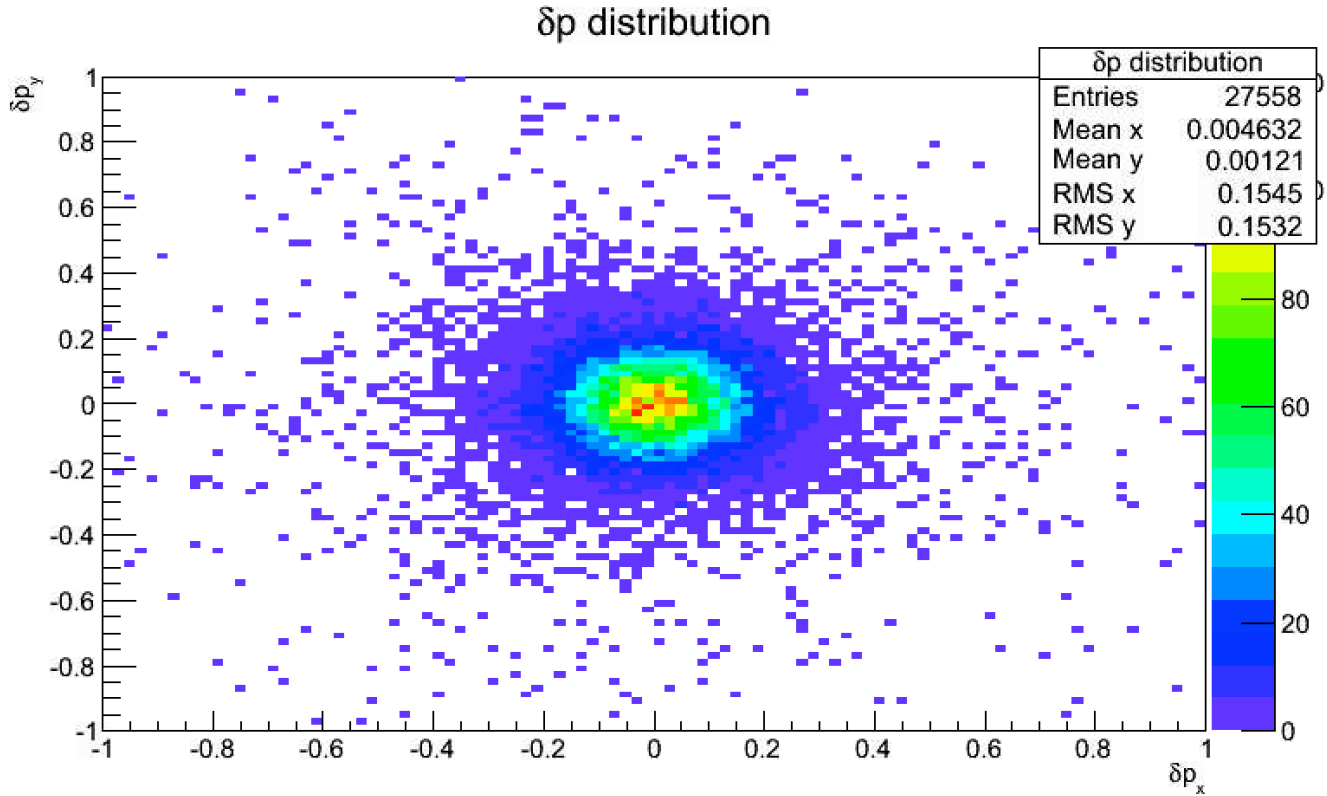


Figure 33: δp_x and δp_y are obtained by finding the difference between input and output p_x , p_y in PYTHIA6 simulation. A 2σ cut (0.3 GeV) is made.

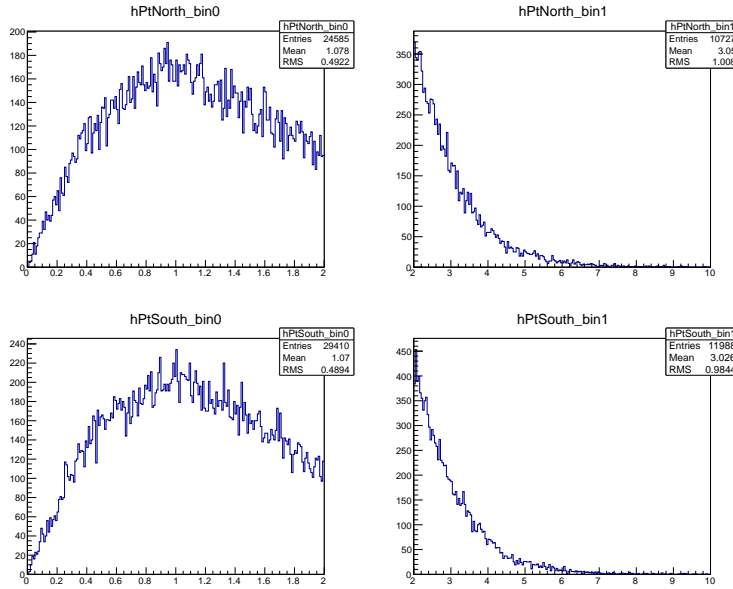


Figure 34: p_T distribution for North arm (top) and South arm (bottom) in $p + p$ data.

3.3 J/ψ Transverse Single Spin Asymmetry

The physics J/ψ double spin asymmetry cannot be measured directly from the data due to the present of background particles under the J/ψ mass peak which pass the event and track selection. Equations 34 and 35 show how the J/ψ double spin asymmetry and the corresponding statistical uncertainty are calculated.

$$A_N^{J/\psi} = \frac{A_N^{incl} - f \cdot A_N^{bgr}}{1 - f} \quad (34)$$

$$\delta A_N^{J/\psi} = \frac{\sqrt{(\delta A_N^{incl})^2 + f^2 \cdot (\delta A_N^{bgr})^2}}{1 - f} \quad (35)$$

Here, $f = N^{BG}/N^{inel}$ is the background fraction which can be obtained from the previous section; A_N^{inc} is the inclusive dimuon asymmetry within 2σ mass window cut which can be gotten from GPR fitting; and $A_N^{bgr.}$ is the background asymmetry which we estimate from the low side band dimuon and the mass range of which is from 1.5 GeV to 2.4 GeV. Since the background dimuons under the J/ψ peak can not be extracted, the low side band dimuon was picked to represent the $A_N^{bgr.}$ under the J/ψ peak by assuming that the $A_N^{bgr.}$ in a neighboring dimuon mass range are equal. A potential systematic uncertainty due to this assumption will be shown in a later chapter.

3.4 Background Fraction

The Gaussian Process Regression (GPR) method is used to fit the background shapes without supposing a prior functional form. The invariant mass distribution of the background events follows a stochastic process, so it is difficult to verify that a given functional form for the background distribution is better over another one. In the GPR method, each data point is treated as a random variable following a Gaussian Distribution. Between each pair of the data points, there exist a correlation which, mathematically, requires an N -dimensional Gaussian distribution, with an $n \times n$ covariance matrix representing how the data should move together. Here N is the number of data points. The correlation of two data points can be gotten by assuming a kernel function. In my analysis, the Radial

Basis Function (RBF) kernel was chosen; the RBF kernel is given by:

$$k(x_i, x_j) = \sigma_f^2 \exp\left(-\frac{(x_i - x_j)^2}{2l^2}\right) + \sigma_i^2 \delta(x_i - x_j), \quad (36)$$

where σ_i is the uncertainty on point i , $\delta(x_i - x_j)$ is the Kronecker delta and σ_f and l are hyperparameters for this covariance function. Eq. 36 shows that the further away two points are, the less correlation they will have. This is intuitively right because closer the points are the similar they would present. The second term guarantees that the uncertainty from each point contribute only when we calculate the covariance of a point with itself.

The probability of observing one outcome y given features x and hyperparameters is shown as following:

$$\log p(y|x, \theta) = -\frac{1}{2}y^T K^{-1}y - \frac{1}{2}\log|K| - \frac{n}{2}\log 2\pi \quad (37)$$

Then, basing on the theory of maximum likelihood estimation, the hyperparameters can be determined by running multivariate optimization algorithms.

Having chosen the kernel and determined the hyperparameters, the covariance information from the data set can be encoded into a matrix \mathbf{K} :

$$\begin{bmatrix} k(x_1, x_1) & k(x_1, x_2) & \dots & \dots & k(x_1, x_n) \\ k(x_2, x_1) & k(x_2, x_2) & \dots & \dots & k(x_2, x_n) \\ \vdots & \vdots & \vdots & k(x_i, x_j) & \vdots \\ k(x_n, x_1) & k(x_n, x_2) & \dots & \dots & k(x_n, x_n) \end{bmatrix} \quad (38)$$

The GPR assumes that all the data points follows a multivariate Gaussian Distribution with a zero mean and covariance matrix given by the $\mathbf{n} \times \mathbf{n}$ matrix \mathbf{K} (eq. 38). The joint distribution of given data points \mathbf{y} and a given prediction point y_* can be gotten by extending the \mathbf{n} -dimensional Gaussian distribution:

$$\begin{bmatrix} \mathbf{y} \\ y_* \end{bmatrix} \propto N \left(0, \begin{bmatrix} K & K_*^T \\ K_* & K_{**} \end{bmatrix} \right) \quad (39)$$

where $K_* = [k(x_*, x_1), \dots, k(x_*, x_n)]$ and $K_{**} = k(x_*, x_*)$. [EQUATION 35 doesn't make sense. On the left-hand-side you have a $n+1$ vector, on the right-hand-side is some sort of matrix. ???[This is a way to represent multivariant gaussian distribution. The matrix inside shows the correlation between each point in the data set]]

The method of predicting one point by giving a set of known data points is involved with the conditional probability. A detailed description of calculating the prediction point y_* using the conditional probability is shown in ref. [72]:

$$\bar{y}_* = K_* K^{-1} y \quad (40)$$

$$var(y_*) = K_{**} - K_* K^{-1} K_*^T \quad (41)$$

Notice that this procedure relies on the covariance matrix \mathbf{K} being invertible.

In the context of J/ψ background study, the training (given) data points are in the 1.5-2.2 GeV and 4.3-6.0 GeV invariant mass ranges in order to exclude the

J/ψ and ψ' contributions to the mass spectrum and include only the data points that should correspond to background for the analysis.

For the J/ψ invariant mass fit, the background which is gotten from GPR is extracted from real data points. Then the J/ψ is fitted with a Crystal Ball function [77] while the ψ' is fitted with a Gaussian function. The explicit form of Crystal Ball function is shown as follow:

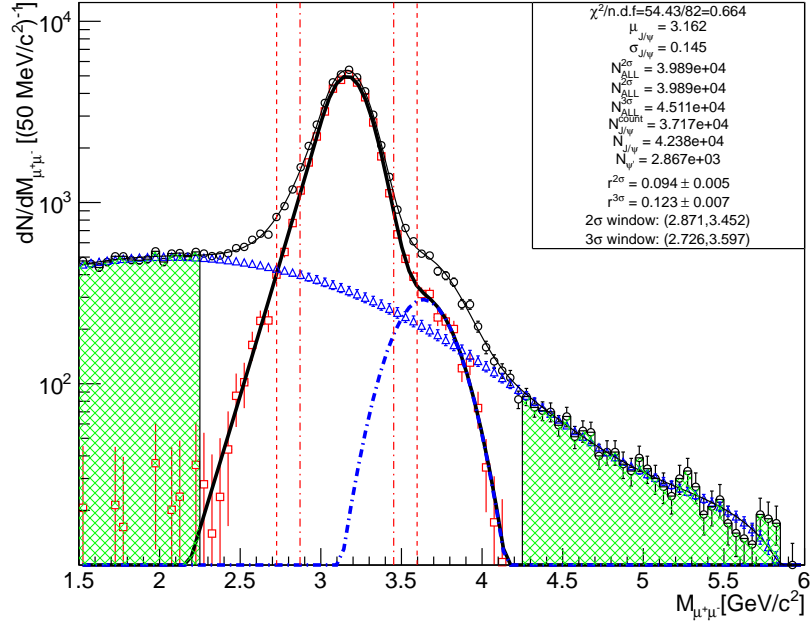
$$f(x; \alpha, n, \bar{x}, \sigma) = N \cdot \begin{cases} \exp\left(-\frac{(x - \bar{x})^2}{2\sigma^2}\right), & \text{for } \frac{x - \bar{x}}{\sigma} > -\alpha \\ A \cdot \left(B - \frac{x - \bar{x}}{\sigma}\right)^{-n}, & \text{otherwise} \end{cases} \quad (42)$$

where $A = (\frac{n}{|\alpha|})^n \cdot \exp(-\frac{|\alpha|^2}{2})$, $B = \frac{n}{|\alpha|} - |\alpha|$, $N = \frac{1}{\sigma(C+D)}$, $C = \frac{n}{|\alpha|} \cdot \frac{1}{n-1} \cdot \exp(-\frac{|\alpha|^2}{2})$, $D = \sqrt{\frac{\pi}{2}}(1 + \text{erf}(\frac{|\alpha|}{\sqrt{2}}))$.

In this analysis, we fit dimuon invariant mass in three different p_T bins for both North and South arms which are $p_T \in (0 - 10)$ GeV, $p_T \in (0 - 2)$ GeV, $p_T \in (2 - 10)$ GeV for $p + p$, $p + \text{Al}$ and $p + \text{Au}$ data. At the same time, two x_F bins were chosen by making the statistics of each x_F bin in $2\sigma J/\psi$ mass window equal. The x_F binning for $p + p$, $p + \text{Al}$ and $p + \text{Au}$ data is $x_F \in (0.05 - 0.11)$ and $x_F \in (0.11 - 0.30)$. The background fraction is calculated within a $2\sigma J/\psi$ mass window.

Figures 35 to 39 show the GPR fitting for $p + p$ data, figures 40 to 44 show the GPR fitting for $p + \text{Au}$ data and figures 45 to 49 show the GPR fitting for $p + \text{Al}$ data. All the plots show a clear peak which indicates that J/ψ particles are dominant around the $2\sigma J/\psi$ invariant mass window.

BinningMode_1_Arm0_Charge0_bin0.0_10.0



BinningMode_1_Arm1_Charge0_bin0.0_10.0

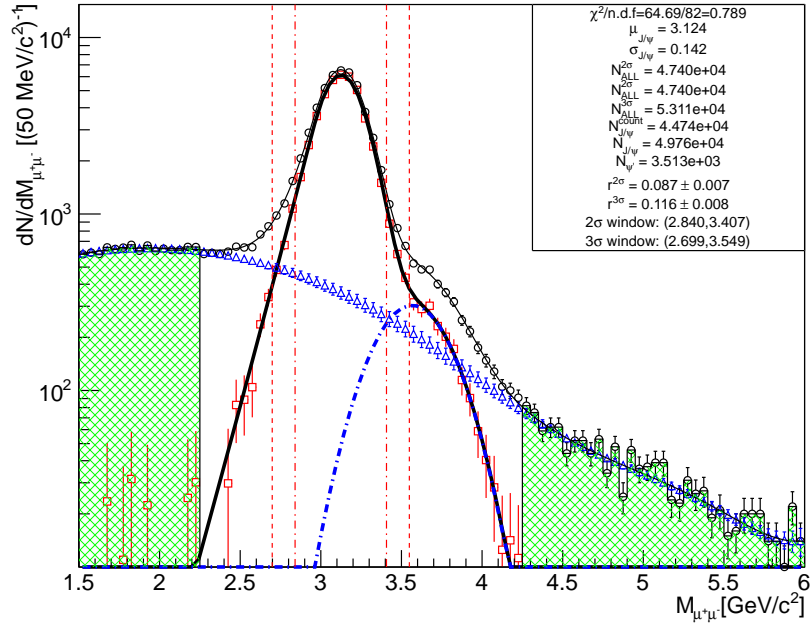
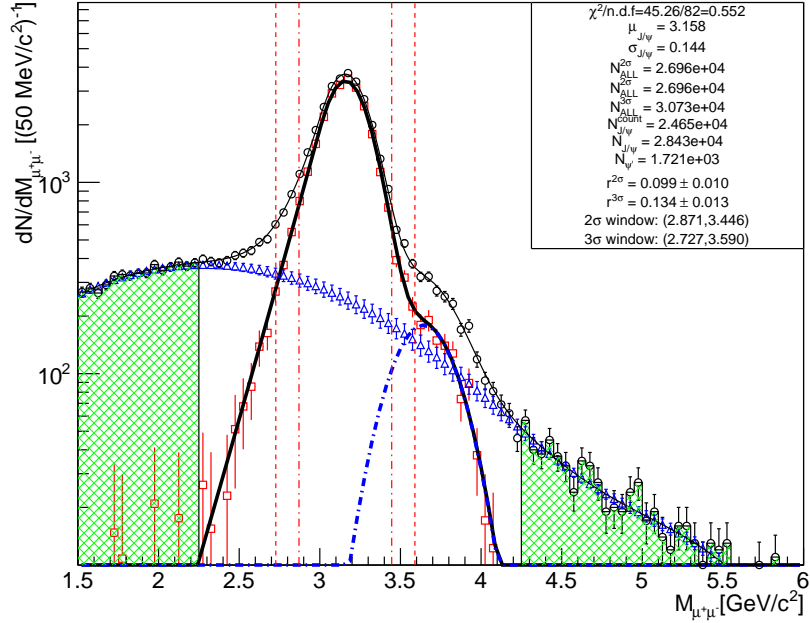


Figure 35: MuTr mass spectrum fits with GPR background estimation for $p_T = 0 - 10 \text{ GeV}$ bin for the north (top) and south (bottom) arm with $p + p$ data

BinningMode_1_Arm0_Charge0_bin0.0_2.0



BinningMode_1_Arm1_Charge0_bin0.0_2.0

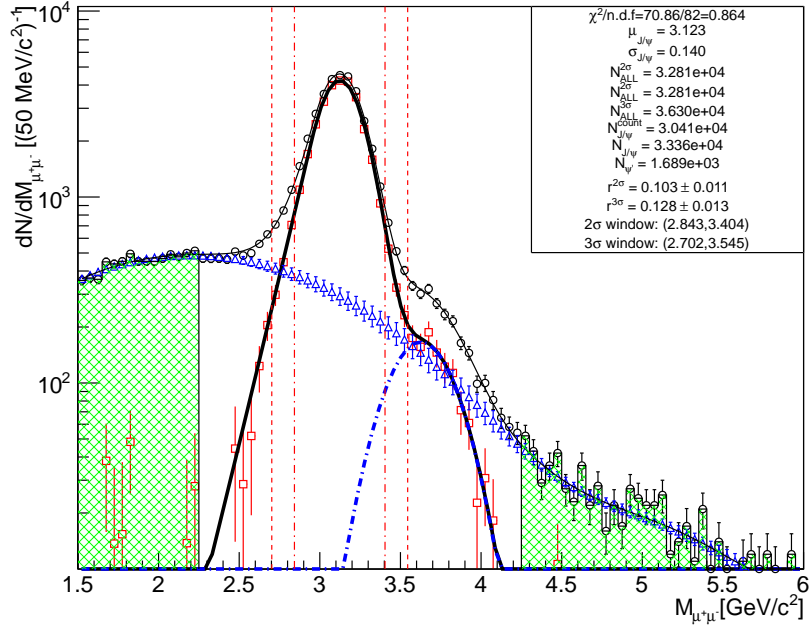
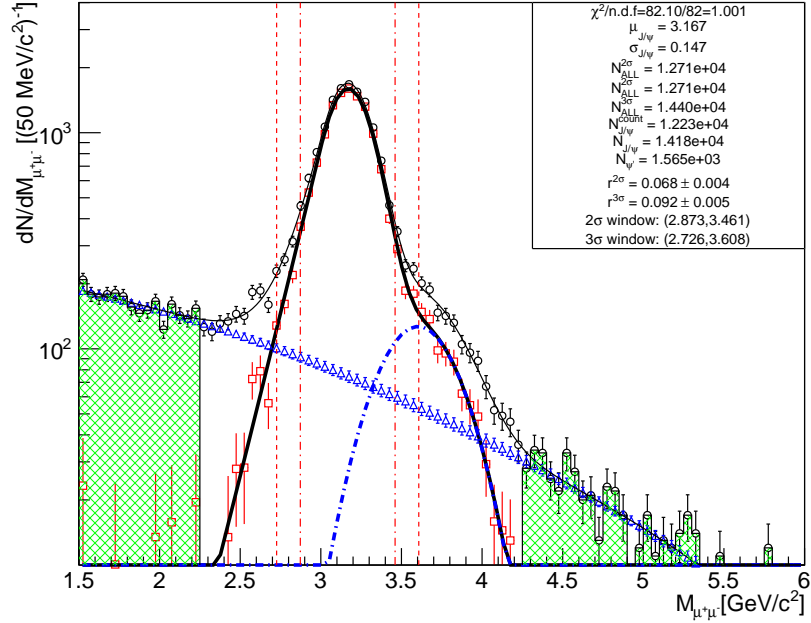


Figure 36: MuTr mass spectrum fits with GPR background estimation for $p_T = 0 - 2 \text{ GeV}$ bin for the north (top) and south (bottom) arm with $p + p$ data

BinningMode_1_Arm0_Charge0_bin2.0_10.0



BinningMode_1_Arm1_Charge0_bin2.0_10.0

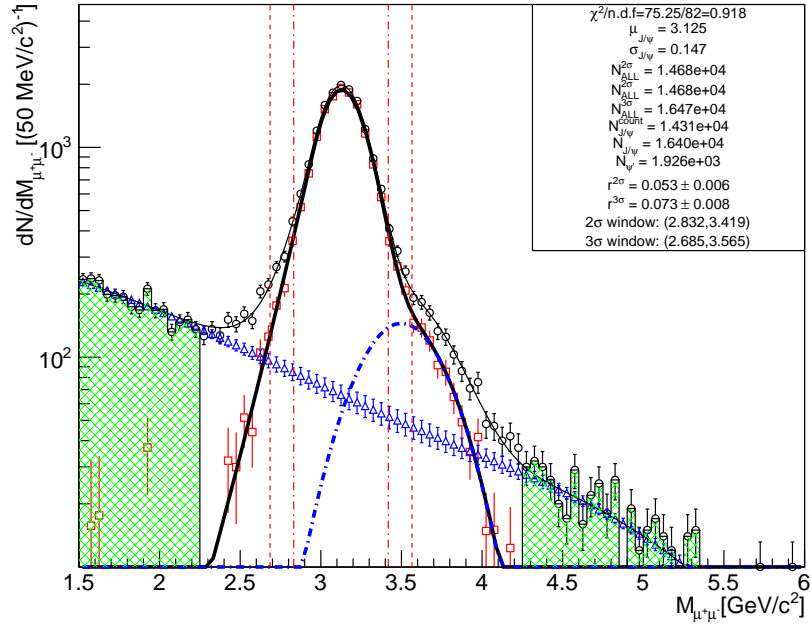
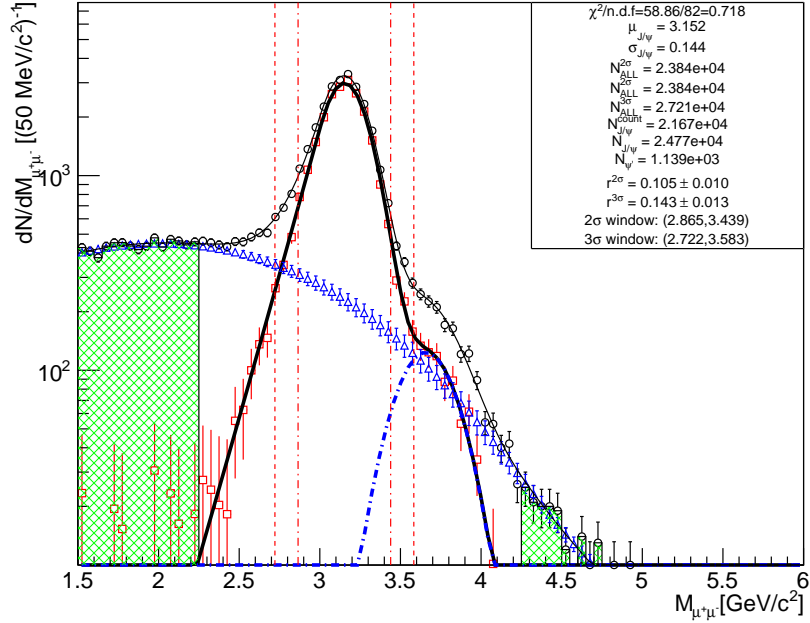


Figure 37: MuTr mass spectrum fits with GPR background estimation for $p_T = 2 - 10 \text{ GeV}$ bin for the north (top) and south (bottom) arm with $p + p$ data

BinningMode_2_Arm0_Charge0_bin0.1_0.1



BinningMode_2_Arm1_Charge0_bin0.1_0.1

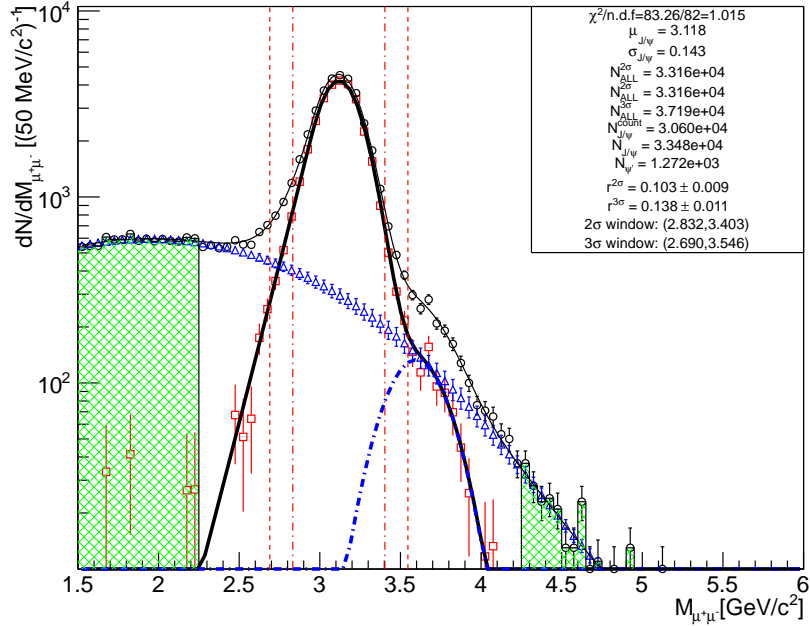
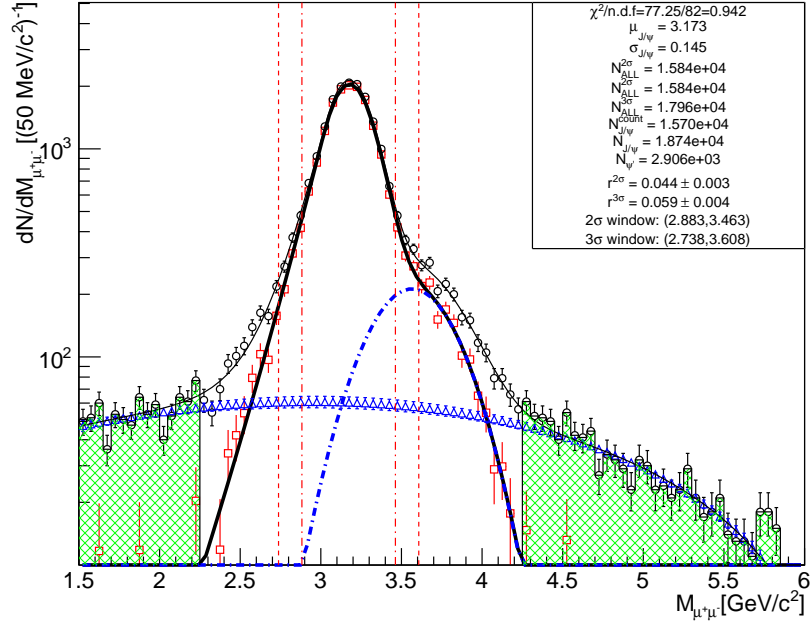


Figure 38: MuTr mass spectrum fits with GPR background estimation for $x_F = 0.05 - 0.11$ bin for the north (top) and south (bottom) arm with $p + p$ data

BinningMode_2_Arm0_Charge0_bin0.1_0.3



BinningMode_2_Arm1_Charge0_bin0.1_0.3

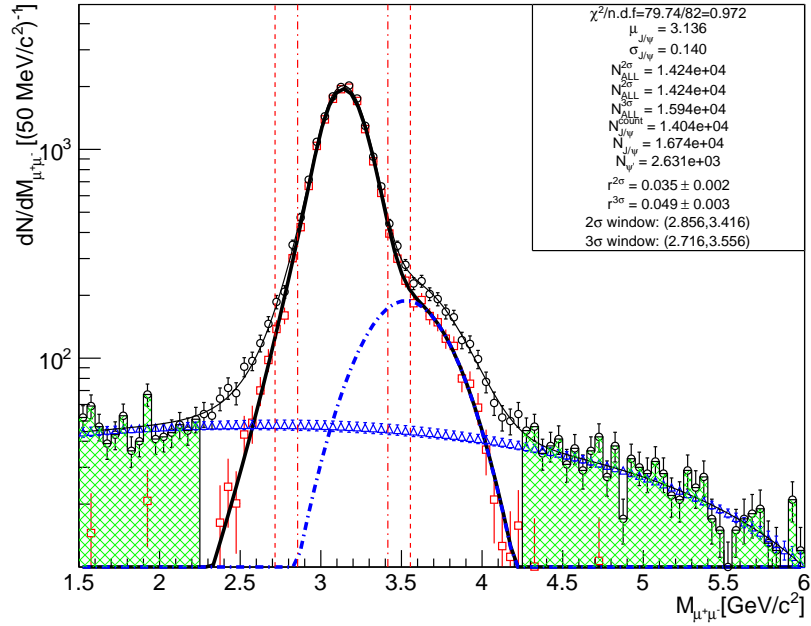
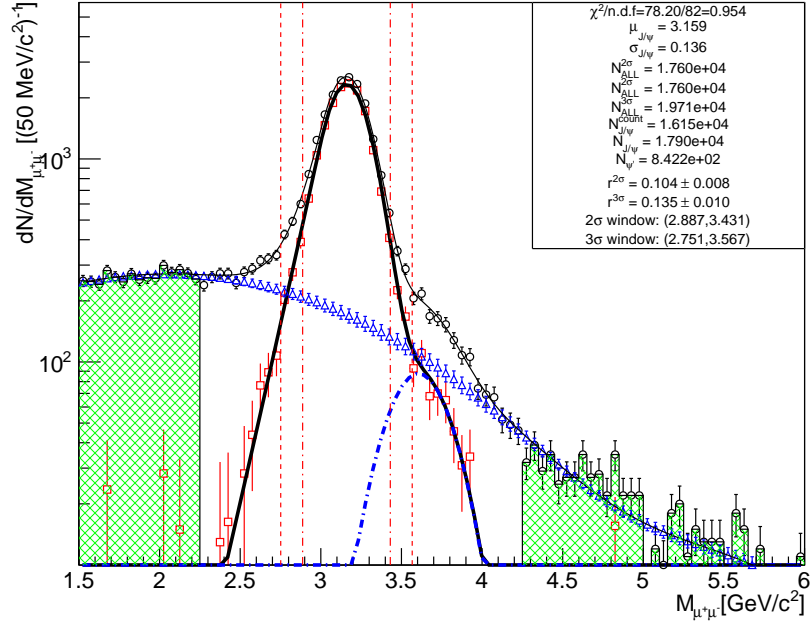


Figure 39: MuTr mass spectrum fits with GPR background estimation for $x_F = 0.11 - 0.30$ bin for the north(top) and south(bottom) arm with $p + p$ data

BinningMode_1_Arm0_Charge0_bin0.0_10.0



BinningMode_1_Arm1_Charge0_bin0.0_10.0

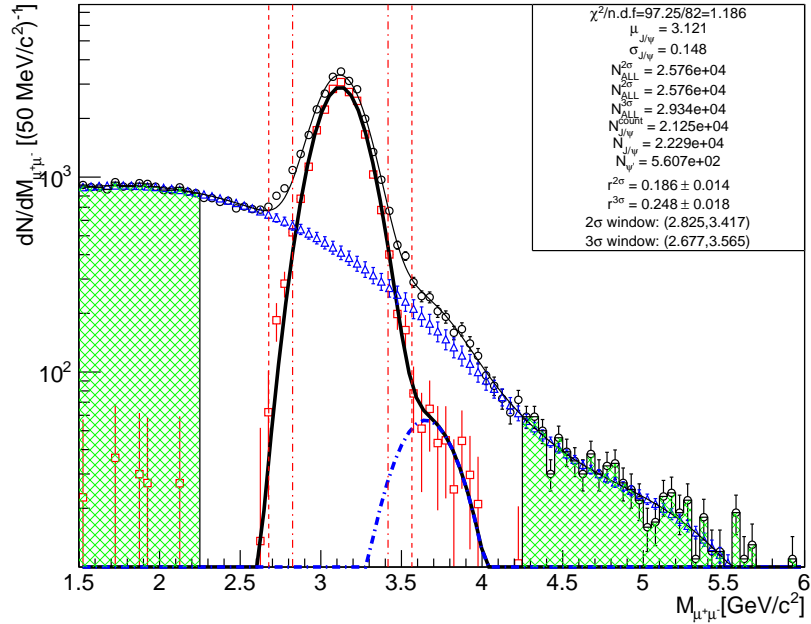
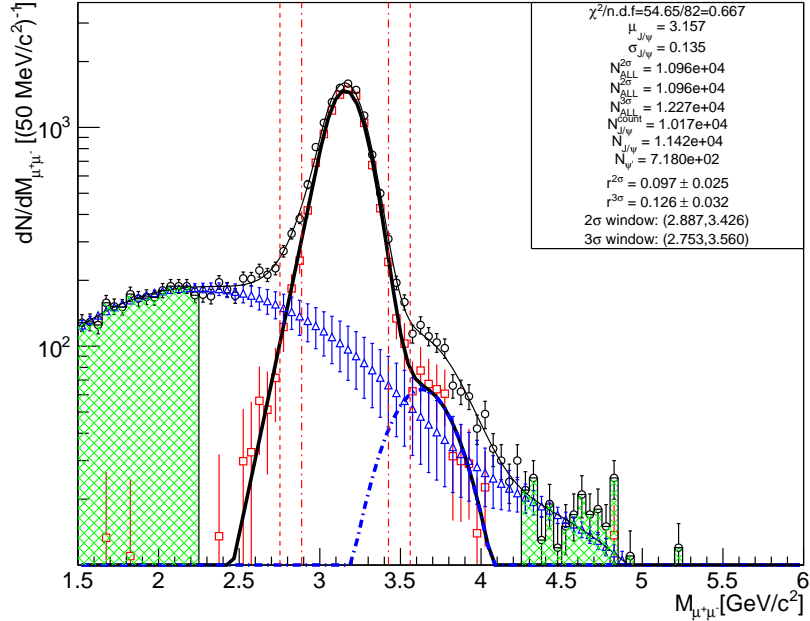


Figure 40: MuTr mass spectrum fits with GPR background estimation for $p_T = 0 - 10 \text{ GeV}$ bin for the north (top) and south (bottom) arm with $p + \text{Au}$ data

BinningMode_1_Arm0_Charge0_bin0.0_2.0



BinningMode_1_Arm1_Charge0_bin0.0_2.0

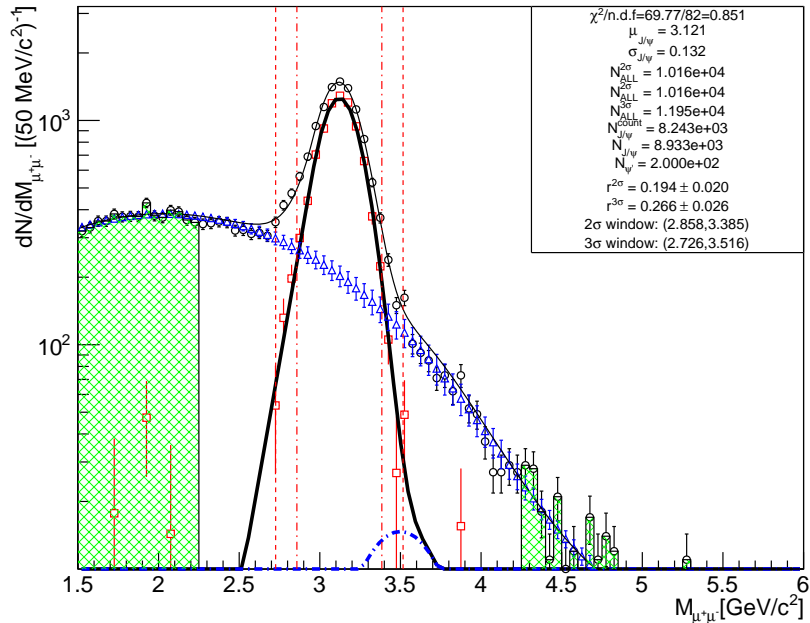
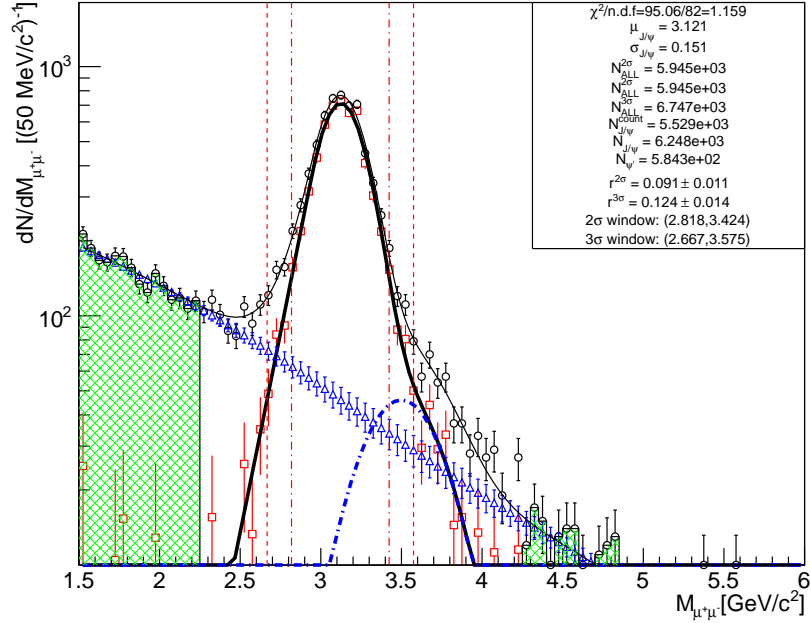


Figure 41: MuTr mass spectrum fits with GPR background estimation for $p_T = 0 - 2 \text{ GeV}$ bin for the north (top) and south (bottom) arm with $p + \text{Au}$ data

BinningMode_1_Arm1_Charge0_bin2.0_10.0



BinningMode_1_Arm1_Charge0_bin2.0_10.0

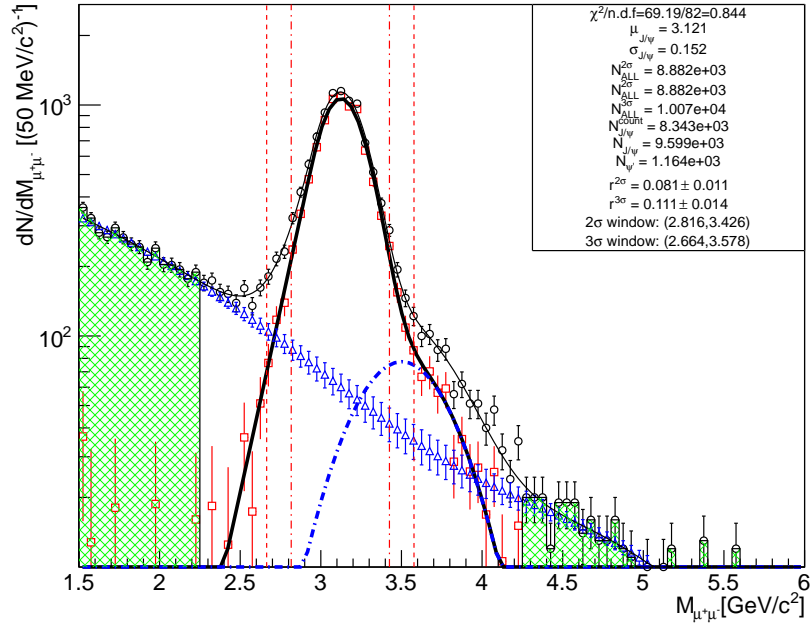
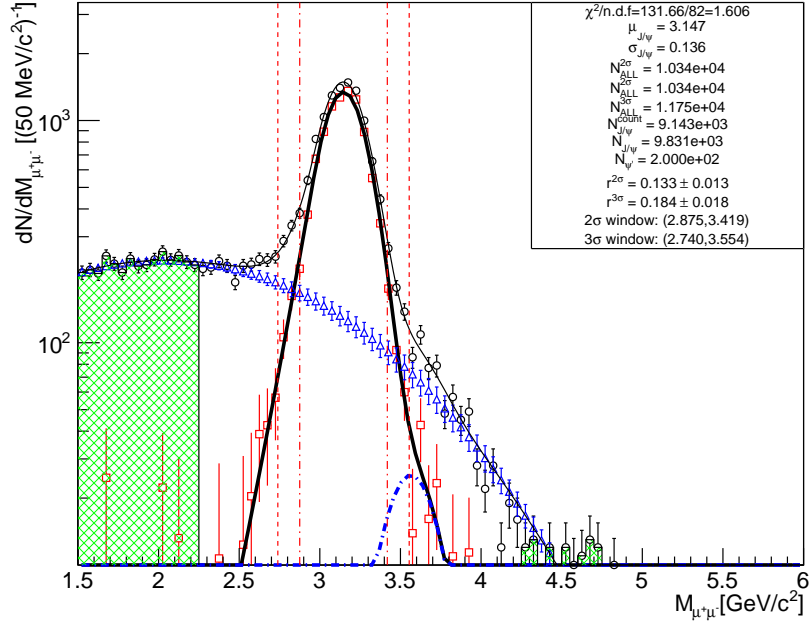


Figure 42: MuTr mass spectrum fits with GPR background estimation for $p_T = 2 - 10 \text{ GeV}$ bin for the north (top) and south (bottom) arm with $p + \text{Au}$ data

BinningMode_2_Arm0_Charge0_bin0.1_0.1



BinningMode_2_Arm1_Charge0_bin0.1_0.1

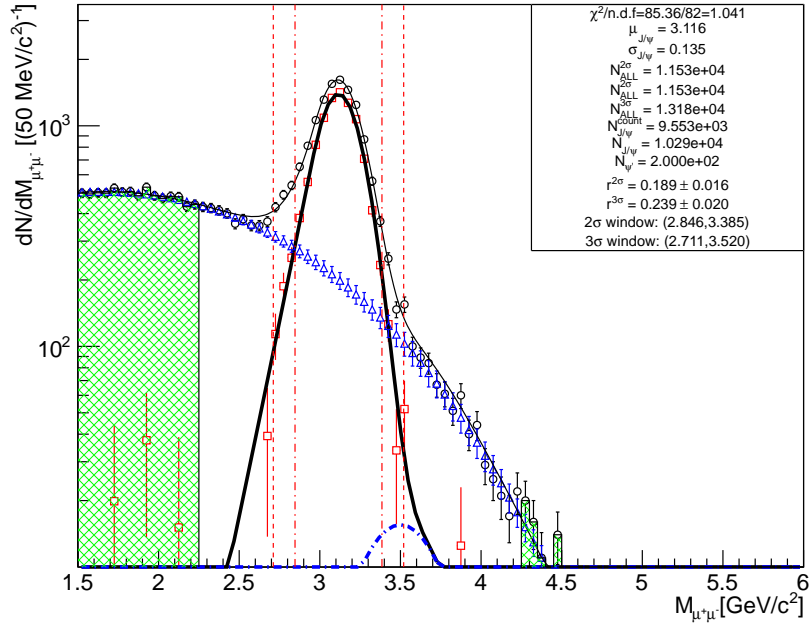
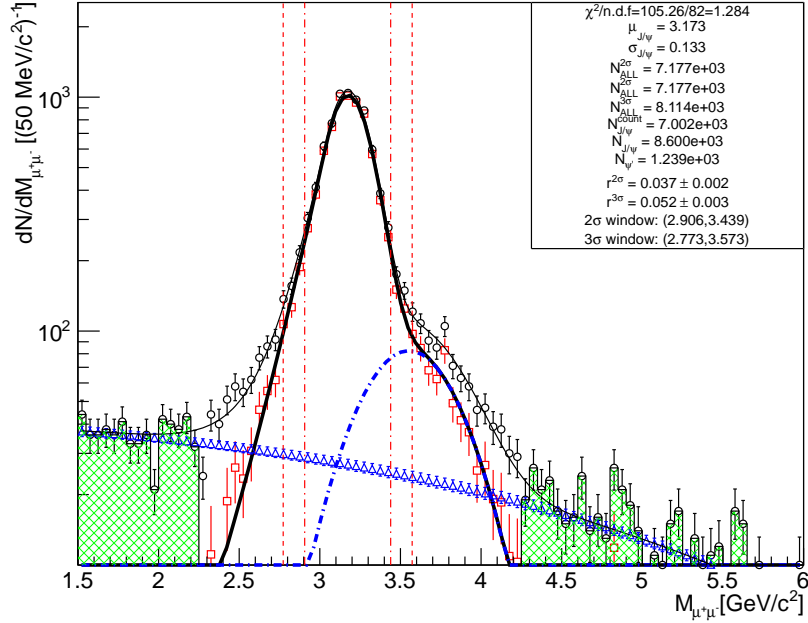


Figure 43: MuTr mass spectrum fits with GPR background estimation for $x_F = 0.05 - 0.11$ bin for the north (top) and south (bottom) arm with $p + \text{Au}$ data

BinningMode_2_Arm0_Charge0_bin0.1_0.3



BinningMode_2_Arm1_Charge0_bin0.1_0.3

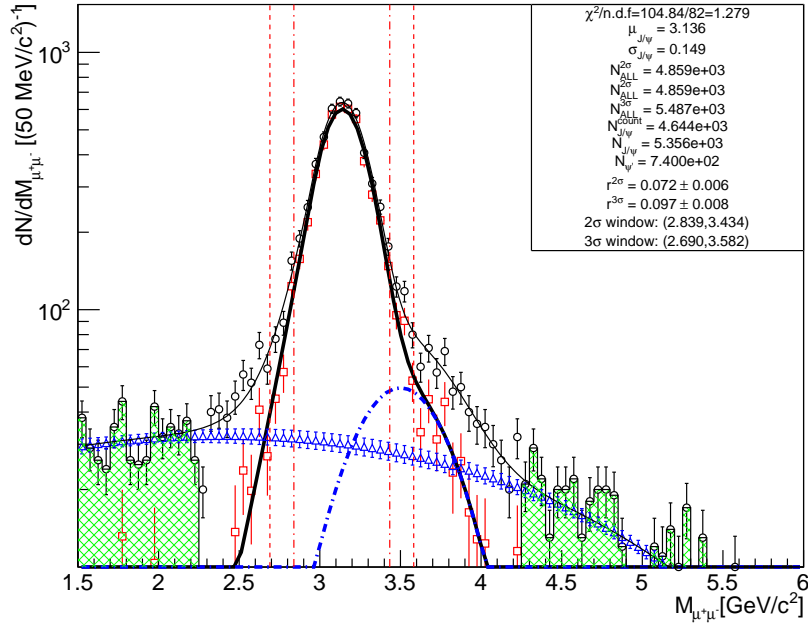
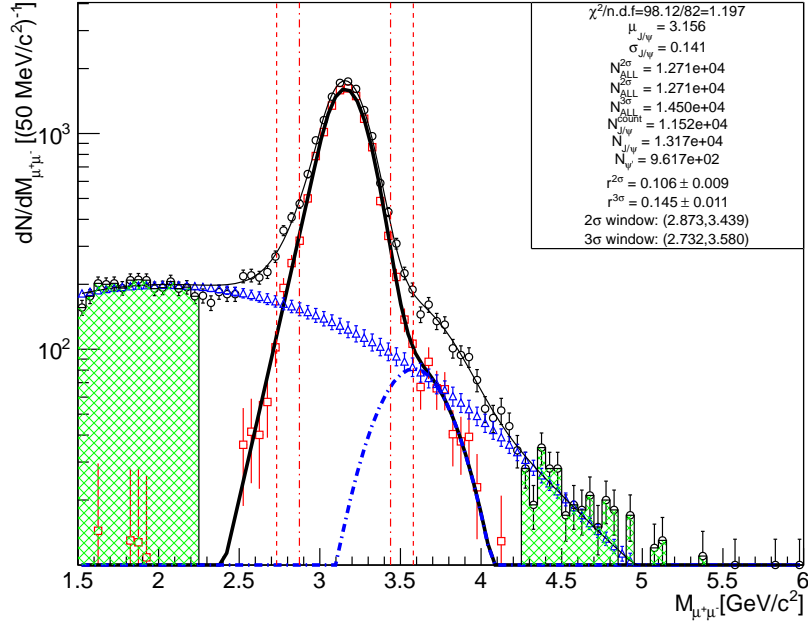


Figure 44: MuTr mass spectrum fits with GPR background estimation for $x_F = 0.11 - 0.30$ bin for the north (top) and south (bottom) arm with $p + \text{Au}$ data

BinningMode_1_Arm0_Charge0_bin0.0_10.0



BinningMode_1_Arm1_Charge0_bin0.0_10.0

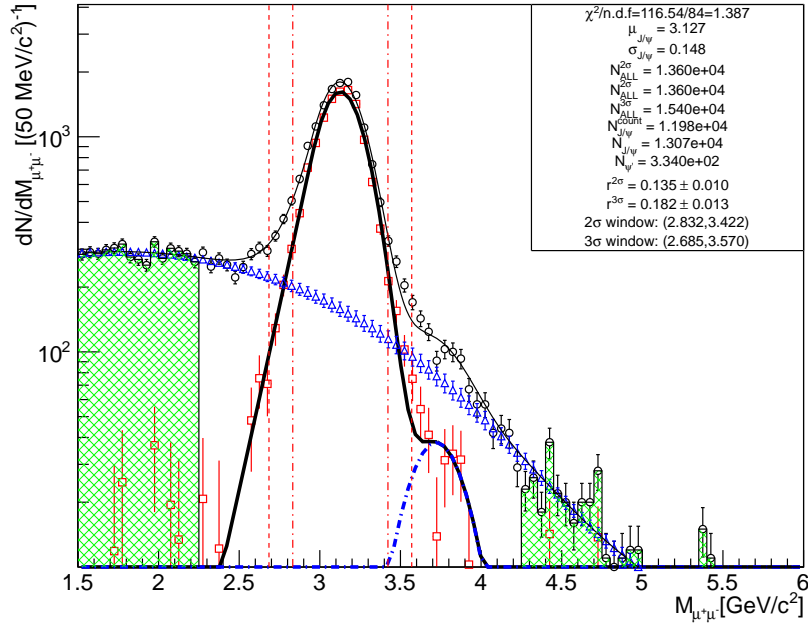
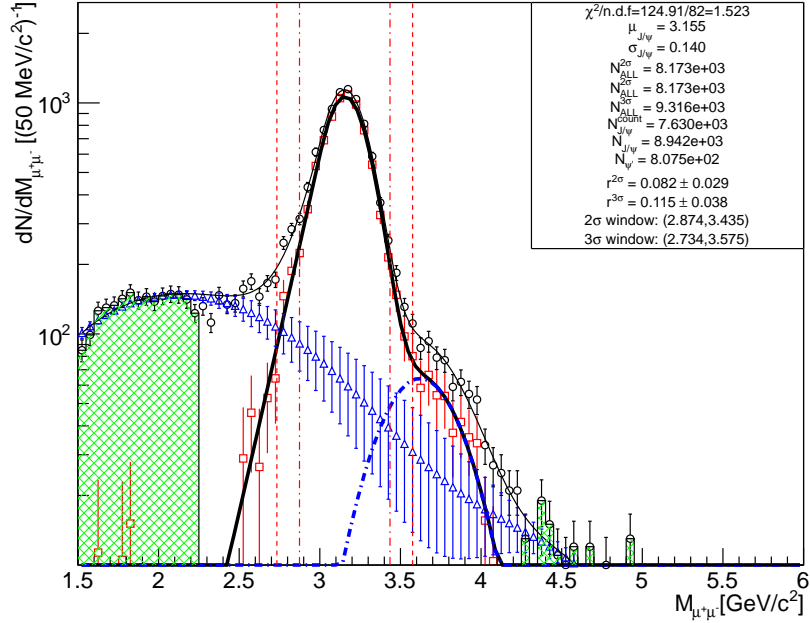


Figure 45: MuTr mass spectrum fits with GPR background estimation for $p_T = 0 - 10 \text{ GeV}$ bin for the north (top) and south (bottom) arm with $p + \text{Al}$ data

BinningMode_1_Arm0_Charge0_bin0.0_2.0



BinningMode_1_Arm1_Charge0_bin0.0_2.0

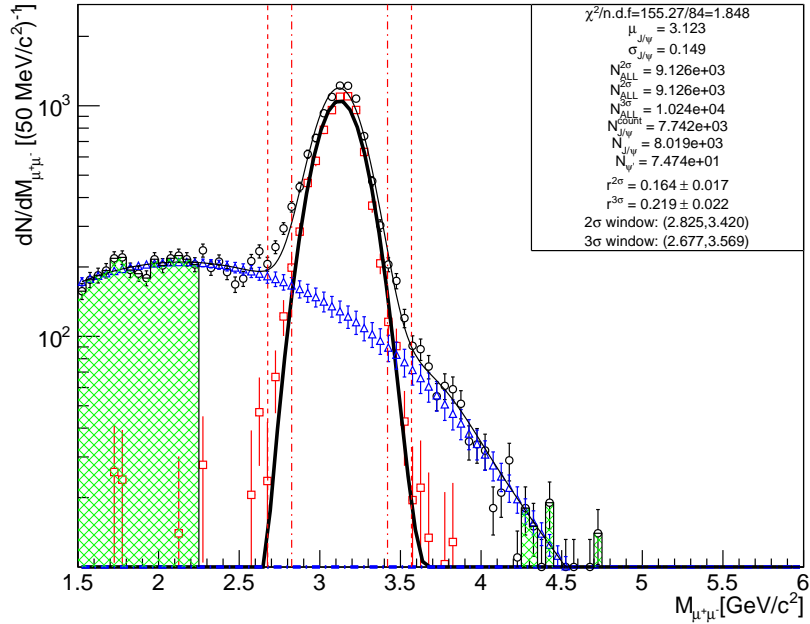
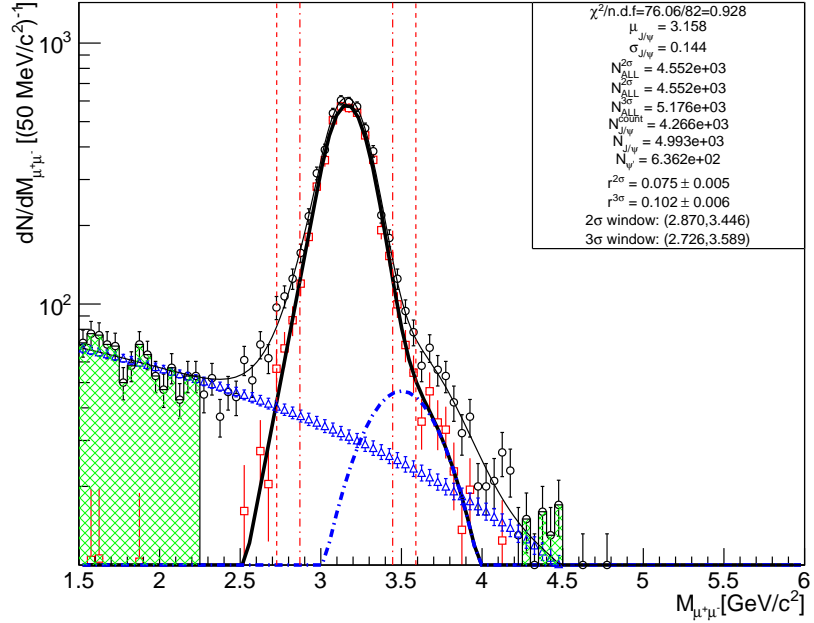


Figure 46: MuTr mass spectrum fits with GPR background estimation for $p_T = 0 - 2 \text{ GeV}$ bin for the north (top) and south (bottom) arm with $p + \text{Al}$ data

BinningMode_1_Arm0_Charge0_bin2.0_10.0



BinningMode_1_Arm1_Charge0_bin2.0_10.0

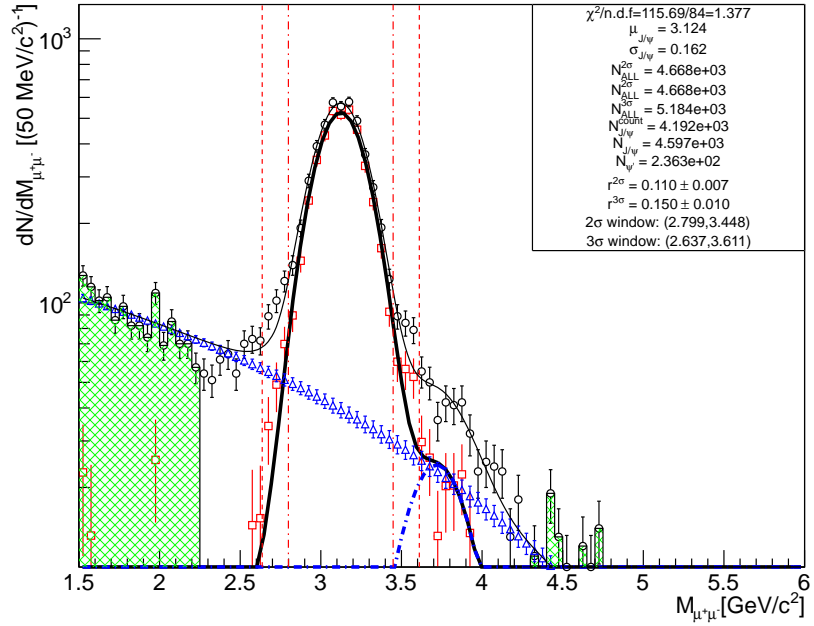
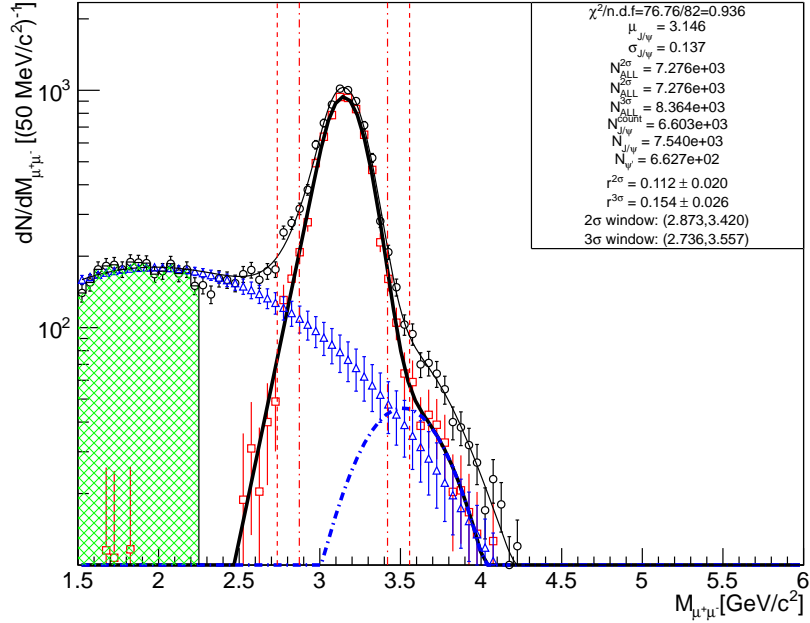


Figure 47: MuTr mass spectrum fits with GPR background estimation for $p_T = 2 - 10 \text{ GeV}$ bin for the north (top) and south (bottom) arm with $p + \text{Al}$ data

BinningMode_2_Arm0_Charge0_bin0.1_0.1



BinningMode_2_Arm1_Charge0_bin0.1_0.1

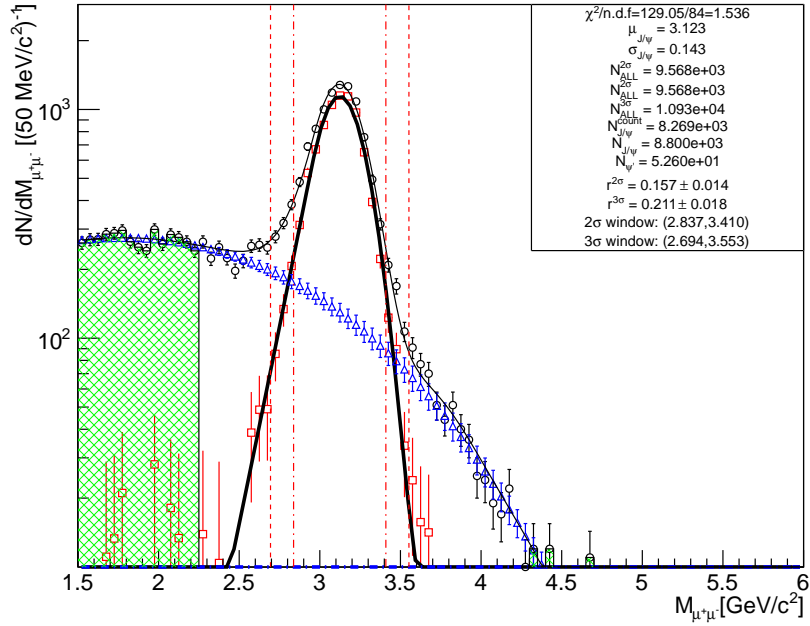
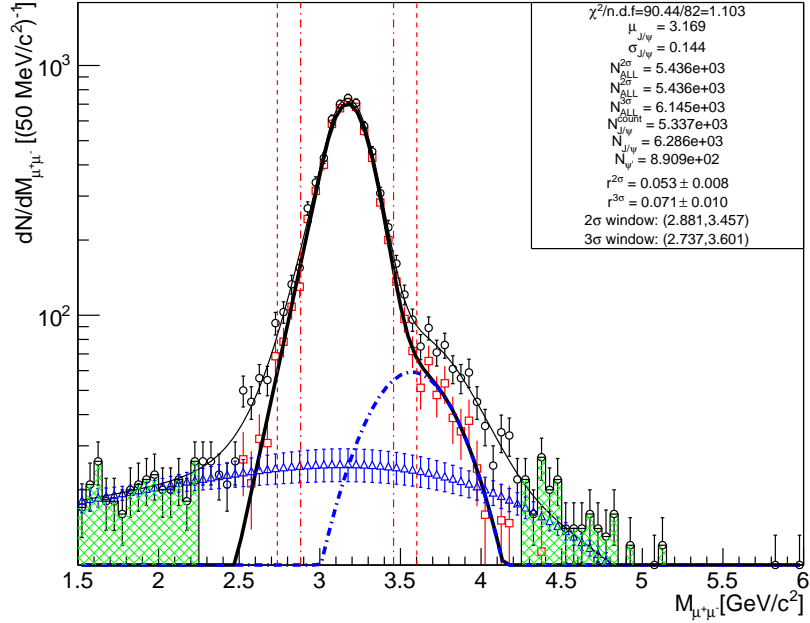


Figure 48: MuTr mass spectrum fits with GPR background estimation for $x_F = 0.05 - 0.11$ bin for the north (top) and south (bottom) arm with $p + \text{Al}$ data

BinningMode_2_Arm0_Charge0_bin0.1_0.3



BinningMode_2_Arm1_Charge0_bin0.1_0.3

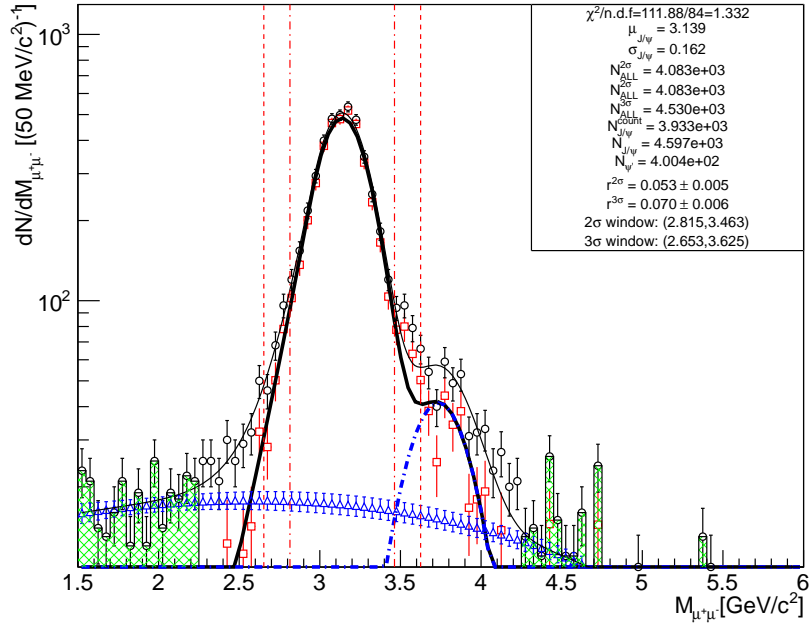


Figure 49: MuTr mass spectrum fits with GPR background estimation for $x_F = 0.11 - 0.30$ GeV bin for the north (top) and south (bottom) arm with $p + \text{Al}$ data

Table 3 shows the background fraction in p_T bins from GPR for $p + p$ data.

Table 4 shows the background fraction in p_T bins from GPR for $p + \text{Au}$ data.

Table 5 shows the background fraction in p_T bins from GPR for $p + \text{Al}$ data.

Table 6 shows the background fraction in x_F bins from GPR for $p + p$ data.

Table 7 shows the background fraction in x_F bins from GPR for $p + \text{Au}$ data.

Table 8 shows the background fraction in x_F bins from GPR for $p + \text{Al}$ data.

These tables show that the background fraction in p -going direction in all bins are less than 10% and, in Al-going and Au-going direction, the background fraction is higher than in the p -going direction.

p_T (GeV)	$f_{Bgr} \pm \delta f_{Bgr}(\text{Stat.})(\%)$ North	$f_{Bgr} \pm \delta f_{Bgr}(\text{Stat.})(\%)$ South
$p_T \in 0 - 2$	9.9 ± 1.0	10.3 ± 1.1
$p_T \in 2 - 10$	6.8 ± 0.7	5.3 ± 0.6

Table 3: Background Fraction in p_T bins for $p + p$ data

p_T (GeV)	$f_{Bgr} \pm \delta f_{Bgr}(\text{Stat.})(\%)$ North	$f_{Bgr} \pm \delta f_{Bgr}(\text{Stat.})(\%)$ South
$p_T \in 0 - 2$	9.7 ± 1.6	19.4 ± 2.2
$p_T \in 2 - 10$	7.5 ± 0.5	9.1 ± 1.1

Table 4: Background Fraction in p_T bins for $p + \text{Au}$ data

p_T (GeV)	$f_{Bgr} \pm \delta f_{Bgr}(Stat.)(\%)$ North	$f_{Bgr} \pm \delta f_{Bgr}(Stat.)(\%)$ South
$p_T \in 0 - 2$	8.2 ± 1.6	16.3 ± 1.5
$p_T \in 2 - 10$	7.5 ± 0.6	11.0 ± 0.7

Table 5: Background Fraction in p_T bins for $p + \text{Al}$ data

x_F	$f_{Bgr} \pm \delta f_{Bgr}(Stat.)(\%)$ North	$f_{Bgr} \pm \delta f_{Bgr}(Stat.)(\%)$ South
$x_F \in 0.05 - 0.11$	10.5 ± 1.0	10.3 ± 0.9
$x_F \in 0.11 - 0.30$	4.4 ± 0.3	3.5 ± 0.2

Table 6: Background Fraction in x_F bins for $p + p$ data

x_F	$f_{Bgr} \pm \delta f_{Bgr}(Stat.)(\%)$ North	$f_{Bgr} \pm \delta f_{Bgr}(Stat.)(\%)$ South
$x_F \in 0.05 - 0.11$	13.3 ± 1.6	18.9 ± 1.6
$x_F \in 0.11 - 0.30$	3.6 ± 0.2	7.2 ± 0.6

Table 7: Background Fraction in x_F bins for $p + \text{Au}$ data

x_F	$f_{Bgr} \pm \delta f_{Bgr}(Stat.)(\%)$ North	$f_{Bgr} \pm \delta f_{Bgr}(Stat.)(\%)$ South
$x_F \in 0.05 - 0.11$	11.2 ± 2.5	15.7 ± 1.6
$x_F \in 0.11 - 0.30$	5.3 ± 0.6	5.3 ± 0.5

Table 8: Background Fraction in x_F bins for $p + \text{Al}$ data

3.5 Inclusive and Background A_N extraction

3.5.1 Maximum Likelihood method

The Maximum Likelihood Method has been used in the previous $J/\psi A_N$ analyses in PHENIX and it has the advantage of dealing with low statistic situations very nicely. The main idea of the Maximum Likelihood Method is representing the outcome of given data as a probability function of one set of parameters. Then the parameters can be gotten by achieving the maximum likelihood of the probability, $p(\theta|data)$, where θ represents the parameters. In general, a maximum likelihood problem can be written in the following form:

$$\max_{\theta} p(\theta|data) \quad (43)$$

Namely, return the parameter set θ that gives the maximum $p(\theta|data)$. In the context of transversely single spin asymmetry, the likelihood \mathcal{L} for one dimuon pair with azimuthal angle ϕ with respect to the incoming proton beam polarization direction is $\sigma_0(1 + P \cdot A_N \sin(\phi_{\text{pol}} - \phi))$ which is corresponding to Sivers effect to the asymmetry [43], where σ_0 is the unpolarized cross section, P is the beam polarization, and ϕ_{pol} is the direction of beam polarization which is $+(-)\pi/2$ when the spin is up (down). Then the log-likelihood for all the dimuon pairs is given by:

$$\log \mathcal{L} = \sum_i \log(1 + P \cdot A_N \sin(\phi_{\text{pol}} - \phi_i)). \quad (44)$$

where P is the beam polarization which is the average polarization of each run weighted by run luminosity and ϕ_i is the azimuthal angle of i th outgoing J/ψ from the data set. Table 9 shows the polarization of polarized proton beams in each data set.

In most optimization cases, one of the concerns is whether our problem has only one maximum or minimum point. After all, the global maximum/minimum is what we really pursue. In many practical cases, a global optimization is assumed. The standard methods to find the optimum parameters, such as gradient descent method and Newton's method, are quite efficient in finding one or multiple parameters that are present in the likelihood function. Notice that both gradient descent method and Newton's method assume a global optimization. In our case, there is only one parameter in the likelihood function and the maximum range of A_N can not exceed $[-1,1]$. So in this problem, we can simply scan the A_N from -1 to 1 with 1200 steps to find the best estimator A_N . The gradient descent method and Newton's method are more widely used and have better performance than the scanning method because they are more computationally friendly especially in problems with large sets of parameters. The main reason, in our case, to pick scanning method is the scanning procedures can be visualized. In that case, instead of blindly running a code and get a result, we can check what is the behavior of the likelihood function vs. the target parameter. So the global optimization can be guaranteed by this data visualization. Figure 58 shows how

Table 9: Blue and yellow beam polarization in $p + p$ and $p + A$ collisions.

Data set	Blue beam	Yellow beam
$p + p$	57%	57%
$p + \text{Al}$	57%	0
$p + \text{Au}$	61%	0

the global optimization is checked. The statistical uncertainty of A_N is obtained by calculating the inverse of the second derivative of \mathcal{L} with respect to A_N :

$$\sigma^2(A_N) = \left(-\frac{\partial^2 \log \mathcal{L}}{\partial^2 A_N} \right)^{-1}. \quad (45)$$

3.5.2 Azimuthal Fitting method with Spin Analyzer

The Azimuthal Fitting method is developed basing on the definition of Transverse Single Spin Asymmetry. Similar to Eq. 44, the production cross section of J/ψ as a function of the azimuthal angle ϕ is given by:

$$\sigma(\phi) \propto 1 + P \cdot A_N \sin(\phi_{\text{pol}} - \phi), \quad (46)$$

where $\phi_{\text{pol}} = +(-)\pi/2$ when the spin is up (down).

The asymmetry can be written as function of azimuthal angle ϕ as:

$$A(\phi) = \frac{\sigma^\uparrow(\phi) - \sigma^\downarrow(\phi)}{\sigma^\uparrow(\phi) + \sigma^\downarrow(\phi)} = A_N \cdot \cos(\phi). \quad (47)$$

Therefore, A_N can be extracted by fitting the $A(\phi)$ with a cosine modulation. A feature of the Azimuthal Fitting method that is better over Maximum Likelihood

method is that one can check the quality of the fitting by using the χ^2/NDF . While the quality of Maximum Likelihood fitting can not be quantified as we shall see in the following sections. The most important feature of Maximum Likelihood method is that it is not sensitive to low statistic cases which makes it as the main method of this analysis.

The Azimuthal Fitting method is implemented with the framework of Spin Analyzer (or SpinAnalyzer) which is a new tool to formalize the common parts of the spin-asymmetry analysis under the PHENIX Fun4All framework. SpinAnalyzer lets users input good events as if filling a histogram of counts and the SpinAnalyzer classifies the counts with respect to the spin pattern. Having also taken the relative luminosity into account, SpinAnalyzer will calculate the asymmetry automatically in the background. The most relative features of SpinAnalyzer to this analysis are:

1. The spin information is directly loaded from the Spin Database. The newest database QA level is used at the time when SpinAnalyzer is run.
2. The output from SpinAnalyzer is histograms of counts which are categorized with respect to spin combinations. If chosen, it will also output histograms containing the single and double spin-asymmetry results.
3. Spin Analyzer, previously focusing on double spin asymmetry, now is capable to do single polarized beam case such as $p + \text{Au}$ collisions.

One more thing needed to be mentioned here is the spin value read from Spin Database. The values in the spin DB are taken from the Control Device API(CDEV) packets, which is provided by Collider-Accelerator Department.CDEV data has spin information at 12 o'clock, where the RHIC polarimeters are located. Therefore, +1 (-1) in the spin DB means spin-down (spin-up) at 12 o'clock.

The spin direction is reversed at PHENIX after the proton beam passed the Siberian snakes (helical magnets) between 12 o'clock and PHENIX (there are two places where the Siberian snakes are in RHIC, so the spin direction is back to original after each rotation). Therefore, +1 (-1) in the spin DB means spin-down (spin-up) at PHENIX.

3.5.3 Maximum Likelihood method with $p + p$ data

In $p + p$ collisions, both the blue beam and yellow beam are polarized. In Run15, the transverse polarization direction is along Y -axis as it has been shown in figure 50. So when $A_N(\phi)$ is calculated w.r.t blue beam, the azimuthal angle is already under the PHENIX coordinate system. However, this is not the case for yellow beam since yellow beam is traveling towards South Arm which is along the negative Z direction in the PHENIX coordinate system. The azimuthal angle under the PHENIX coordinate system is $\pi - \phi$ w.r.t yellow beam. Therefore,

instead of directly applying Eq. 44 to each track, a modified equation is applied:

$$\log \mathcal{L} = \sum_i \log(1 - P \cdot A_N \sin(\phi_{\text{pol}} - \phi_i)). \quad (48)$$

The only difference between Eq. 44 and 48 is the sign before P .

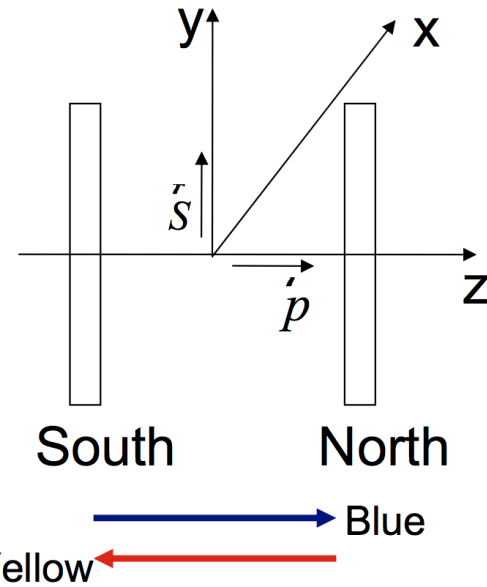


Figure 50: Beam polarization setup for polarized protons in Run15.

Table 10 and table 11 list the inclusive (background) A_N with all the bins for Blue and Yellow beam.

3.5.4 Azimuthal Fitting method with $p + p$ collisions

To achieve sufficient statistics from data in $p + p$ collisions, 16 equal-sized ϕ bins in each p_T and x_F range were assigned. The azimuthal angle ϕ is calculated under

Arm (Blue Beam)	$A_N^{Inc.} \pm \delta A_N^{Inc.}(Stat.)$	$A_N^{Bgr.} \pm \delta A_N^{Bgr.}(Stat.)$
North($0 < p_T < 2\text{GeV}$)	0.007 ± 0.015	0.032 ± 0.035
North($2 < p_T < 10\text{GeV}$)	0.016 ± 0.021	0.111 ± 0.058
North($0.05 < x_F < 0.11$)	0.005 ± 0.015	0.035 ± 0.032
North($0.11 < x_F < 0.30$)	0.016 ± 0.019	0.178 ± 0.087
South($0 < p_T < 2\text{Gev}$)	0.004 ± 0.013	0.023 ± 0.028
South($2 < p_T < 10\text{Gev}$)	0.011 ± 0.020	0.005 ± 0.056
South($0.05 < x_F < 0.11$)	0.004 ± 0.013	0.025 ± 0.026
South($0.11 < x_F < 0.30$)	0.015 ± 0.020	-0.023 ± 0.096

Table 10: List of Inclusive and background A_N from Maximum Likelihood for Blue beam with $p + p$ data

Arm (Yellow Beam)	$A_N^{Inc.} \pm \delta A_N^{Inc.}(Stat.)$	$A_N^{Bgr.} \pm \delta A_N^{Bgr.}(Stat.)$
North($0 < p_T < 2\text{GeV}$)	0.021 ± 0.015	0.018 ± 0.035
North($2 < p_T < 10\text{GeV}$)	0.053 ± 0.021	0.072 ± 0.058
North($0.05 < x_F < 0.11$)	0.026 ± 0.015	0.021 ± 0.032
North($0.11 < x_F < 0.30$)	0.040 ± 0.019	0.117 ± 0.087
South($0 < p_T < 2\text{Gev}$)	0.005 ± 0.013	0.032 ± 0.030
South($2 < p_T < 10\text{Gev}$)	0.004 ± 0.020	0.060 ± 0.056
South($0.05 < x_F < 0.11$)	0.009 ± 0.013	0.029 ± 0.028
South($0.11 < x_F < 0.30$)	-0.005 ± 0.020	0.137 ± 0.096

Table 11: List of Inclusive and background A_N from Maximum Likelihood for Yellow beam with $p + p$ data

the PHENIX coordinate system. The same ϕ binning is made also for $p + \text{Al}$ and $p + \text{Au}$ collisions.

The inclusive and background asymmetries extracted from the Spin Analyzer are shown in figures 53 to 55. The inclusive asymmetry is calculated from like-sign dimuon pairs within 2σ invariant mass range, centered on the J/ψ peak, obtained from the GPR fitting in section 3.4. The background asymmetry is calculated from the low-side-band dimuon invariant mass range from 1.5 to 2.4 GeV. The χ^2/NDF for each bin, as we shall see from the panels, is always around 1 which is what we expected. The result gotten from the Azimuthal Fitting method is consistent with the result from the Maximum Likelihood method: the central values are within 0.1 standard deviations of each other and the statistical uncertainty for each bin are equal. The differences in $J/\psi A_N$ from these two methods will be considered as a systematic uncertainty which will be discussed in the later chapters.

3.5.5 Maximum Likelihood method with $p + \text{Au}$ data

In $p + \text{Au}$, the polarized proton is traveling towards positive z -direction so the azimuthal angle is given by the PHENIX coordinate system. But before we can really start calculating the azimuthal angle, we need to address the “tilt angle” issue in $p + \text{Au}$ collisions as it has been shown in figure 57 which plots the $FVTX_X vs. FVTX_Z$ distribution in $p + \text{Au}$ collisions. By comparing figure 57 with figure 56 where two proton are moving exactly along the z -axis, we can eas-

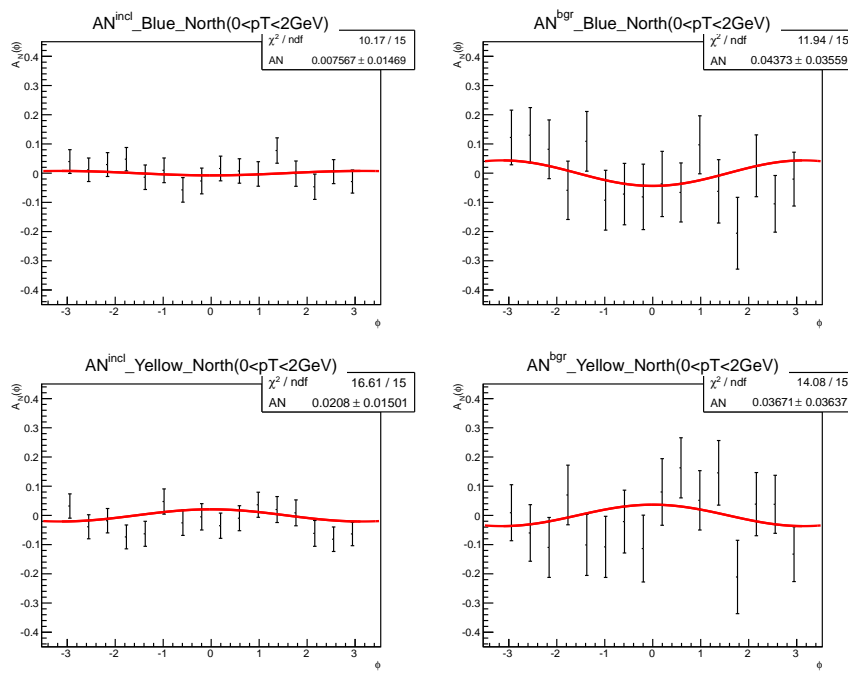


Figure 51: $p + p$ Inclusive and background A_N with $0 < p_T < 2$ GeV bin in North arm

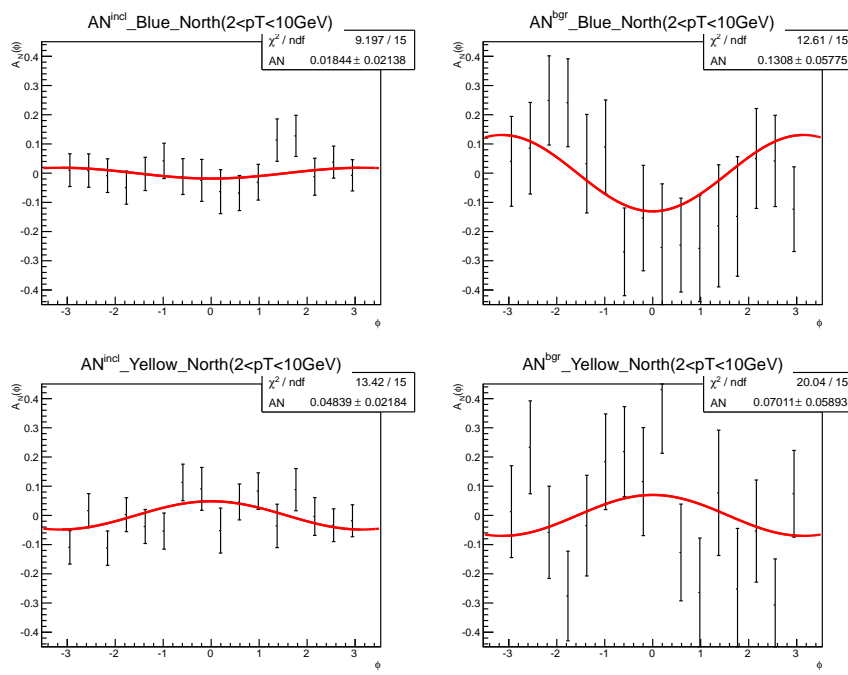


Figure 52: $p + p$ Inclusive(left) and background(right) A_N with $2 < p_T < 10$ GeV bin in North arm

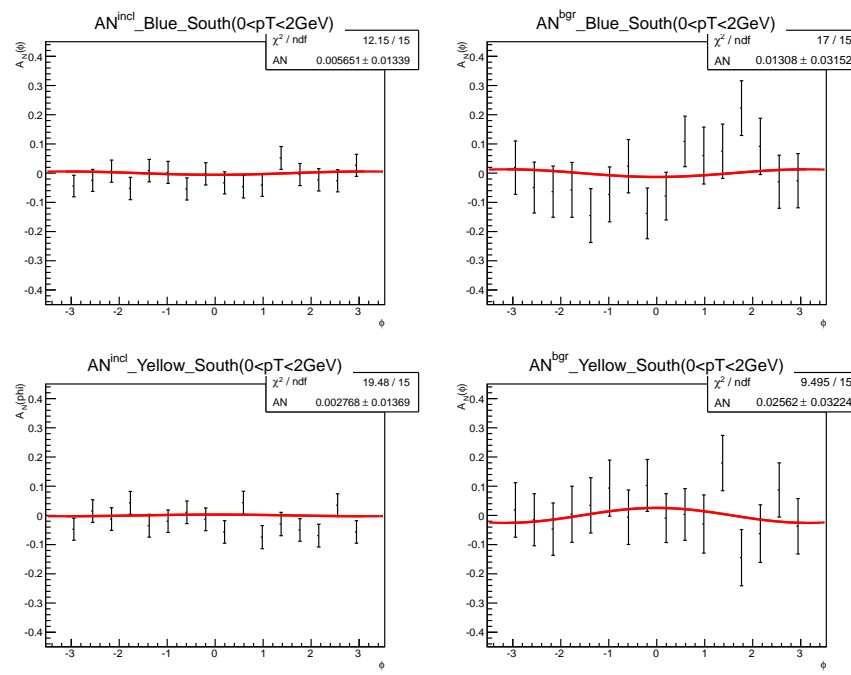


Figure 53: $p + p$ Inclusive(left) and background(right) A_N with $0 < p_T < 2$ GeV bin in South arm

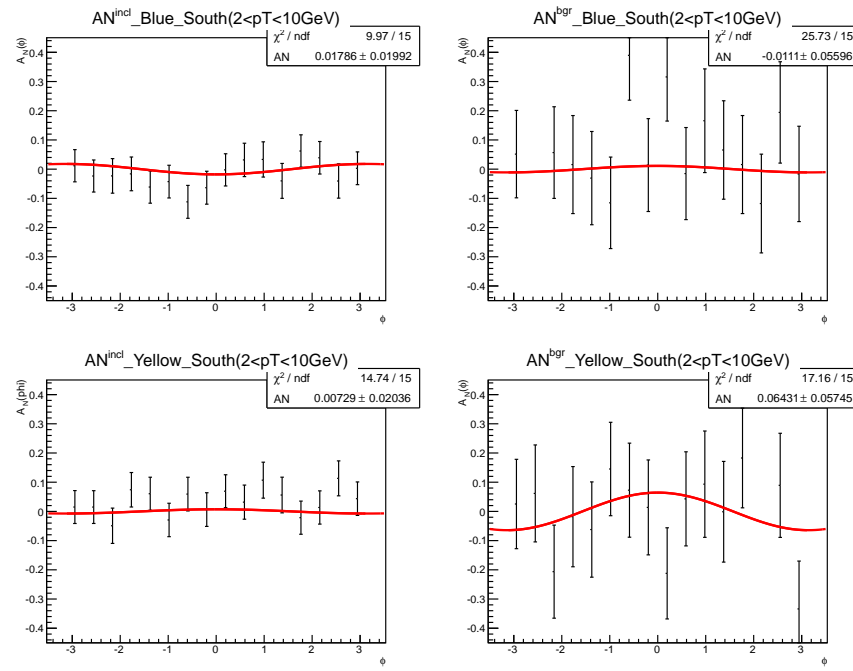


Figure 54: $p + p$ Inclusive(left) and background(right) A_N with $2 < p_T < 10$ GeV bin in South arm

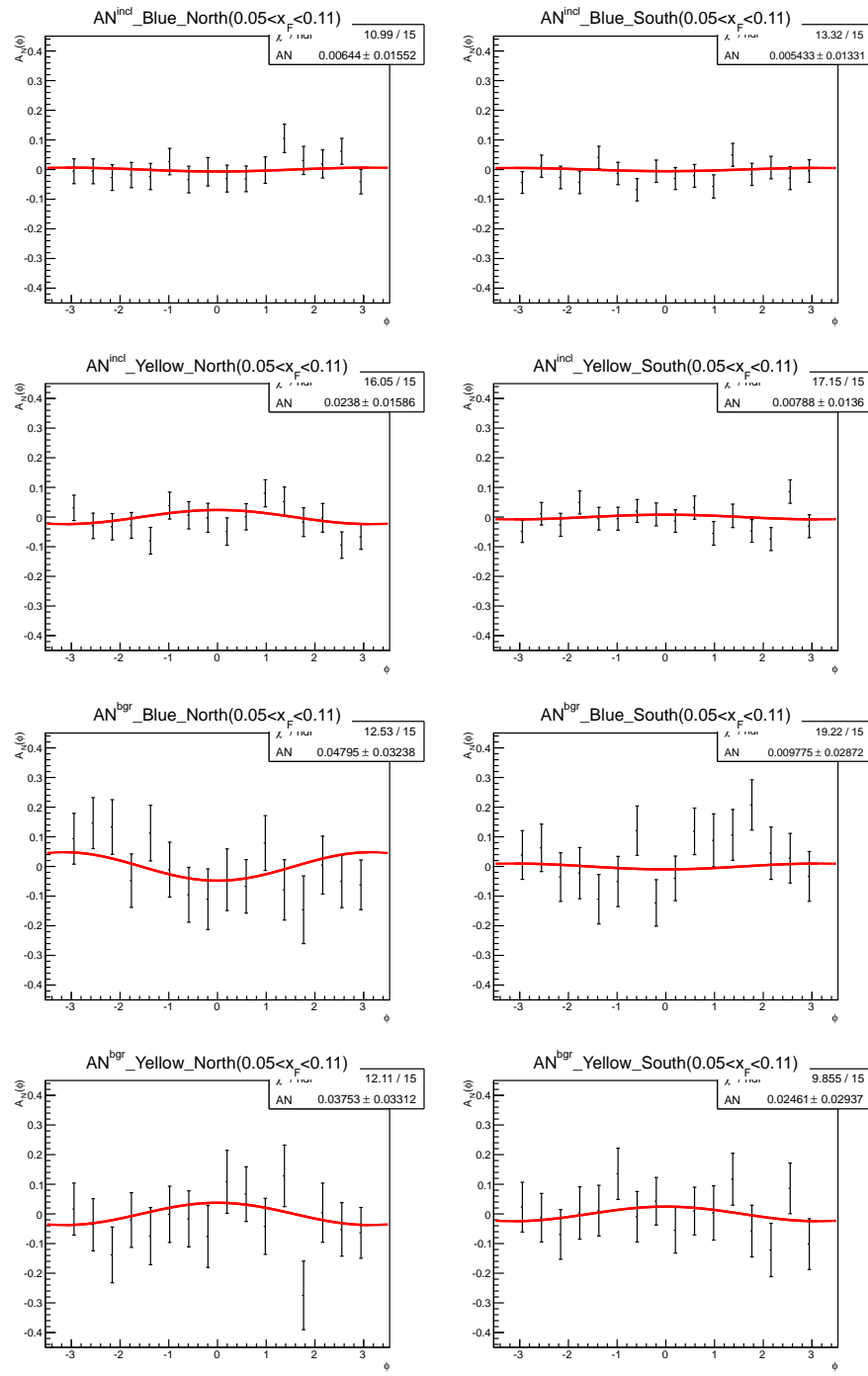


Figure 55: pp Inclusive(top plot)&background(bottom plot) A_N with one x_F bin

ily identify that, in $p + \text{Au}$ collisions, the Blue and Yellow beams are not moving exactly along z -axis, though it is still a head-on collision. The tilt angle can be calculated by the slope of the highlighted band in figure 57 and the value is 3.6 mrad.

This tilt angle means the z -axis of the Center of Mass (CM) frame of the collision is no longer aligned with the z -axis of the PHENIX coordinate system. Since every measured quantity is recorded in the PHENIX coordinate system, we need to transform the momentum vectors into the CM frame. Considering that it is still a head-on collision, only a rotation transformation is needed for this purpose. The transformation is shown as following:

$$p'_y = p_y \quad (49)$$

$$p'_x = \cos(\alpha) * p_x - \sin(\alpha) * p_z \quad (50)$$

$$p'_z = \sin(\alpha) * p_x + \cos(\alpha) * p_z \quad (51)$$

where $p_{x,y,z}$ is the momentum recorded in pDST and $p'_{x,y,z}$ is the momentum in CM frame and α is 3.6 mrad as mentioned above.

Having got the corrected momentum, one can calculate the azimuthal angle in the CM frame. Then apply the Maximum Likelihood method to extract inclusive and background A_N for each bin. Figure 58 shows inclusive and background asymmetry scanning with Maximum Likelihood method for $p + \text{Au}$ data. From

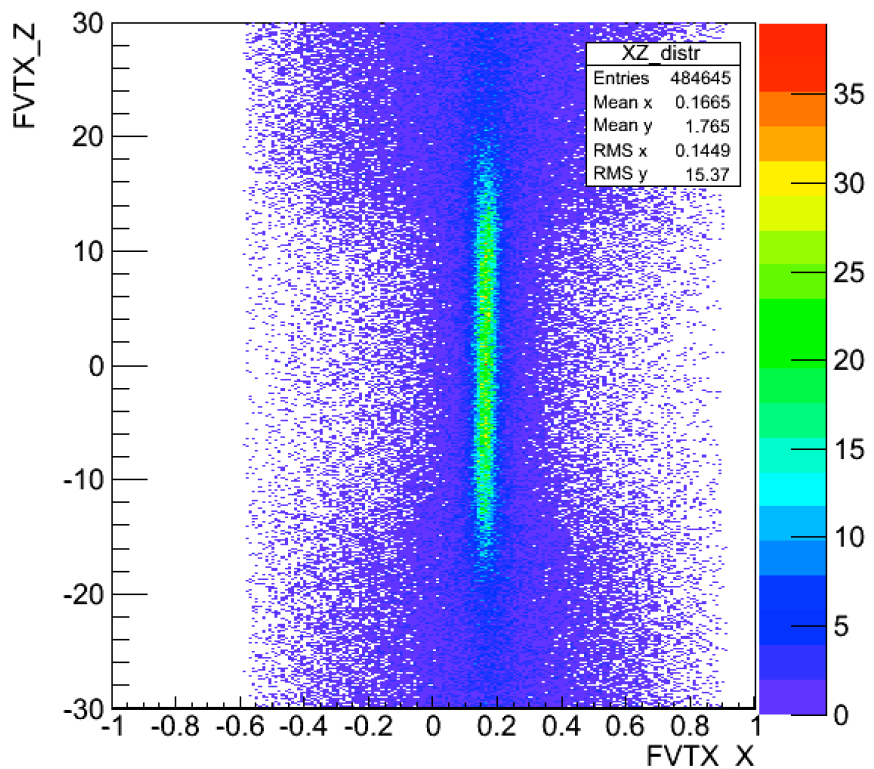


Figure 56: This plot shows FVTX_X vs. FVTX_Z distribution in $p + p$ collisions.

The intense green band is perpendicular to the x -axis which indicates that $p + p$ collisions in Run15 were along the z -axis.

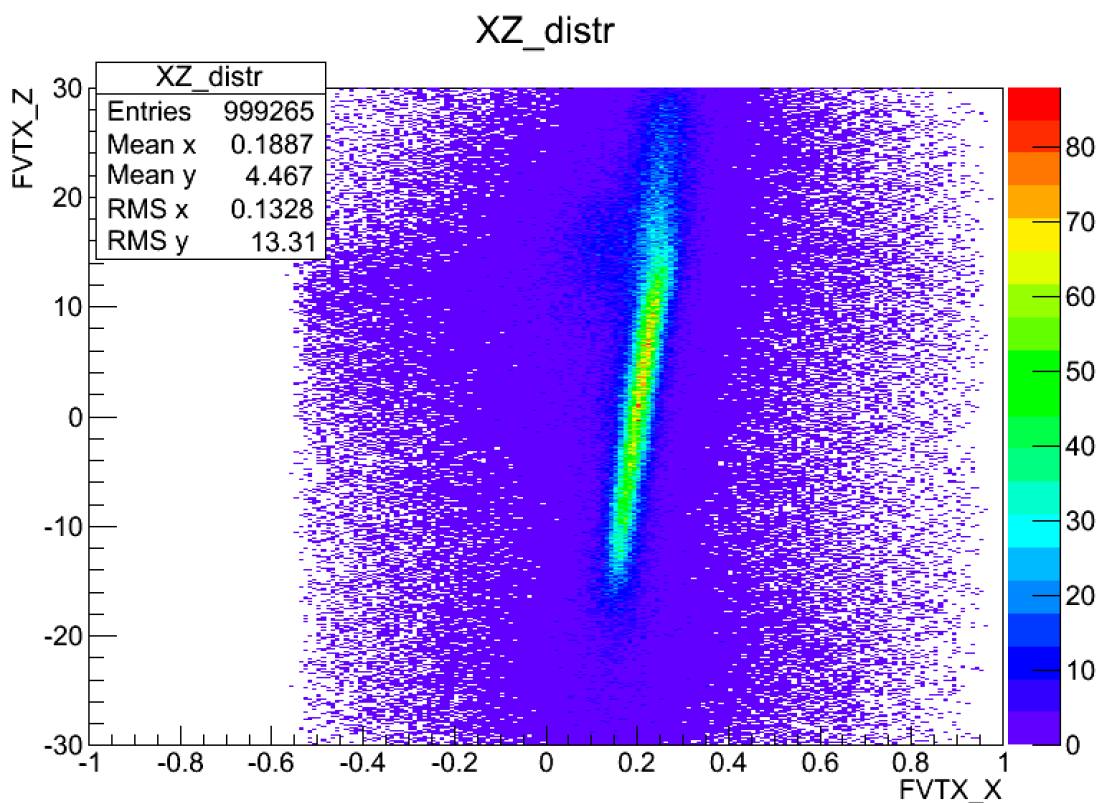


Figure 57: This plot shows FVTX_X vs. FVTX_Z distribution in $p + \text{Au}$ collision.

The intense green band indicates that $p + \text{Au}$ collisions were not exactly along the z -axis.

this panel, we can see that the scanning curves have a single global minimum point which is corresponding to the asymmetry and they are very smooth with the current stepping setting. Tables 12 and 13 list the inclusive and background A_N that we found from the scanning.

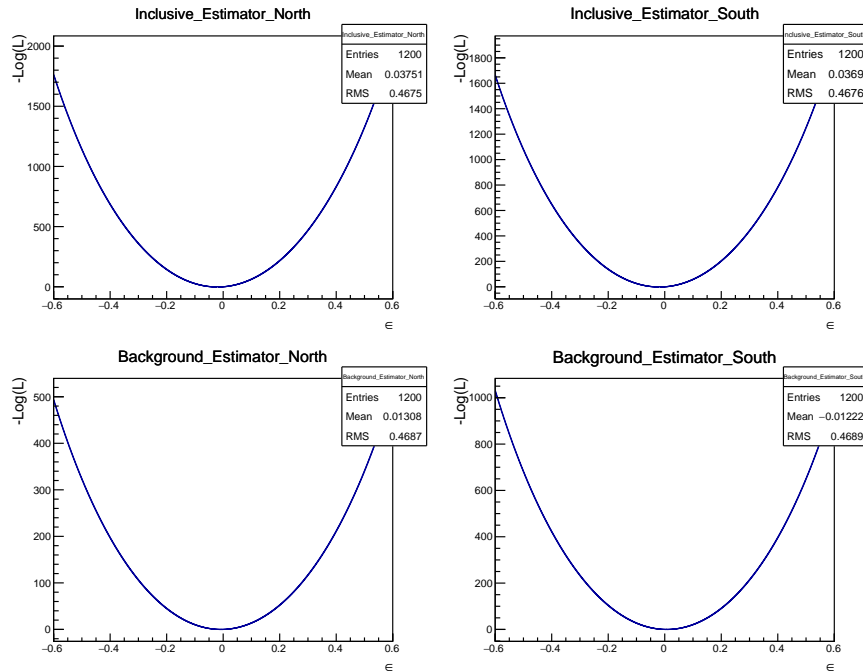


Figure 58: Epsilon scanning with $p+\text{Au}$ dataset. Top (bottom) left: epsilon scanning for inclusive (background) A_N in North arm with $0.05 < x_F < 0.11$. Top (bottom) right: epsilon scanning for inclusive (background) A_N in South arm with $0.05 < x_F < 0.11$.

p_T	$A_N^{Inc.} \pm \delta A_N^{Inc.}(Stat.)$ North	$A_N^{Inc.} \pm \delta A_N^{Inc.}(Stat.)$ South
$p_T(GeV) \in 0 - 2$	-0.061 \pm 0.022	-0.056 \pm 0.023
$p_T \in 2 - 10$	0.010 \pm 0.028	0.010 \pm 0.028
$x_F \in 0.05 - 0.11$	-0.025 \pm 0.023	-0.045 \pm 0.021
$x_F \in 0.11 - 0.30$	-0.045 \pm 0.027	-0.021 \pm 0.033

Table 12: $A_N^{Inc.}$ in different p_T and x_F bins with pAu data

p_T	$A_N^{Bgr.} \pm \delta A_N^{Bgr.}(Stat.)$ North	$A_N^{Bgr.} \pm \delta A_N^{Bgr.}(Stat.)$ South
$p_T \in 0 - 2$	-0.005 \pm 0.043	0.020 \pm 0.028
$p_T \in 2 - 10$	-0.026 \pm 0.055	-0.017 \pm 0.046
$x_F \in 0.05 - 0.11$	-0.010 \pm 0.036	0.015 \pm 0.025
$x_F \in 0.11 - 0.30$	-0.036 \pm 0.093	-0.051 \pm 0.097

Table 13: $A_N^{Bgr.}$ in different p_T and x_F bins with pAu data

3.5.6 Azimuthal Fitting method with $p + \text{Au}$ collisions

Similar with the procedure in $p + p$ case, inclusive and background asymmetries with $p + \text{Au}$ data extracted from Spin Analyzer are shown in figures 59 to 62. The inclusive asymmetry is calculated from like-sign dimuon pairs within $2-\sigma$ invariant mass range gotten from GPR fitting in section 3.4. The background asymmetry is calculated from the low-side-band dimuon invariant mass range from 1.5 to 2.4 GeV.

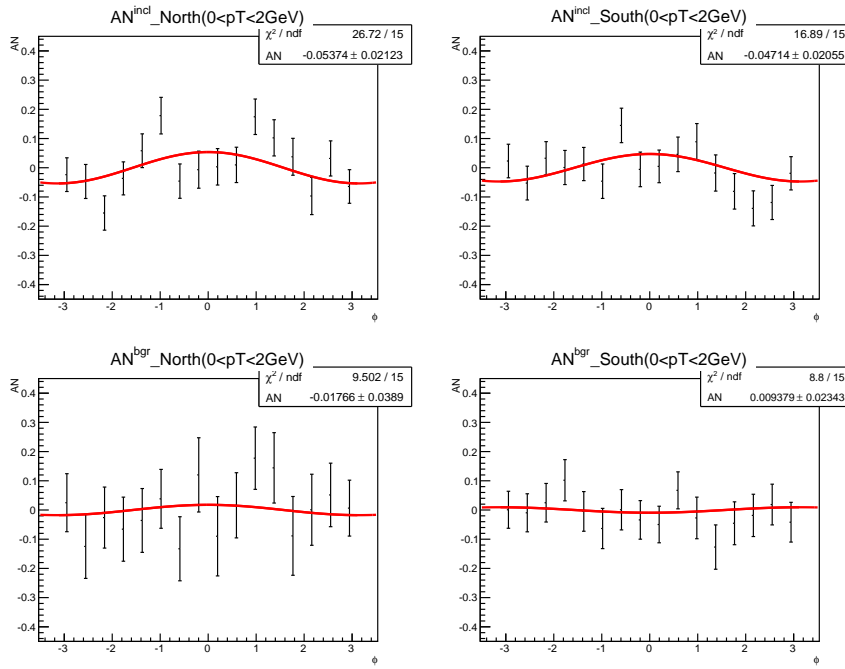


Figure 59: $p + \text{Au}$ Inclusive(left) and background(right) A_N with $0 < p_T < 2\text{GeV}$

In order to investigate how the tilt angle would affect the result, a comparison of inclusive and background A_N obtained before and after tilt angle correction

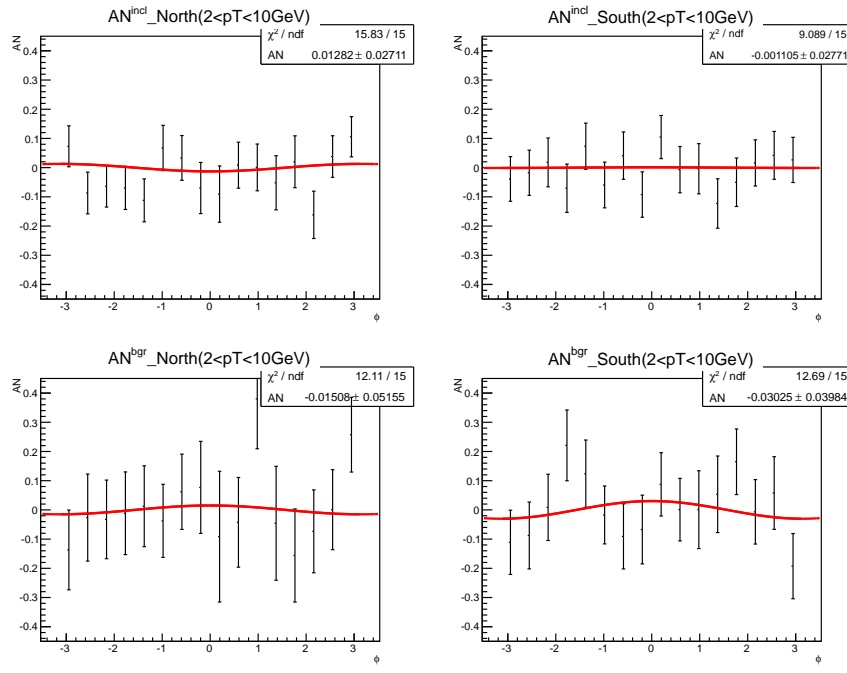


Figure 60: $p + \text{Au}$ Inclusive(left) and background(right) A_N with $2 < p_T < 10 \text{ GeV}$

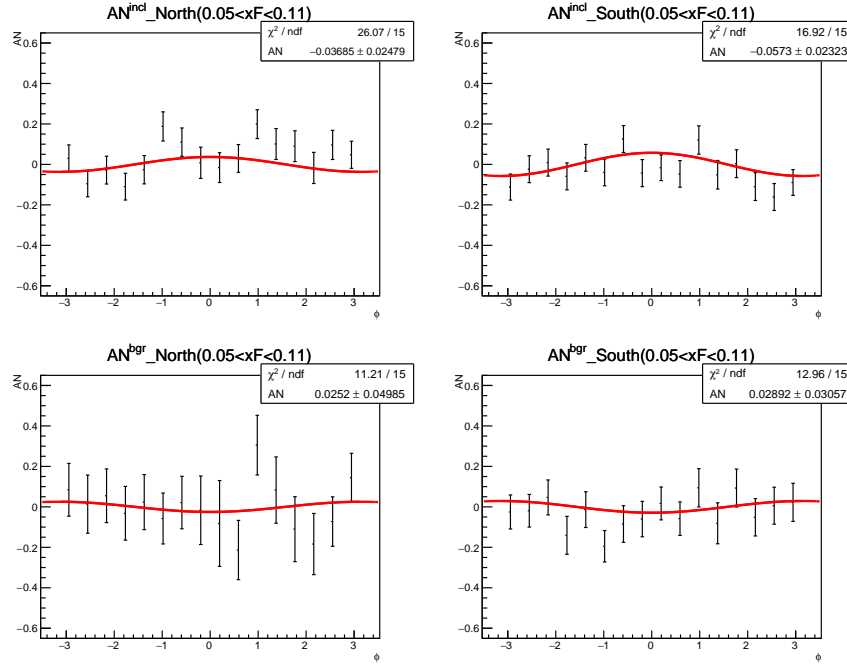


Figure 61: $p + \text{Au}$ Inclusive(left) and background(right) A_N with $0.05 < x_F < 0.11$

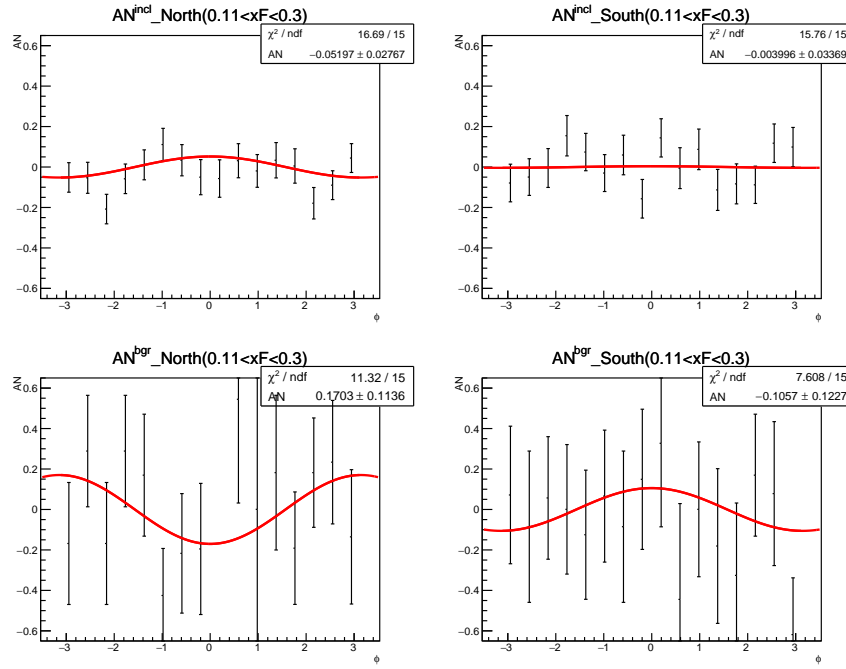


Figure 62: $p + \text{Au}$ Inclusive(left) and background(right) A_N with $0.11 < x_F < 0.30$

was made. Figure 63 shows the inclusive and background A_N in combined x_F bin before tilt angle correction. The difference due to the tilt angle correction is about 0.1 sigma. Therefore, the tilt angle correction will not affect our results in a significant way.

3.5.7 Maximum Likelihood method with $p + \text{Al}$ data

Similar with what has been seen in $p + \text{Au}$ data, there is a tilt angle in $p + \text{Al}$ collisions of 2.5 mrad. The result shown in this section is the inclusive and background A_N after the tilt angle correction.

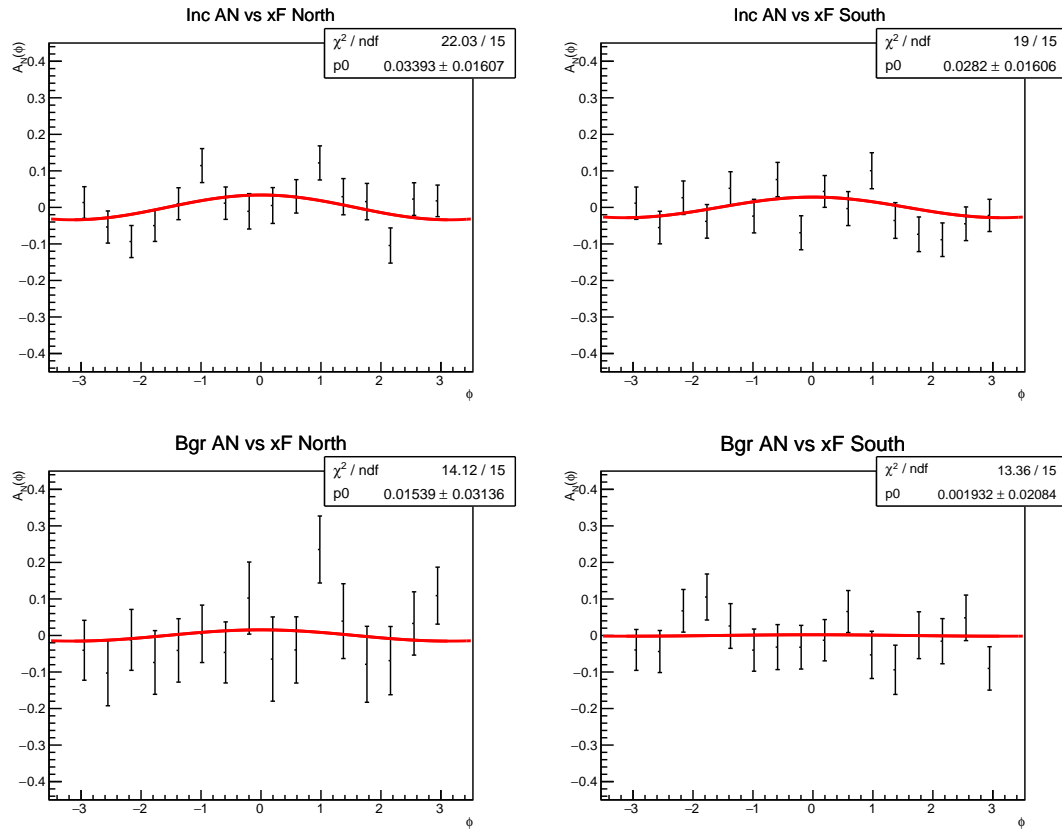


Figure 63: A_N for all x_F before tilt angle correction.

Figures 64 and 65 show inclusive and background asymmetry scanning with Maximum Likelihood method for $p + \text{Al}$ data. Tables 14 and 15 list the inclusive and background A_N that we found from the scanning.

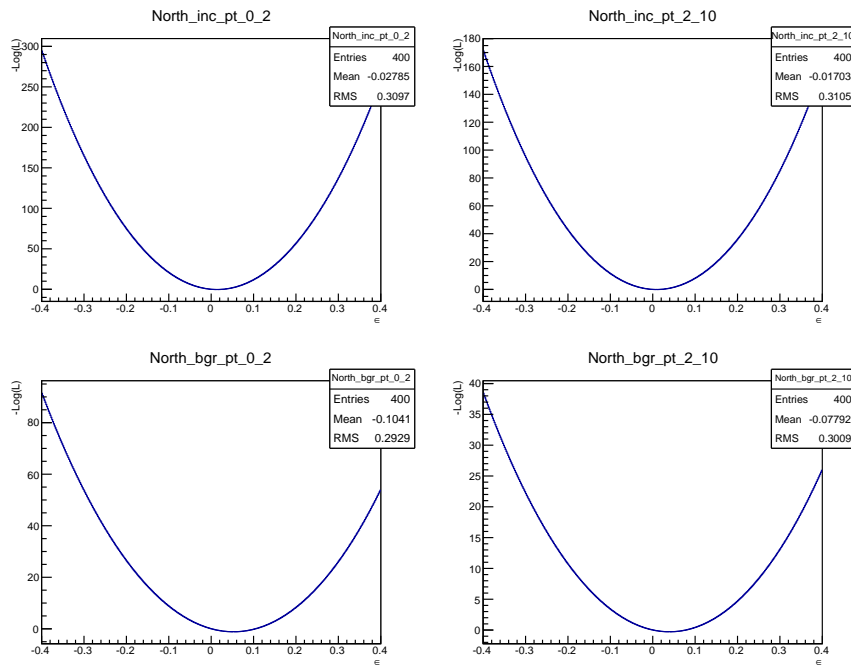


Figure 64: Epsilon scanning with $p+\text{Al}$ dataset. Top left and right plots show the epsilon scanning for inclusive A_N in North arm with $0 < p_T < 2$ GeV and $2 < p_T < 10$ GeV respectively. Bottom left and right plots show the epsilon scanning for background A_N in North arm with $0 < p_T < 2$ GeV and $2 < p_T < 10$ GeV respectively.

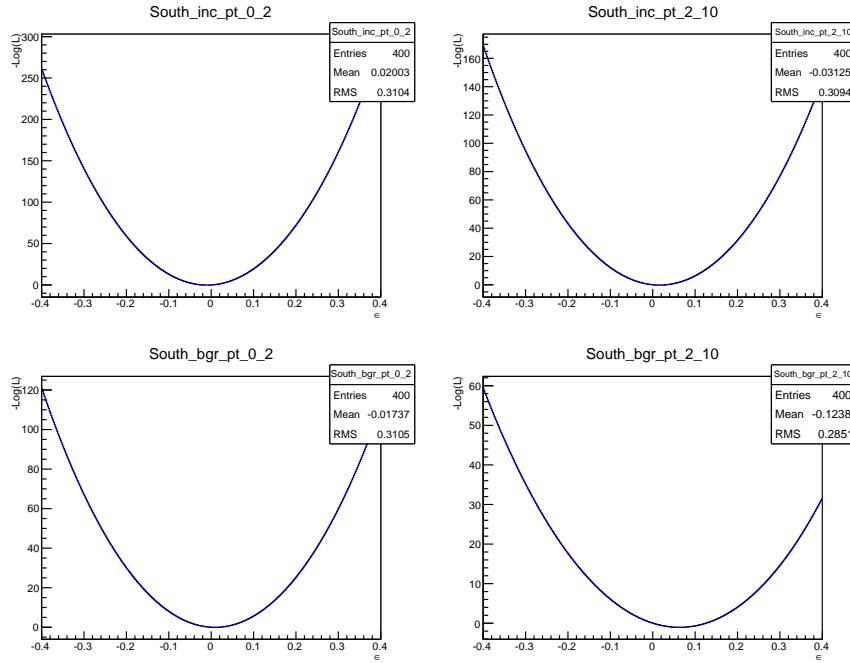


Figure 65: Epsilon scanning with $p+\text{Al}$ dataset. Top left and right plots show the epsilon scanning for inclusive A_N in South arm with $0 < p_T < 2 \text{ GeV}$ and $2 < p_T < 10 \text{ GeV}$ respectively. Bottom left and right plots show the epsilon scanning for background A_N in South arm with $0 < p_T < 2 \text{ GeV}$ and $2 < p_T < 10 \text{ GeV}$ respectively.

p_T	$A_N^{Inc.} \pm \delta A_N^{Inc.}(Stat.)$ North	$A_N^{Inc.} \pm \delta A_N^{Inc.}(Stat.)$ South
$p_T(GeV) \in 0 - 2$	0.031 ± 0.027	-0.018 ± 0.026
$p_T \in 2 - 10$	0.002 ± 0.037	0.051 ± 0.036
$x_F \in 0.05 - 0.11$	0.023 ± 0.029	-0.009 ± 0.025
$x_F \in 0.11 - 0.30$	0.025 ± 0.037	0.042 ± 0.038

Table 14: $A_N^{Inc.}$ in different p_T and x_F bins with $p + \text{Al}$ data

p_T	$A_N^{Bgr.} \pm \delta A_N^{Bgr.}(Stat.)$ North	$A_N^{Bgr.} \pm \delta A_N^{Bgr.}(Stat.)$ South
$p_T \in 0 - 2$	0.090 ± 0.050	-0.029 ± 0.048
$p_T \in 2 - 10$	0.113 ± 0.077	0.009 ± 0.084
$x_F \in 0.05 - 0.11$	0.091 ± 0.044	-0.040 ± 0.043
$x_F \in 0.11 - 0.30$	0.093 ± 0.129	0.234 ± 0.152

Table 15: $A_N^{Bgr.}$ in different p_T and x_F bins with $p + \text{Al}$ data

3.5.8 Azimuthal Fitting method with $p + \text{Al}$ collisions

Same with the procedure in $p + \text{Au}$ production, inclusive and background asymmetries with $p + \text{Al}$ data extracted from Spin Analyzer are shown in figures 66 to 69. The inclusive asymmetry is calculated from like-sign dimuon pairs within $2 - \sigma$ invariant mass range gotten from GPR fitting in section 3.4. The background asymmetry is calculated from the low-side-band dimuon invariant mass range from 1.5 to 2.4 GeV.

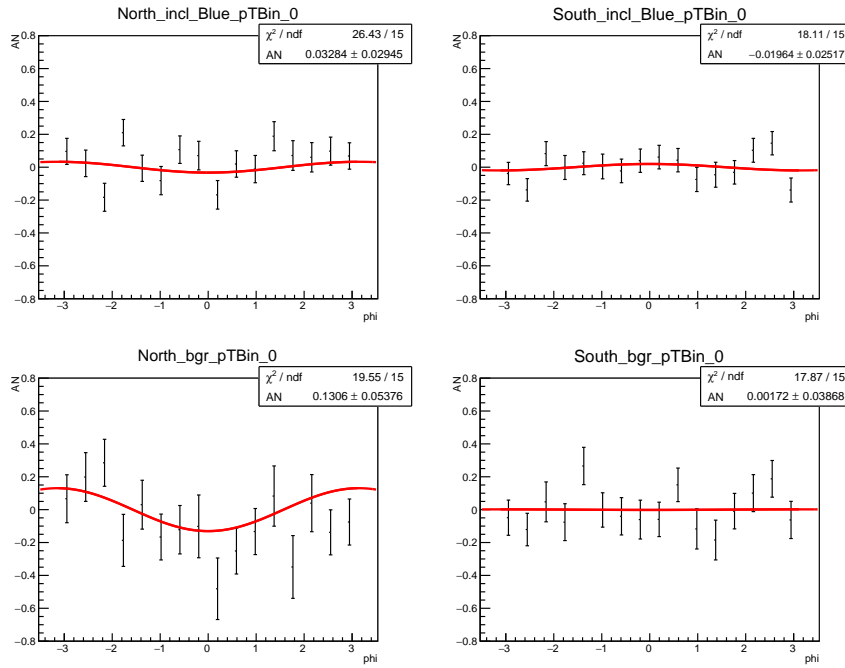


Figure 66: $p + \text{Al}$ Inclusive(left) and background(right) A_N with $0 < p_T < 2\text{GeV}$

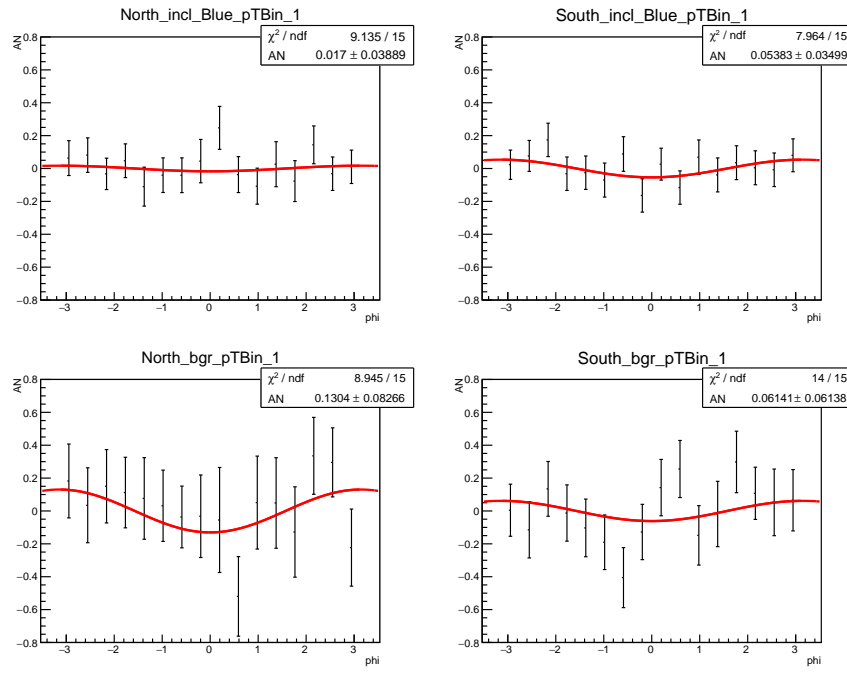


Figure 67: $p + \text{Al}$ Inclusive(left) and background(right) A_N with $2 < p_T < 10 \text{ GeV}$

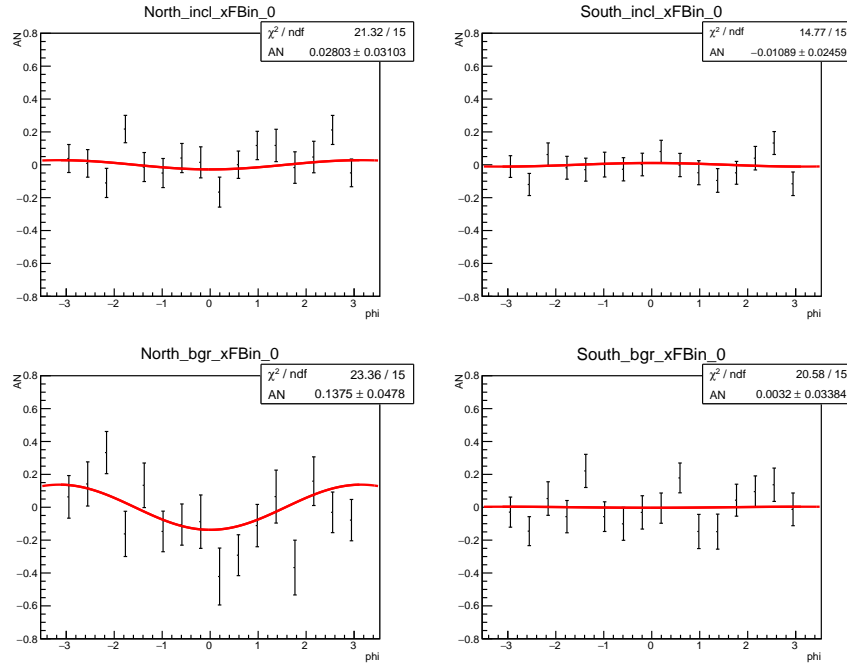


Figure 68: $p + \text{Al}$ Inclusive(left) and background(right) A_N with $0.05 < x_F < 0.11$

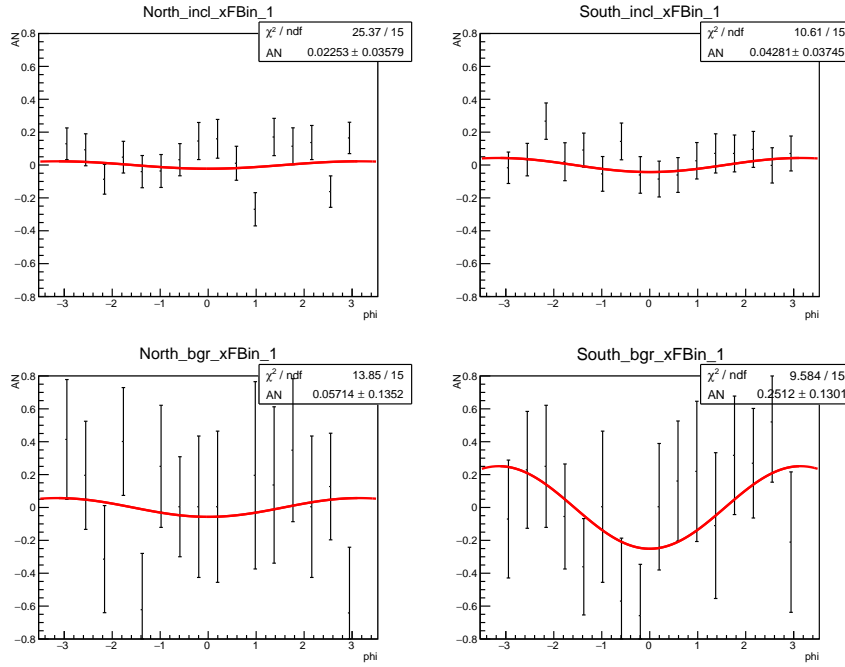


Figure 69: $p + \text{Al}$ Inclusive(left) and background(right) A_N with $0.11 < x_F < 0.30$

3.6 Crosschecks

As it can be seen in the previous subsections, the inclusive and background A_{NS} gotten from Maximum Likelihood method and Azimuthal Fitting method are in agreement with each other. However, it is still necessary to do some crosschecks in order to make our analysis more solid.

The crosschecks are done in different levels. Considering that the Spin Analyzer standardizes some steps for A_N extraction in the background, such as getting spin patterns from spin database, calculating fill-by-fill weighted polarization, and calculating A_N , verifying those procedures by a standalone code is quite useful.

This crosscheck is in the coding level. Constructing a standalone code can explicitly repeat the steps that Spin Analyzer does in the background. Another crosscheck is at the method level. So far, the inclusive and background A_N are obtained directly by combining all the data for the whole dataset; in a later subsection, a crosscheck based on fill-by-fill information will be described. Lastly, in order to avoid potential bias from a single person, an independent crosscheck done by people in another group is compared.

3.6.1 A crosscheck for Spin Analyzer using standalone code with $p+p$ data

In $p+p$ collisions, since both blue and yellow beam are polarized, equation! 34 is rewritten as:

$$\begin{aligned} A_N(\phi) &= \frac{\sigma^{\uparrow\uparrow}(\phi) + \sigma^{\uparrow\downarrow}(\phi) - (\sigma^{\downarrow\uparrow}(\phi) + \sigma^{\downarrow\downarrow}(\phi))}{\sigma^{\uparrow\uparrow}(\phi) + \sigma^{\uparrow\downarrow}(\phi) + \sigma^{\downarrow\uparrow}(\phi) + \sigma^{\downarrow\downarrow}(\phi)} \\ &= \frac{1}{P} * \frac{N^{\uparrow\uparrow}(\phi) + R_1 * N^{\uparrow\downarrow}(\phi) - (R_2 * N^{\downarrow\uparrow} + R_3 * N^{\downarrow\downarrow})}{N^{\uparrow\uparrow}(\phi) + R_1 * N^{\uparrow\downarrow}(\phi) - R_2 * N^{\downarrow\uparrow} + R_3 * N^{\downarrow\downarrow}} \end{aligned} \quad (52)$$

where $R_1 = L^{\uparrow\uparrow}/L^{\uparrow\downarrow}$, $R_2 = L^{\uparrow\uparrow}/L^{\downarrow\uparrow}$, $R_3 = L^{\uparrow\uparrow}/L^{\downarrow\downarrow}$ and polarization is the average polarization of all the runs weighted by the run luminosity with $P_{blue} = 57\%$ and $P_{yellow} = 57\%$.

The $A_N(\phi)$, relative luminosity (R_1 , R_2 , R_3) and polarization values for the blue and yellow beams obtained from the standalone code are exactly the same as those values calculated by the Spin Analyzer.

Figures 70 through 73 show the inclusive and background A_N fitting result from the standalone code. The difference of $A_N^{incl(bgr)}$ values between the Spin Analyzer and standalone is about 0.02σ in each bin. This slight discrepancy is due to the different uncertainty calculation for A_N in each ϕ bin. In the Spin Analyzer, only the number of events are considered in the statistical uncertainty, while in the standalone code the polarization is also taken into account.

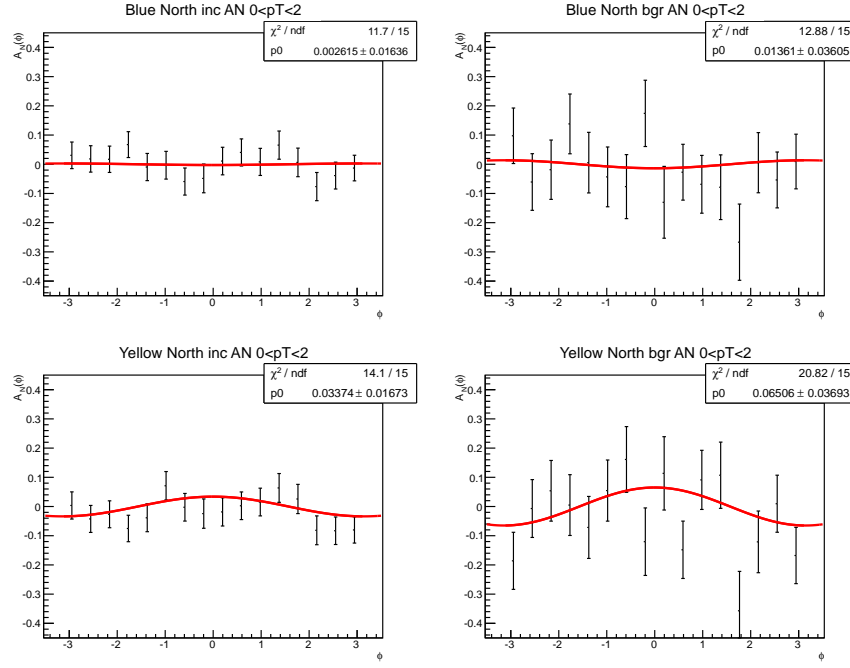


Figure 70: Inclusive and background A_N got from standalone code with $0 < p_T < 2$ GeV bin in North arm with $p + p$ data

This crosscheck was to see whether the Spin Analyzer deals with the spin patterns, relative luminosity and A_N calculation correctly. So a crosscheck just on p_T bins is sufficient.

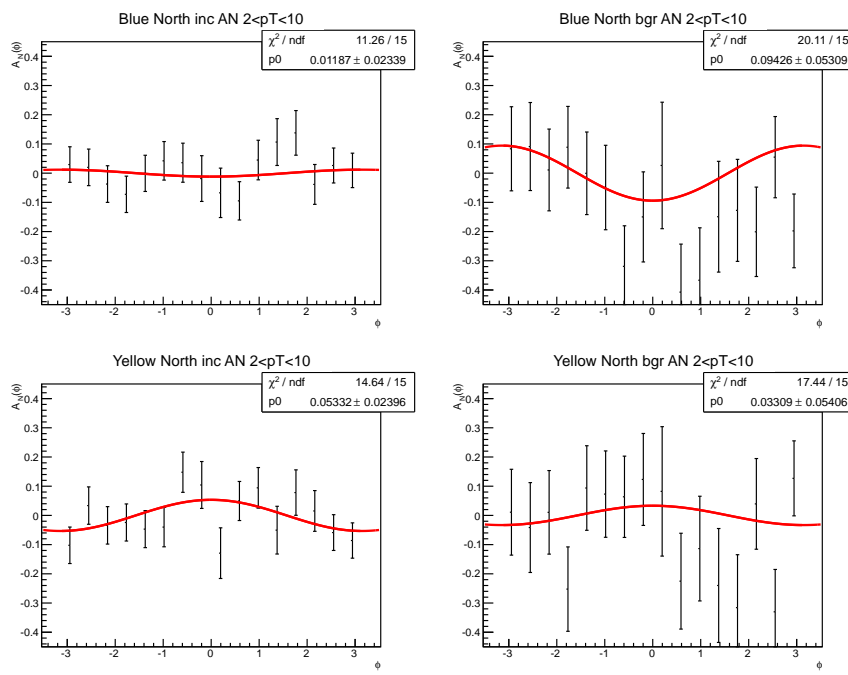


Figure 71: Inclusive and background A_N got from standalone code with $2 < p_T < 10$ GeV bin in North arm with $p + p$ data

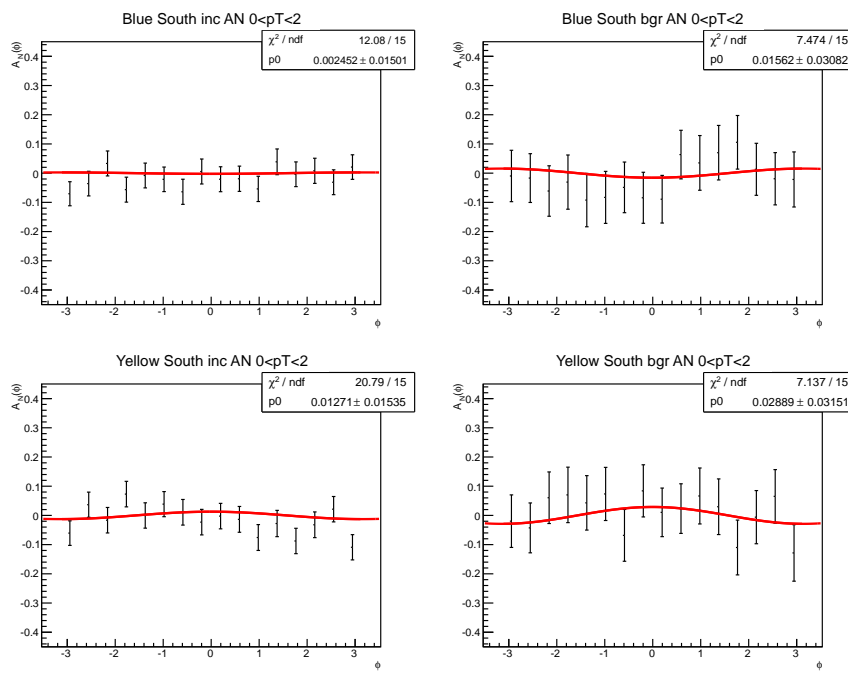


Figure 72: Inclusive and background A_N got from standalone code with $0 < p_T < 2$ GeV bin in South arm with $p + p$ data

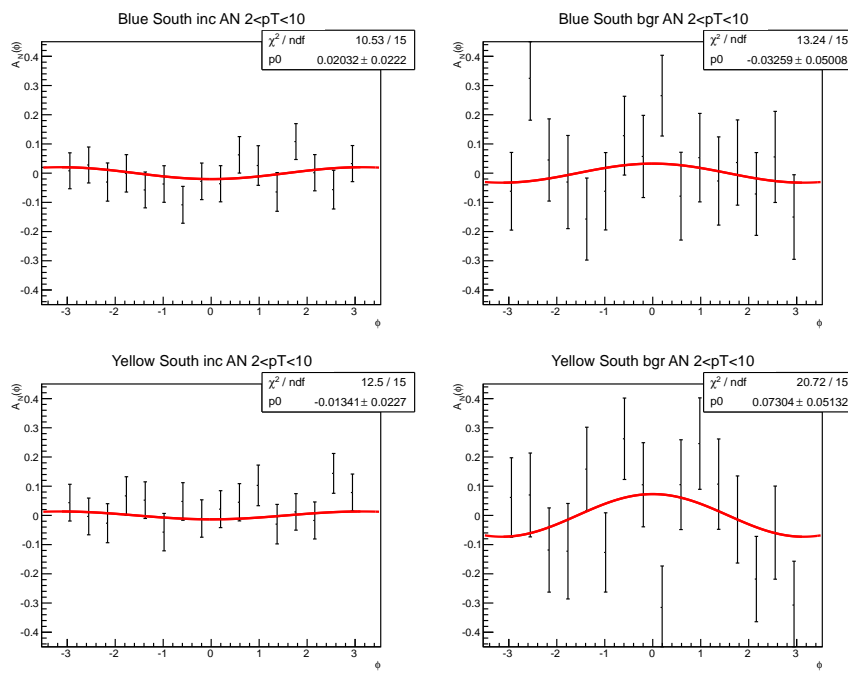


Figure 73: Inclusive and background A_N got from standalone code with $2 < p_T < 10$ GeV bin in South arm with $p + p$ data

3.6.2 Cross check for $p + \text{Au}$ data with standalone code

For $p + \text{Au}$ collisions, only the blue beam is polarized. So $A_N^{inl(bgr)}(\phi)$ can be calculated by equation 34. The polarization is the average polarization of all the runs weighted by the run luminosity with $P_{blue} = 60\%$.

Figures 74 to 76 show the inclusive/background A_N in different p_T and x_F bins. An approximately $1\%\sigma$ shift is observed due to the same reason described in the last subsection.

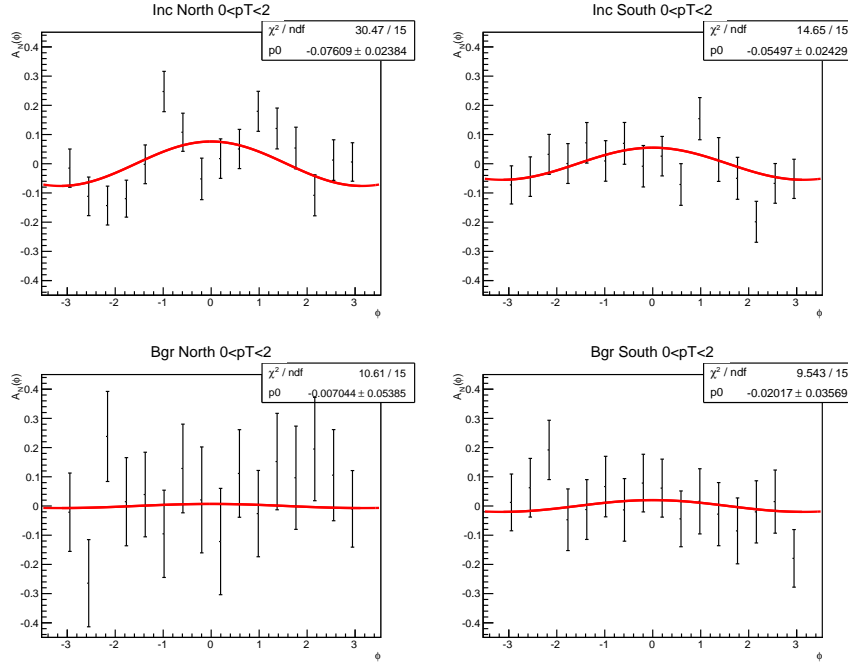


Figure 74: Inclusive and background A_N got from standalone code with $0 < p_T < 2$ GeV with $p + \text{Au}$ data

Considering that the $p + \text{Al}$ and $p + \text{Au}$ analysis use exactly the same code but

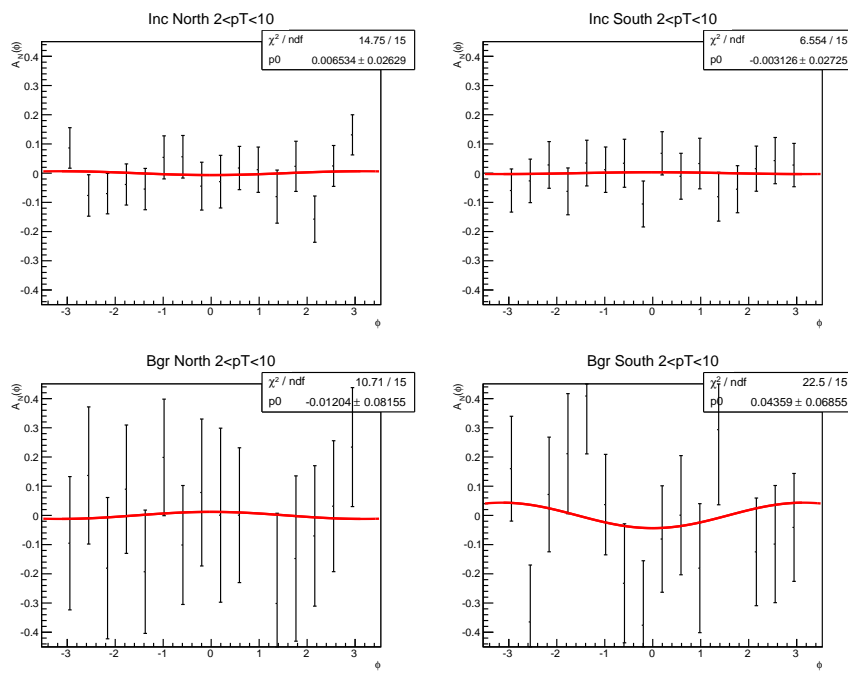


Figure 75: Inclusive and background A_N got from standalone code with $2 < p_T < 10$ GeV with $p + \text{Au}$ data

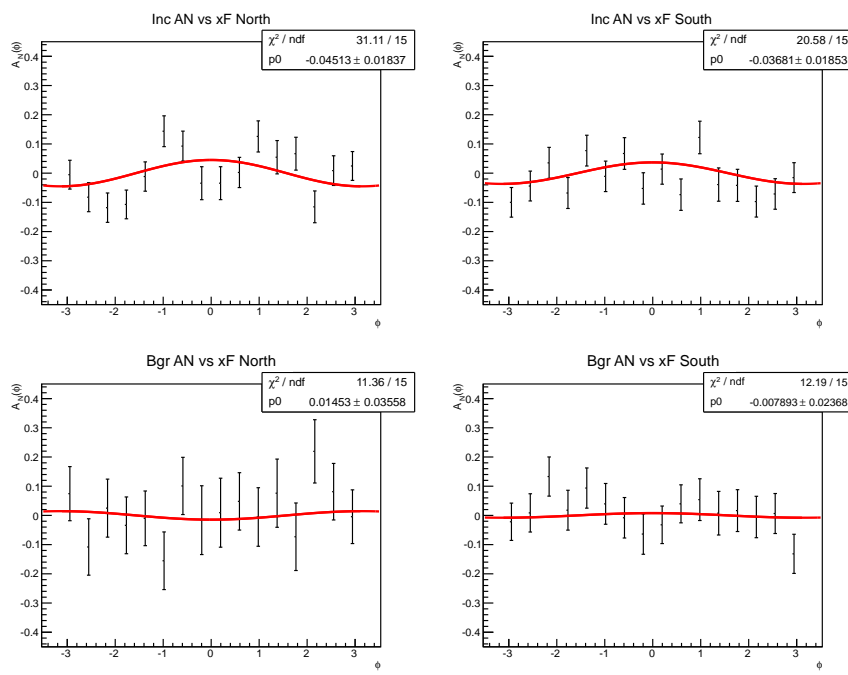


Figure 76: Inclusive and background A_N got from standalone code with combined x_F bin with $p + \text{Au}$ data

different input data files, in the code checking level it is sufficient to only check the $p + \text{Au}$ results.

3.6.3 Fill-by-Fill A_N estimation with Maximum Likelihood method

A fill-by-fill A_N estimation is also covered by Maximum Likelihood method. This is a crosscheck on whether there is a bias with combined data analysis which is caused by detector acceptance or/and trigger efficiency change within the whole data taking period. Figure 77 shows the Fill-by-Fill result. This result is compared with result obtained previously. The largest difference observed between these two methods is the inclusive A_N in North arm which varies about 0.15σ difference. Other than that, the differences are all less than 0.05σ . So we may conclude that result with combined data for this analysis is consistent with Fill-by-Fill method.

3.6.4 Cross check for $p+\text{Au}$ data from other collaborators

Another cross check also has been done with Sanghoon Lim and Marie Boer from LANL. I appreciate their time and work on this cross check. A event-by-event check has been performed before comparing the inclusive A_N . In this check, several quantities have been picked for comparison such as x , y , and z components of dimuon momentum, azimuthal angle of prompt dimuon and also the spin pattern. We got perfect match on this part. After that, Sanghoon and

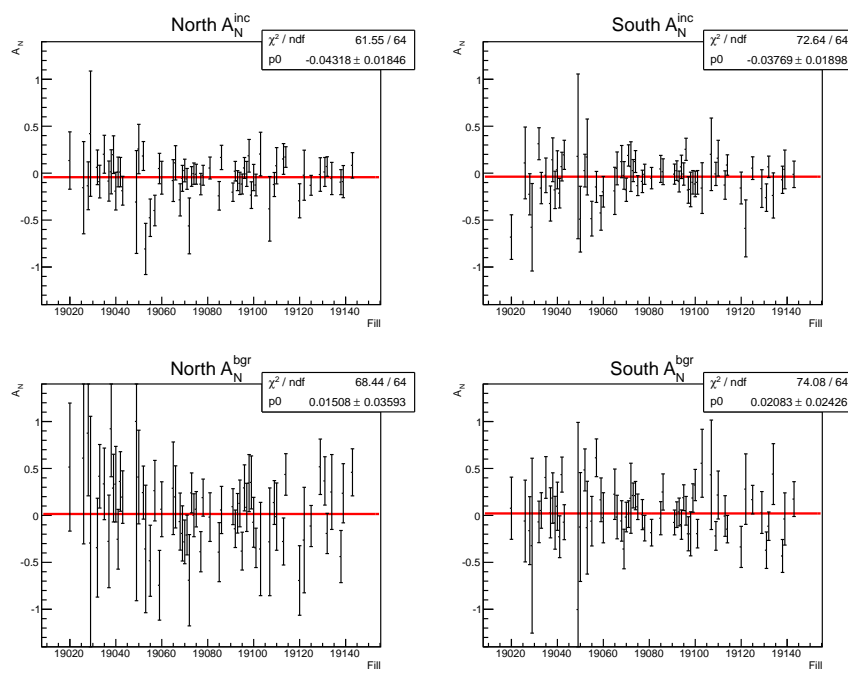


Figure 77: Fill-by-fill Inclusive and background A_N from Maximum Likelihood method with $p + \text{Au}$ data

I produced inclusive A_N using the same picoDST and good run list but different sets of dimuon cuts. Marie was using a different good run list and dimuon cuts. The purpose of this cross check is to see whether there is a coding issue. Rather than that, it also checks whether we introduced some bias when applying the cuts. Figure 78 shows the inclusive A_N for north arm with lower p_T bin. My result is perfectly matched with the result produced by Sanghoon. Marie's result is also consistent with mine. Considering that she was using a different dataset, the fluctuation shown in figure 78 is expected. With different cut sets, the inclusive A_N results are statistically consistent with each other.

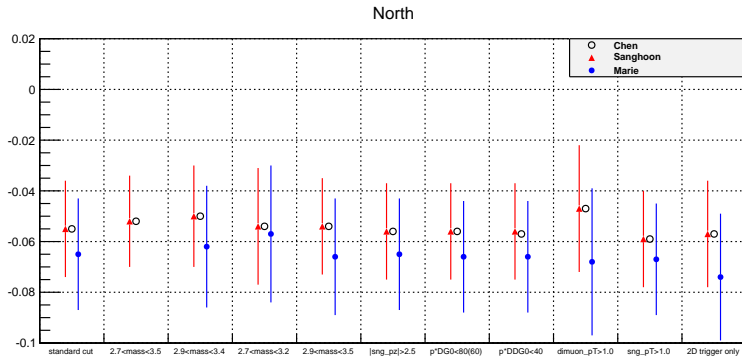


Figure 78: Comparing inclusive A_N from different cut sets with Sanghoon and Marie using $p + \text{Au}$ data

3.6.5 Crosscheck with BBC counts

It is necessary to cross check the BBC counts and dimuon yield (figures 79 to 81) for each bunch in each run, to make sure that the bunch crossing number is dealt

with correctly and the BBC counts read from Spin Database is reasonable.

From those plots, the abort gap can be clearly seen for both dimuon yield plots and BBC counts plots and the abort gap is placed in the right crossing bunch range.

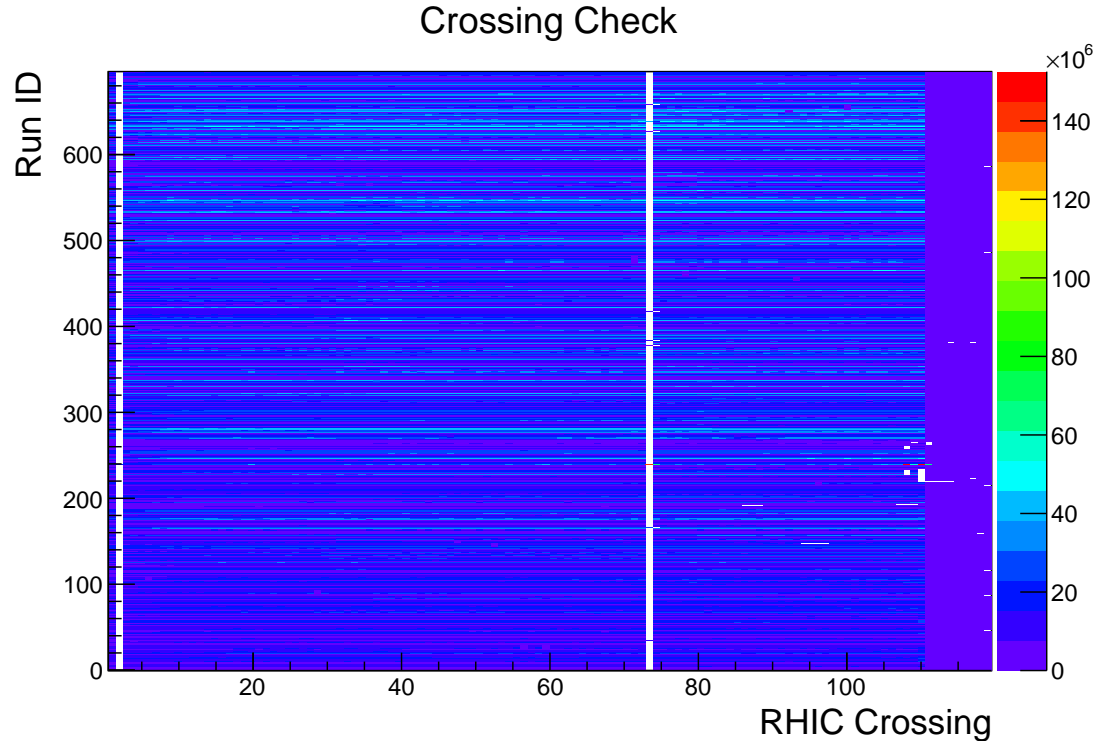


Figure 79: BBCin cross check with $p + p$ data: A 2-D plot filled with BBCin counts reading from Spin Database. X-axis is RHIC crossing number and Y-axis is Run ID number.

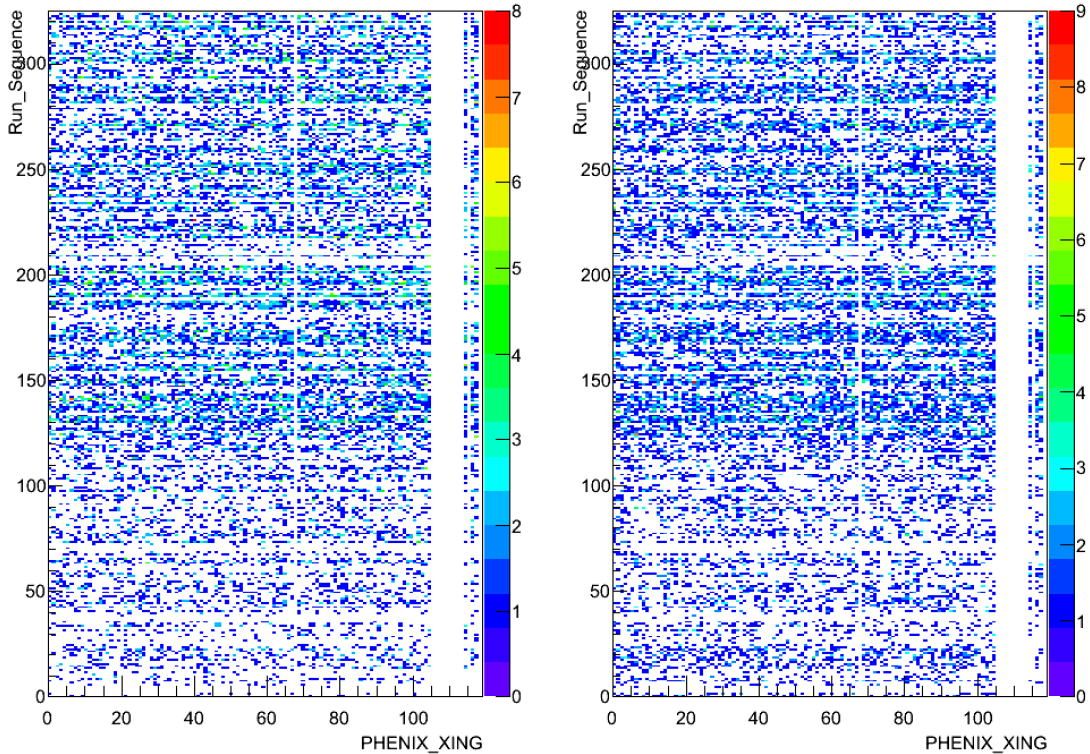


Figure 80: The left plot(North arm) and right plot(South arm) show dimuon yields for each bunch in each run in $p + \text{Au}$ collisions. The X axis is PHENIX crossing number and Y axis is run sequence number.

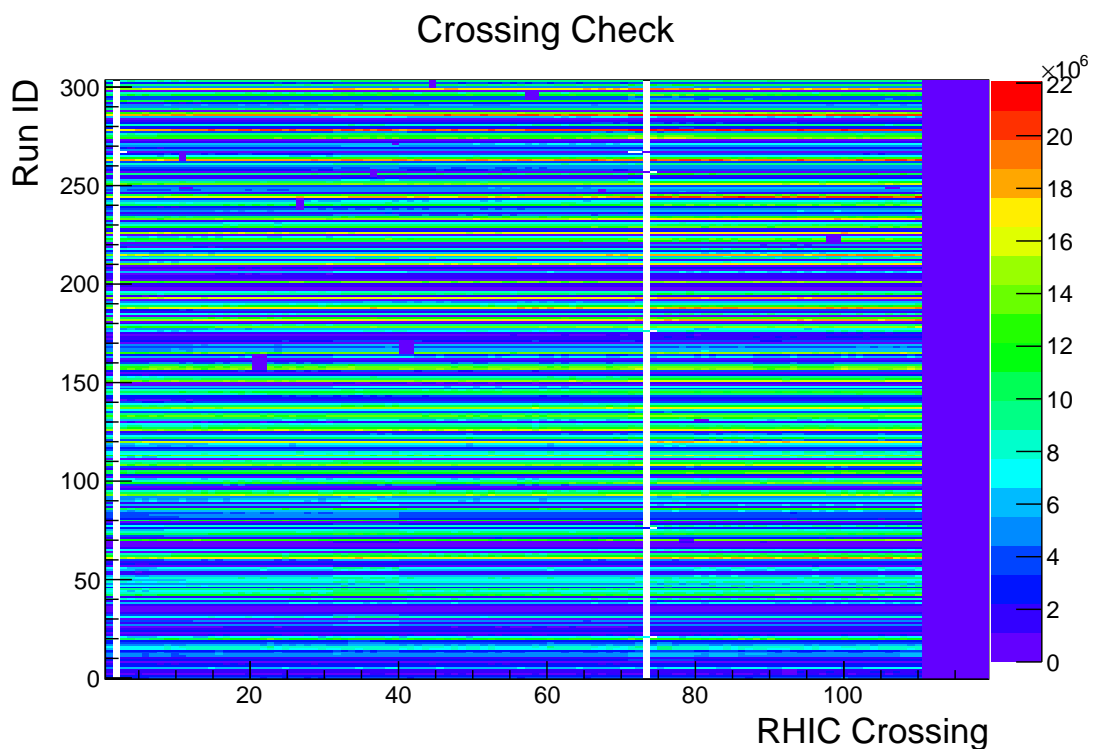


Figure 81: $p + \text{Au}$ BBCin cross check: A 2-D plot filled with BBCin counts read from Spin Database. X-axis is RHIC crossing number and Y-axis is Run ID number.

3.7 J/ψ A_N

Having obtained the inclusive and background asymmetries the signal asymmetry can be calculated from Equation 34 and Equation 35. Figures 82 to 83 show J/ψ A_N in different p_T and x_F bins with $p + p$ data. Figures 86 and 87 show J/ψ A_N in different p_T and x_F bins with $p + \text{Al}$ data, and figures 84 and 85 show J/ψ A_N in different p_T and x_F bins with $p + \text{Au}$ data. For those plots, the p_T (x_F) values for one bin is the average p_T (x_F) value over all the dimuon in that bin. Tables 16 to 19 list the J/ψ A_N in each arm for each p_T and x_F bin with $p + p$, $p + \text{Al}$ and $p + \text{Au}$ data.

p_T (GeV)	$A_N^{J/\psi} \pm \delta A_N^{J/\psi}(\text{Stat.})$ North	$A_N^{J/\psi} \pm \delta A_N^{J/\psi}(\text{Stat.})$ South
$p_T \in 0 - 2$	0.004 ± 0.017	0.013 ± 0.011
$p_T \in 2 - 10$	0.009 ± 0.023	0.011 ± 0.021
$x_F \in 0.05 - 0.11$	0.002 ± 0.027	0.001 ± 0.015
$x_F \in 0.11 - 0.30$	0.008 ± 0.021	0.017 ± 0.021

Table 16: $A_N^{J/\psi}$ in different p_T and x_F bins for Blue beam with $p + p$ data

p_T (GeV)	$A_N^{J/\psi} \pm \delta A_N^{J/\psi}$ (Stat.) North	$A_N^{J/\psi} \pm \delta A_N^{J/\psi}$ (Stat.) South
$p_T \in 0 - 2$	0.021 ± 0.017	0.002 ± 0.015
$p_T \in 2 - 10$	0.051 ± 0.023	0.000 ± 0.021
$x_F \in 0.05 - 0.11$	0.027 ± 0.018	0.006 ± 0.015
$x_F \in 0.11 - 0.30$	0.037 ± 0.021	-0.010 ± 0.021

Table 17: $A_N^{J/\psi}$ in different p_T and x_F bins for Yellow beam with $p + p$ data

p_T (GeV)	$A_N^{J/\psi} \pm \delta A_N^{J/\psi}$ (Stat.) North	$A_N^{J/\psi} \pm \delta A_N^{J/\psi}$ (Stat.) South
$p_T \in 0 - 2$	0.018 ± 0.037	-0.013 ± 0.037
$p_T \in 2 - 10$	-0.008 ± 0.045	0.031 ± 0.046
$x_F \in 0.05 - 0.11$	0.018 ± 0.039	0.062 ± 0.037
$x_F \in 0.11 - 0.30$	0.022 ± 0.039	-0.076 ± 0.042

Table 18: $A_N^{J/\psi}$ in different p_T and x_F bins for Blue beam with $p + \text{Al}$ data

p_T (GeV)	$A_N^{J/\psi} \pm \delta A_N^{J/\psi}$ (Stat.) North	$A_N^{J/\psi} \pm \delta A_N^{J/\psi}$ (Stat.) South
$p_T \in 0 - 2$	-0.067 ± 0.025	-0.074 ± 0.029
$p_T \in 2 - 10$	0.013 ± 0.031	0.012 ± 0.033
$x_F \in 0.05 - 0.11$	-0.027 ± 0.027	-0.058 ± 0.027
$x_F \in 0.11 - 0.30$	-0.045 ± 0.029	-0.019 ± 0.037

Table 19: $A_N^{J/\psi}$ in different p_T and x_F bins for Blue beam with $p + \text{Au}$ data

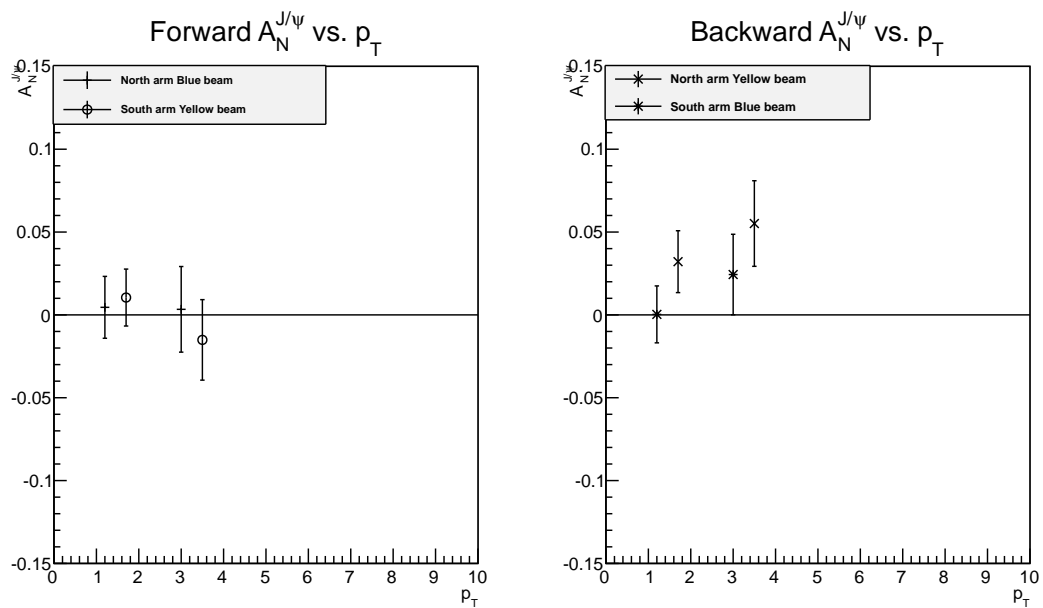


Figure 82: $A_N^{J/\psi}$ vs. p_T in $p + p$ collisions.

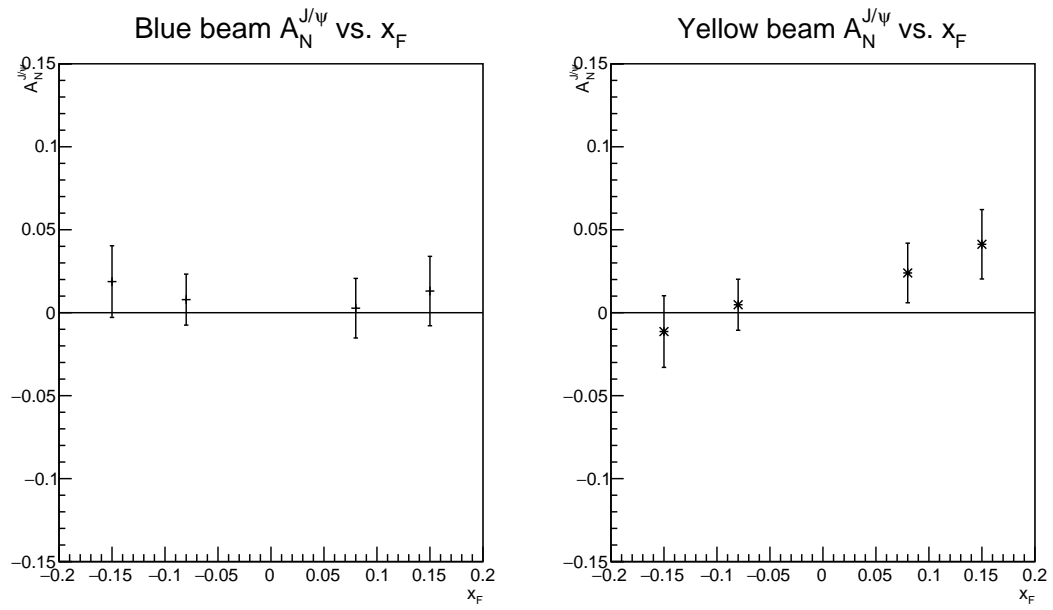


Figure 83: $A_N^{J/\psi}$ vs. x_F in $p + p$ collisions.

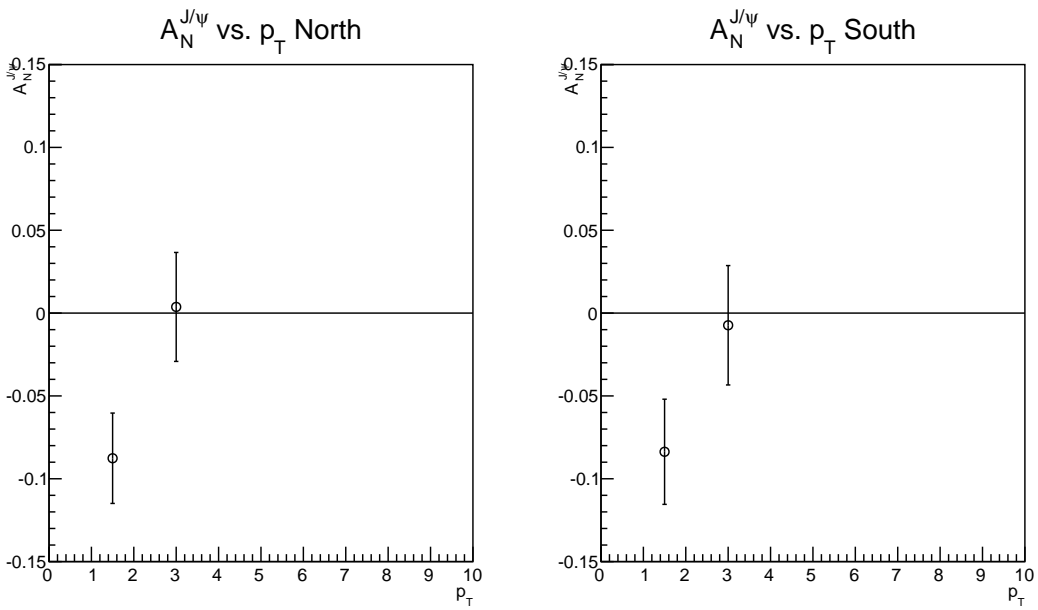


Figure 84: $A_N^{J/\psi}$ vs. p_T in $p + \text{Au}$ collisions.

3.8 Systematic Uncertainty Study

In this section the results of a number of systematic studies are presented where the stability of the result is being probed.

3.8.1 Shuffling result for transverse single spin asymmetry A_N

Shuffling the assigned spin direction for each bunch is a method to check for bunch related false asymmetries. Those can occur if the acceptance or efficiency of the trigger or the detector depend on the bunch structure or the timing. By definition the average asymmetries with randomized spins are zero, but the distribution of asymmetries from many randomized samples would be wider than expected.

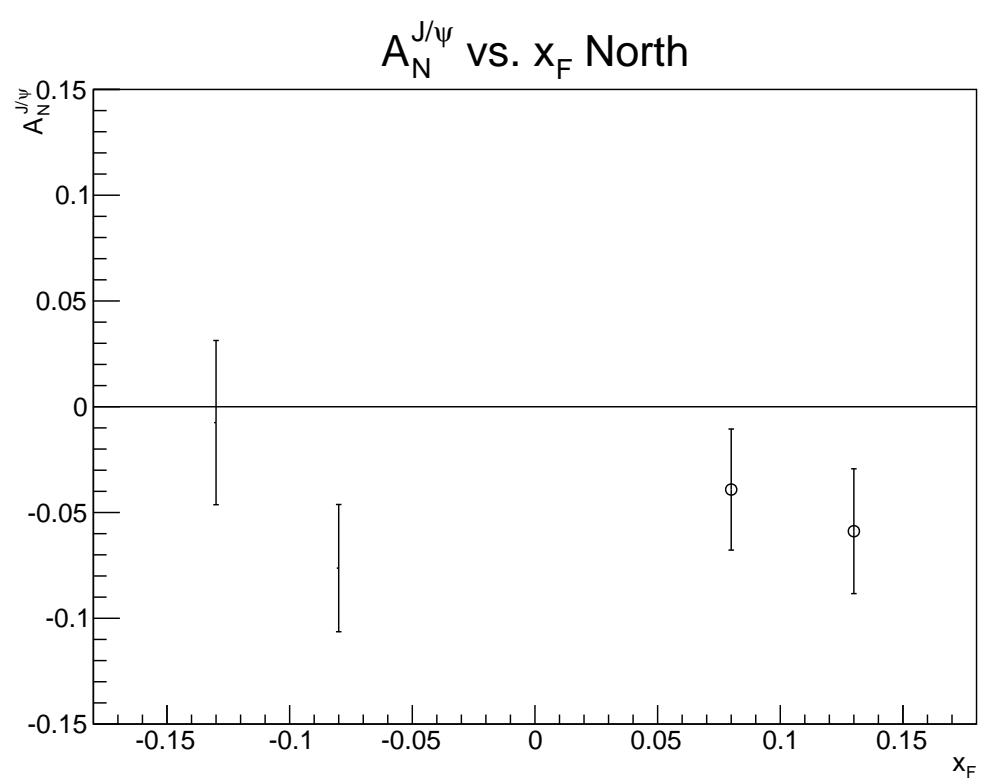


Figure 85: $A_N^{J/\psi}$ vs. x_F in $p + \text{Au}$ collisions.

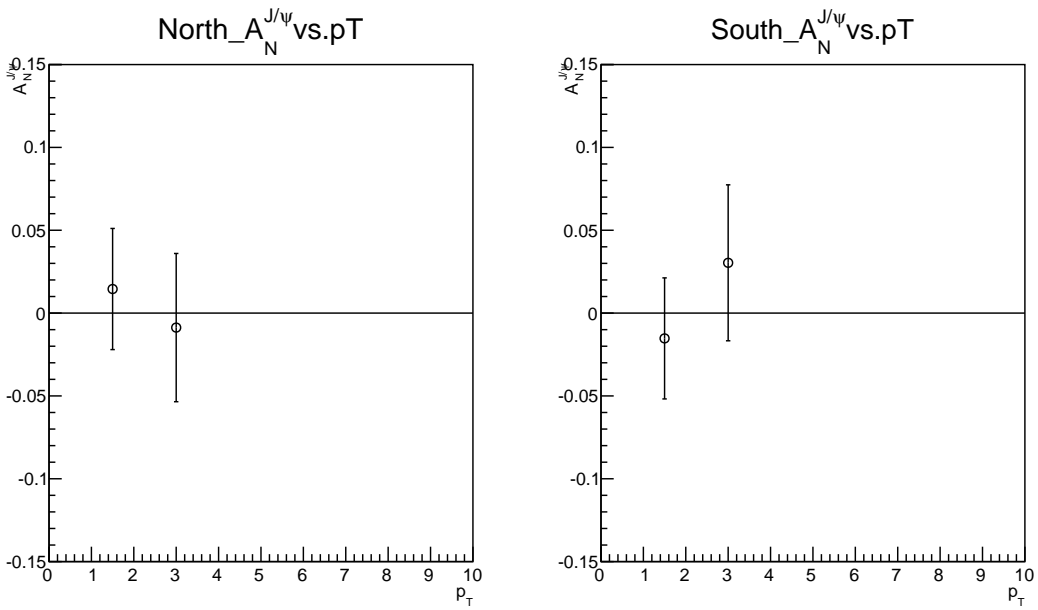


Figure 86: $A_N^{J/\psi}$ vs. p_T in $p + \text{Al}$ collisions.

Bunch shuffling is not sensitive to any physics related asymmetry, i.e., an asymmetry of the Minimum Bias trigger physics itself, background asymmetries or trigger biases. Of course, bunch shuffling is only sensitive to effects of a similar magnitude as the statistical error of the asymmetry.

The systematic bias has been checked with bunch shuffling. The procedure is:

1. randomly reassign the polarization direction for each bunch crossing,
2. recalculate the asymmetry,
3. repeat many times (in our case 10000 times) to produce a shuffled asymmetry distribution centered around zero,
4. compare width of shuffled distribution to statistical error on the physics

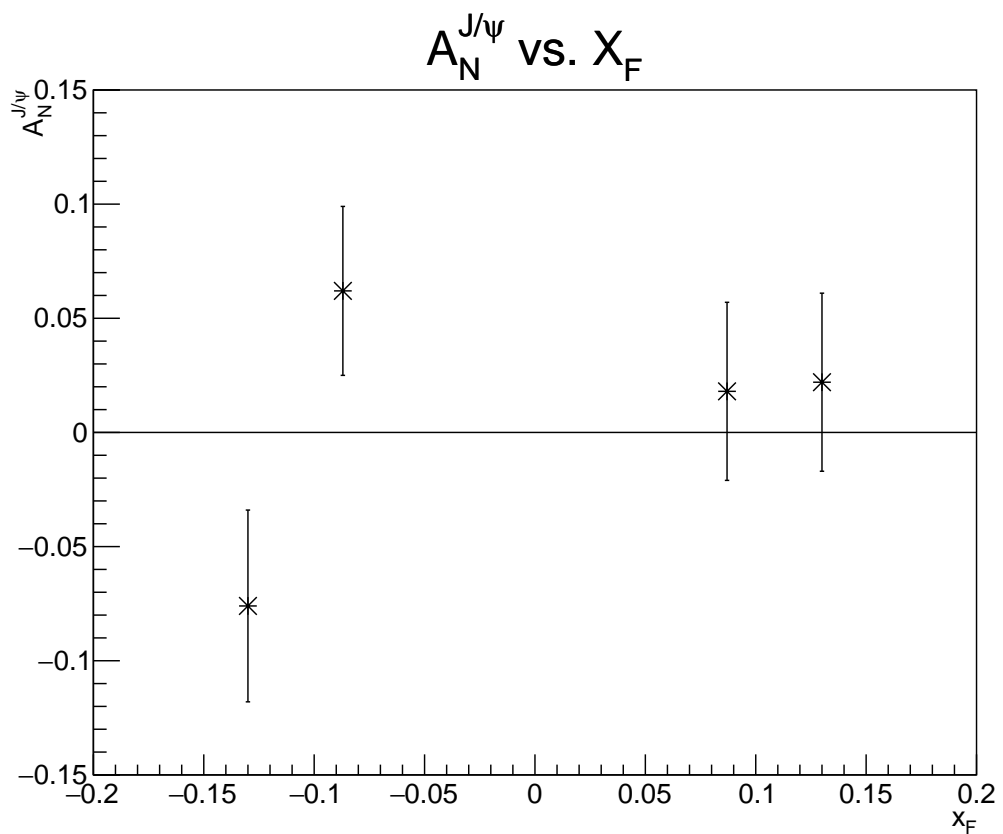


Figure 87: $A_N^{J/\psi}$ vs. x_F in $p + \text{Al}$ collisions.

asymmetry

Figures 88 and 89 show the bunch shuffling result for $p+p$ in two p_T bins; figures 90 and 91 show the bunch shuffling result for $p + \text{Au}$. Those plots show that the peak of the Gaussian distribution is around zero and σ is around one. The only difference of the analysis for $p + \text{Al}$ and $p + \text{Au}$ is the input files, so the bunch shuffling check is only done for $p + \text{Au}$.

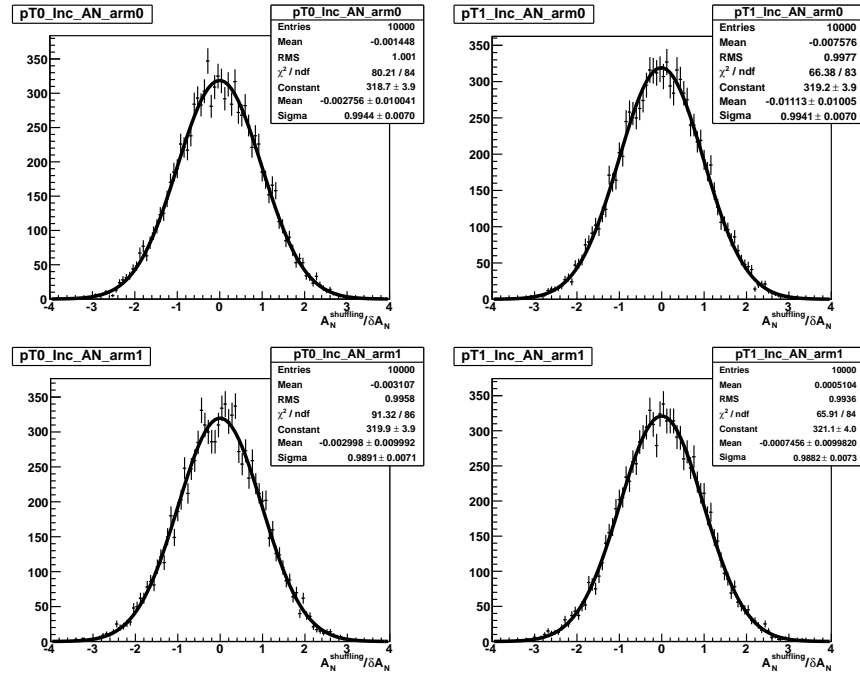


Figure 88: 10000 times bunch shuffling p_T -dependent inclusive asymmetries calculated by standalone code on blue beam with $p + p$ data

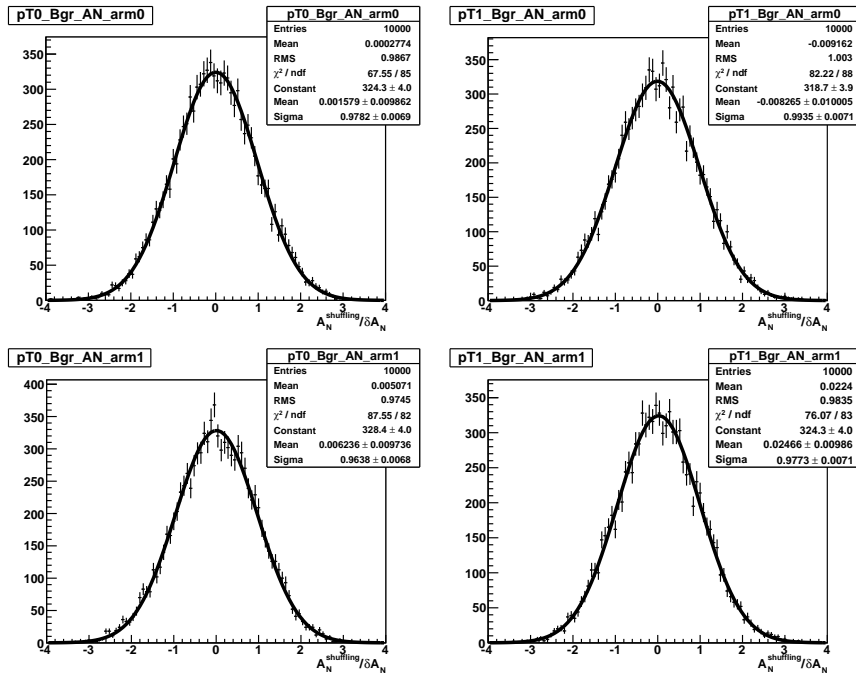


Figure 89: 10000 times bunch shuffling p_T -dependent background asymmetries calculated by standalone code on blue beam with $p + p$ data

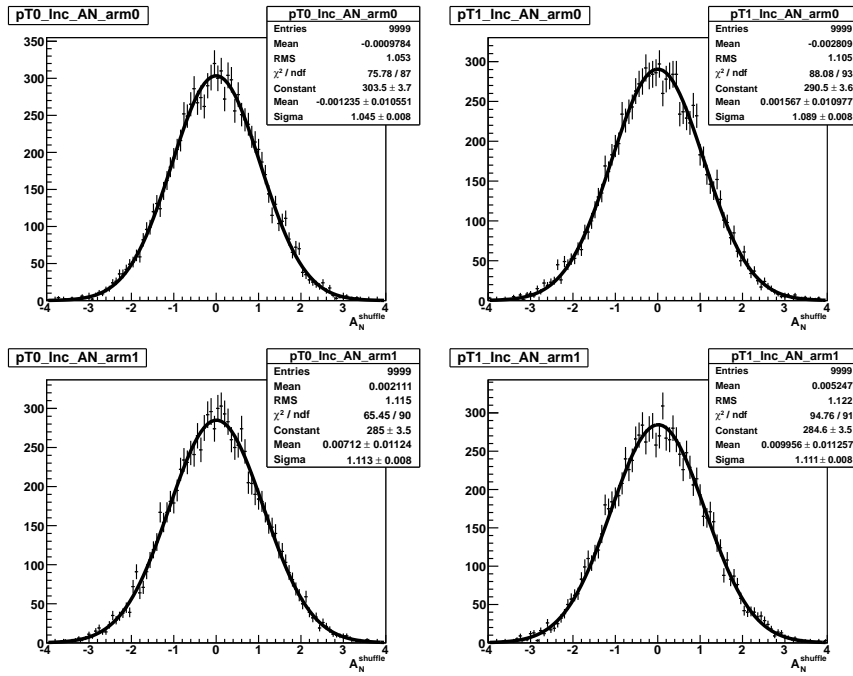


Figure 90: 10000 times bunch shuffling p_T -dependent inclusive asymmetries calculated by standalone code on blue beam with $p + \text{Au}$ data

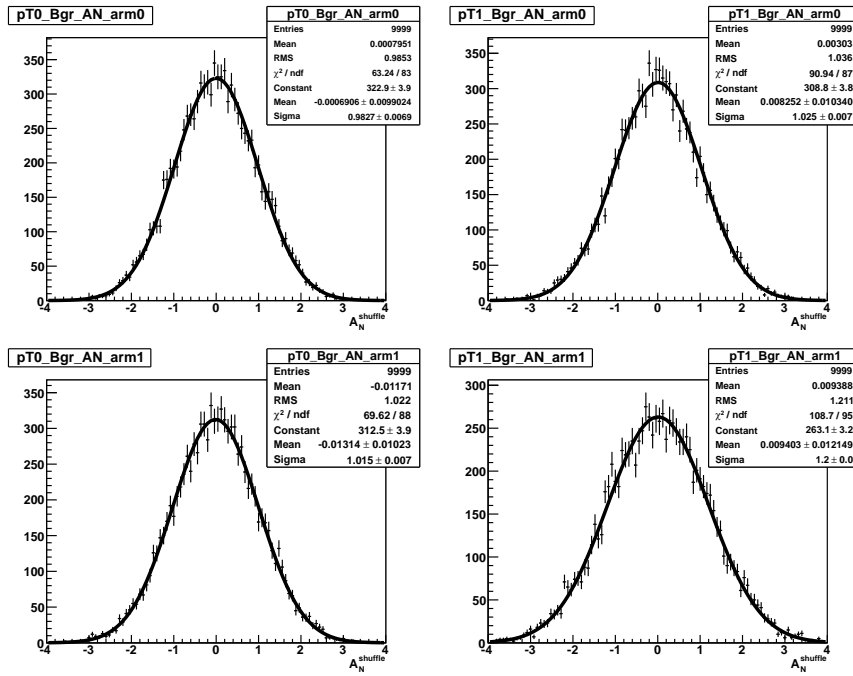


Figure 91: 10000 times bunch shuffling p_T -dependent background asymmetries calculated by standalone code on blue beam with $p + \text{Au}$ data

3.9 Systematic uncertainty from different invariant mass fitting methods

One source of systematic uncertainty comes from background fraction obtained from different fitting methods. The dimuon invariant mass is fitted by one Crystal Ball function for J/ψ peak, one Gaussian function for ψ' peak and a third-order polynomial for the background. The GPR method is believed to have the least bias since the assumption for the background invariant mass distribution is basing on the kernel function. Considering the bias-variance trade-off, it is always good to try both parameterized and unparameterized method for the background invariant mass distribution, although GPR will definitely have less bias than the fitting method with an assumed formula.

The fitting result with $p + p$ data is shown in figures 92 to 94; figures 95 to 100 show the fitting result for $p + \text{Al}$ and $p + \text{Au}$ data.

A set of background fraction is got using this new fitting function with $p + p$, $p + \text{Al}$ and $p + \text{Au}$ data. Tables 20, 21 and 22 list the background fraction for each bin. The differences between two different fitting methods in each bin are treated as a systematic uncertainty due to the background fraction and it propagates to the systematic uncertainty of $A_N^{J/\psi}$ using this equation:

$$\delta_{sys} A_N^{J/\psi} = \frac{\partial A_N^{J/\psi}}{\partial f} \delta f = \frac{A_N^{Incl.} - A_N^{bgr}}{(1-f)^2} \delta f. \quad (53)$$

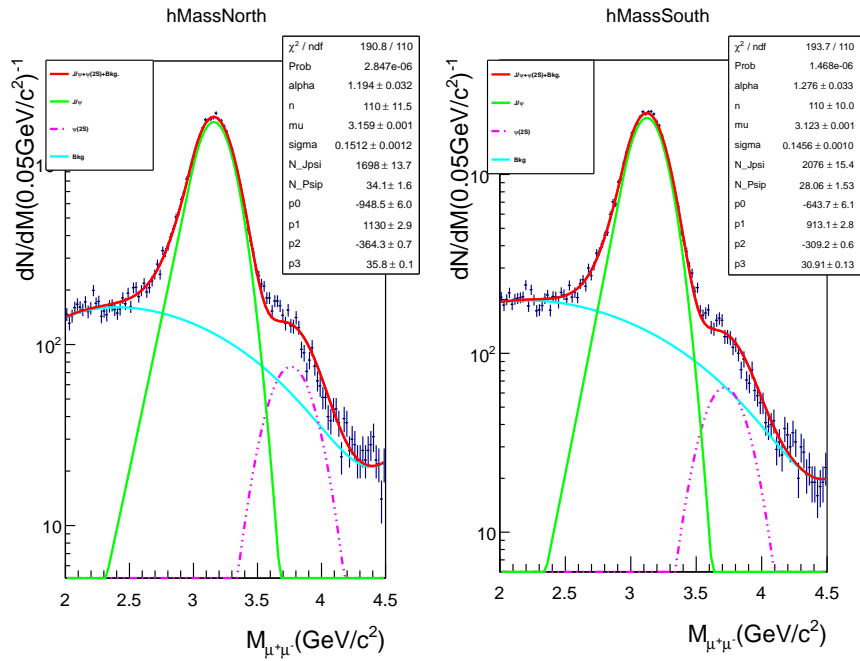


Figure 92: CB+Gaussian+Pol3 fitting in North and South arm with $p + p$ data

p_T (GeV)	$f_{Bgr} \pm \delta f_{Bgr}(\text{Stat.})(\%)$ North	$f_{Bgr} \pm \delta f_{Bgr}(\text{Stat.})(\%)$ South
$p_T \in 0 - 2$	11.6	10.7
$p_T \in 2 - 10$	9.0	8.2
$x_F \in 0.05 - 0.11$	12.8	11.4
$x_F \in 0.11 - 0.30$	6.4	5.7

Table 20: Background Fraction with CB + Gaussian + Pol3 for $p + p$ data

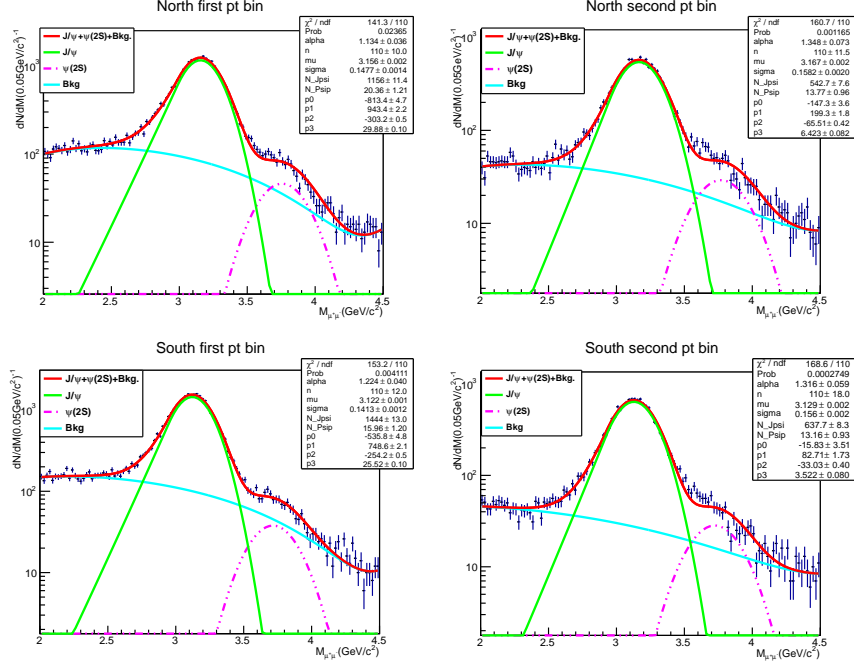


Figure 93: CB+Gaussian+Pol3 fitting in North and South arm for different p_T bins with $p + p$ data

p_T (GeV)	$f_{Bgr} \pm \delta f_{Bgr}(\text{Stat.})(\%)$ North	$f_{Bgr} \pm \delta f_{Bgr}(\text{Stat.})(\%)$ South
$p_T \in 0 - 2$	12.7	18.7
$p_T \in 2 - 10$	10.9	10.5
$x_F \in 0.05 - 0.11$	13.5	18.1
$x_F \in 0.11 - 0.30$	7.2	8.9

Table 21: Background Fraction with CB + Gaussian + Pol3 for $p + \text{Au}$ data

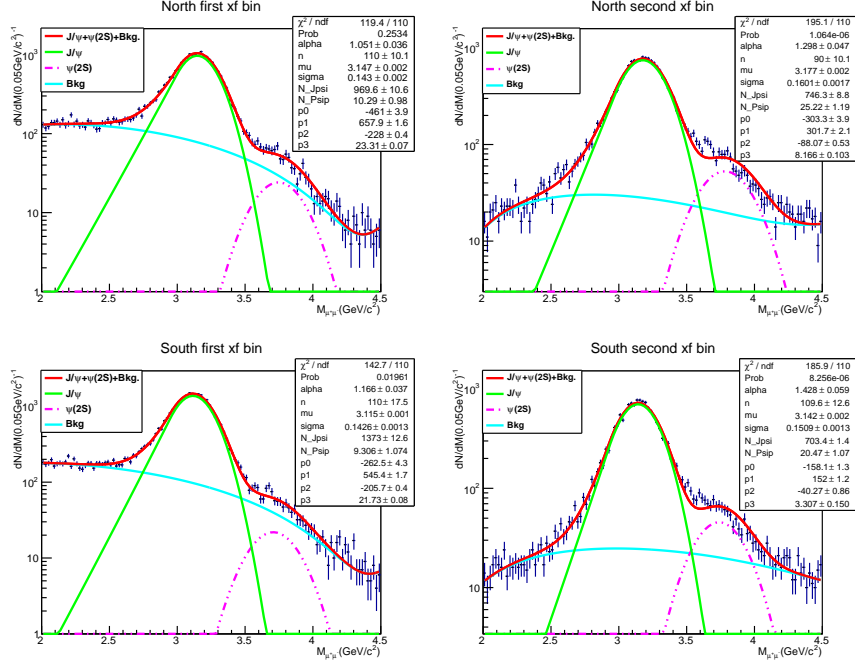


Figure 94: CB+Gaussian+Pol3 fitting in North and South arm for different x_F bins with $p + p$ data

p_T (GeV)	$f_{Bgr} \pm \delta f_{Bgr}(Stat.)\% \text{ North}$	$f_{Bgr} \pm \delta f_{Bgr}(Stat.)\% \text{ South}$
$p_T \in 0 - 2$	11.9	13.8
$p_T \in 2 - 10$	7.1	8.9
$x_F \in 0.05 - 0.11$	13.4	14.3
$x_F \in 0.11 - 0.30$	3.5	7.2

Table 22: Background Fraction with CB + Gaussian + Pol3 for $p + Al$ data

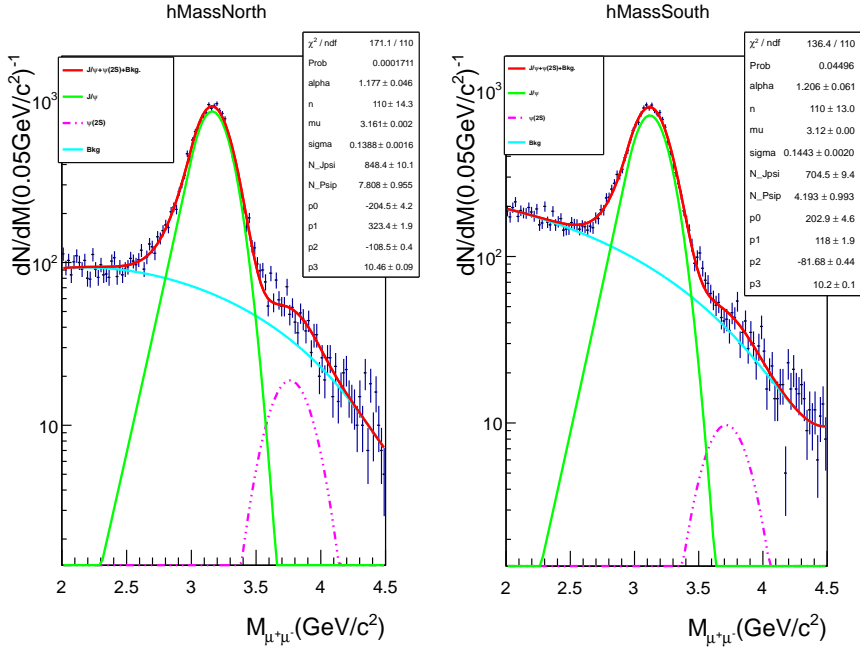


Figure 95: CB+Gaussian+Pol3 fitting in North and South arm with $p + \text{Au}$ data

3.9.1 Combining Systematic Uncertainty from different sources

So far, two sources of systematic uncertainty are discussed in the previous sections. Source one is the systematic uncertainty coming from using different analysis methods. The other systematic uncertainty source is related to the determination of the background fraction with different fitting methods. These sources are independent with each other. Therefore, they can be combined quadratically:

$$\delta_{\text{sys.}} A_N = \sqrt{\delta_{\text{sys.}(ML)}^2 A_N + \delta_{\text{sys.}(fit)}^2 A_N} \quad (54)$$

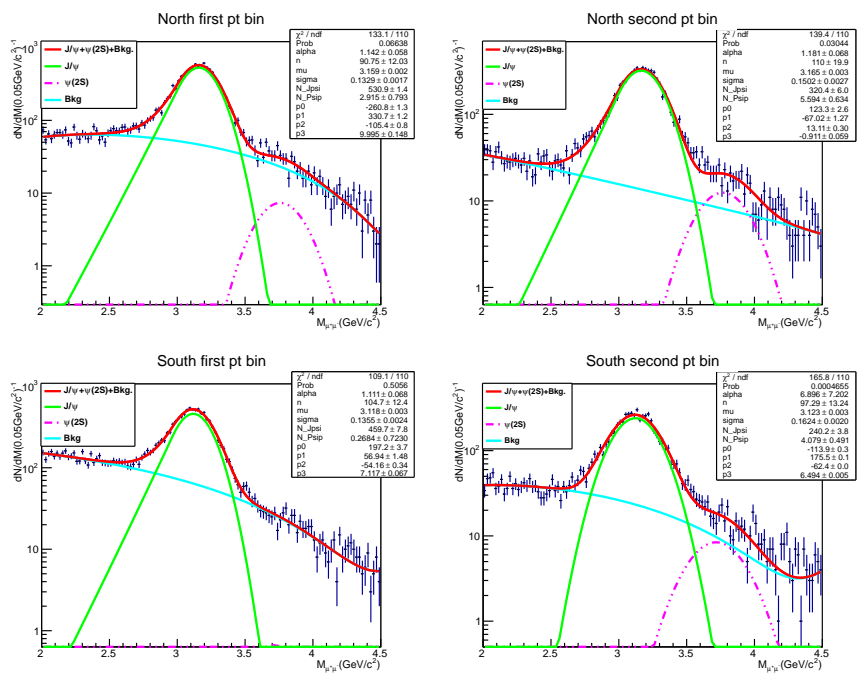


Figure 96: CB+Gaussian+Pol3 fitting in North and South arm for different p_T bins with $p + \text{Au}$ data

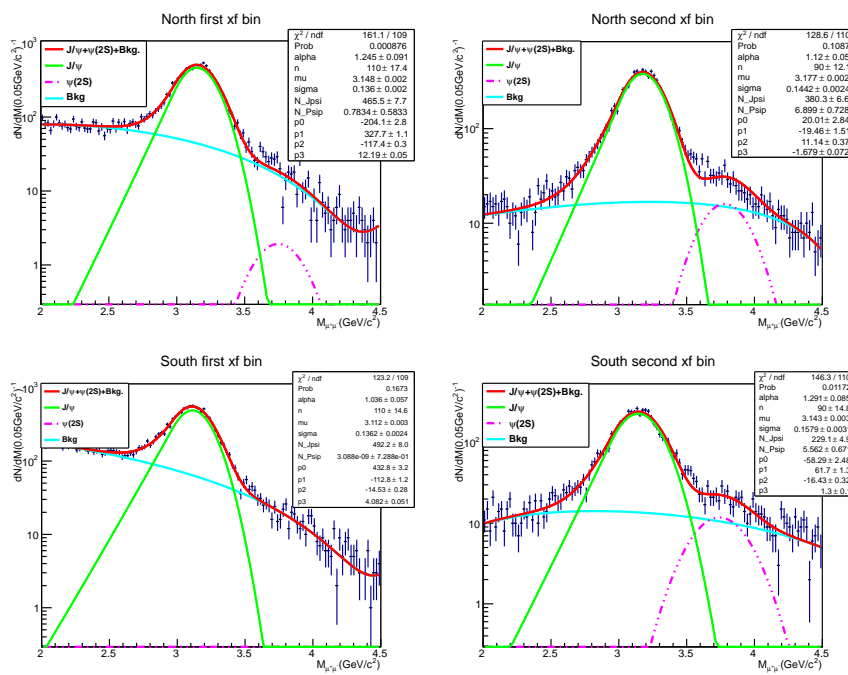


Figure 97: CB+Gaussian+Pol3 fitting in North and South arm for different x_F bins with $p + \text{Au}$ data

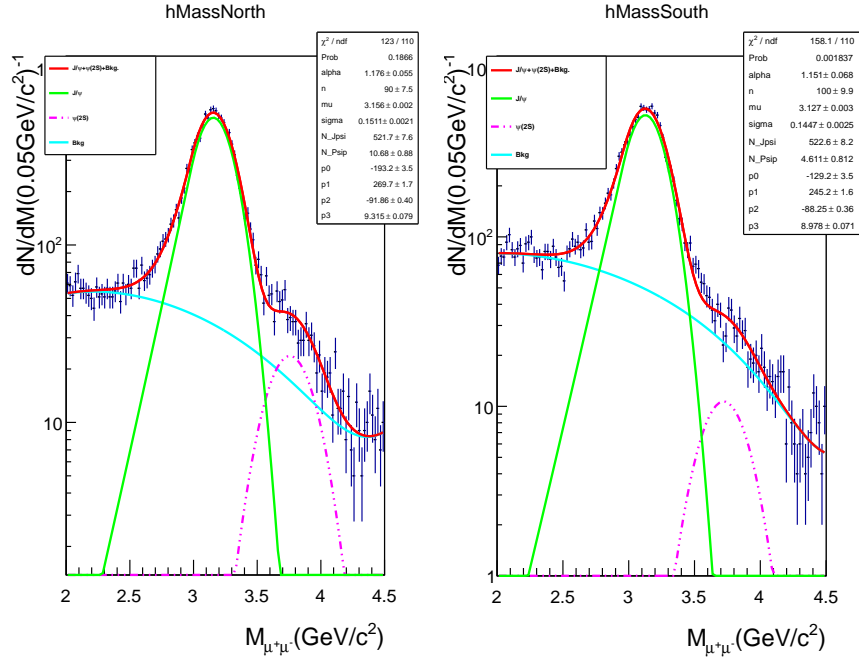


Figure 98: CB+Gaussian+Pol3 fitting in North and South arm with $p + \text{Al}$ data

4 Final Result and Discussion

4.1 Combined result in $p + p$ data for Blue and Yellow beams

The transverse single spin asymmetries A_N in prompt muons productions (mostly from open heavy flavor decays) are measured as a function of x_F and p_T by using Run15 data.

For $p + p$ collision, since both proton beams are polarized, we need to combine blue beam with yellow beam for forward and backward A_N using the following equation:

$$A_N^{comb.} = \frac{A_N^{Blue} \cdot 1/(\delta_{stat.} A_N^{Blue})^2 + A_N^{Yellow} \cdot 1/(\delta_{stat.} A_N^{Yellow})^2}{1/(\delta_{stat.} A_N^{Blue})^2 + 1/(\delta_{stat.} A_N^{Yellow})^2} \quad (55)$$

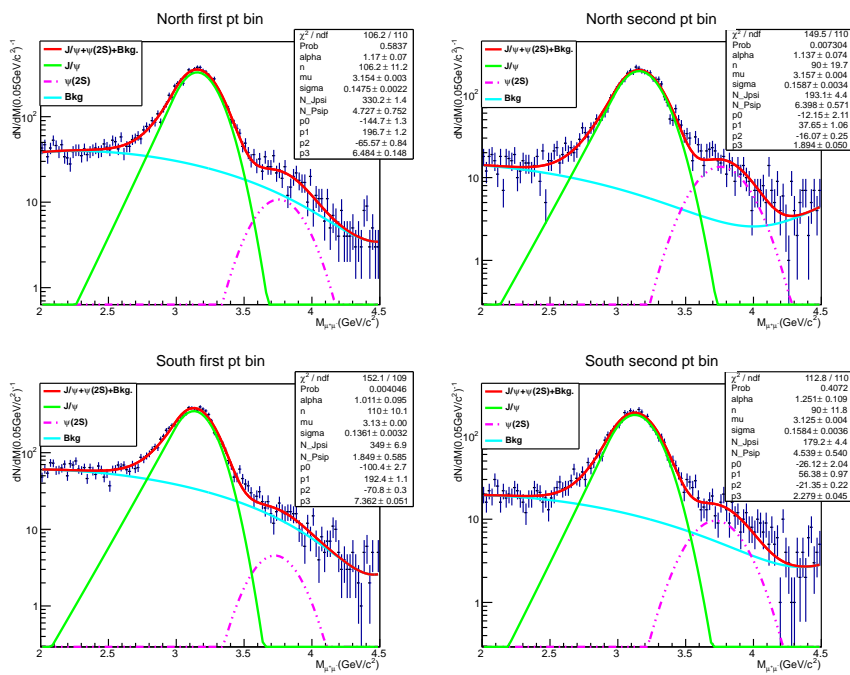


Figure 99: CB+Gaussian+Pol3 fitting in North and South arm for different p_T bins with $p + \text{Al}$ data

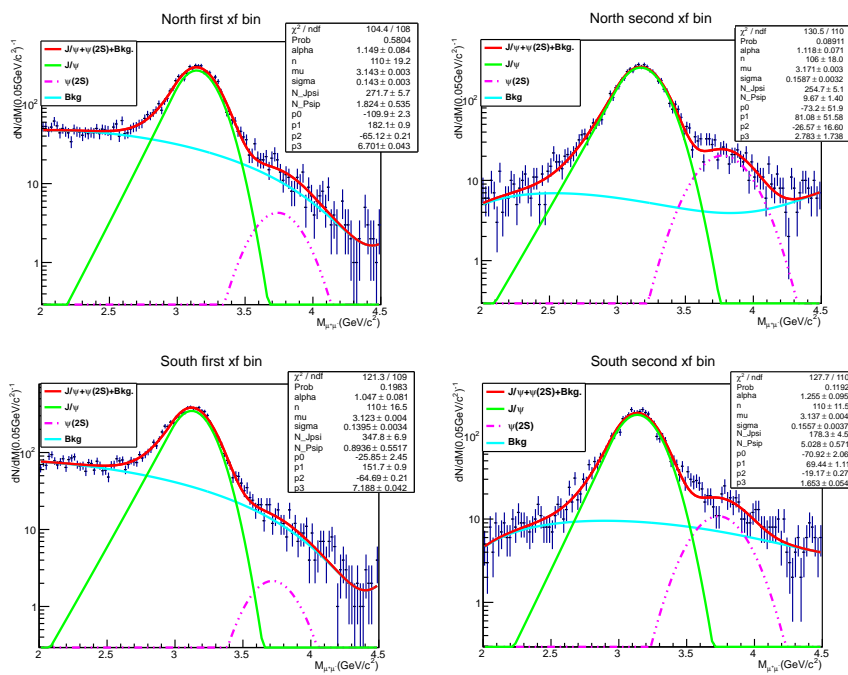


Figure 100: CB+Gaussian+Pol3 fitting in North and South arm for different x_F bins with $p + \text{Al}$ data

The statistic uncertainty is given by:

$$\delta_{stat.}^2 A_N^{comb.} = \frac{1}{1/(\delta_{stat.} A_N^{Blue})^2 + 1/(\delta_{stat.} A_N^{Yellow})^2} \quad (56)$$

The systematic uncertainty from background fraction is given by:

$$\delta_{sys.} A_N^{comb.} = \sqrt{\left(\frac{\partial A_N^{comb.}}{\partial A_N^{Blue}} \delta_{sys.} A_N^{Blue} \right)^2 + \left(\frac{\partial A_N^{comb.}}{\partial A_N^{Yellow}} \delta_{sys.} A_N^{Yellow} \right)^2} \quad (57)$$

4.2 Finalized result for $A_N^{J/\psi}$ with Run15 data

Figure 101 shows the TSSA for J/ψ production, $A_N^{J/\psi}$, in two p_T bins in forward and backward kinematics in $p + p$, $p + \text{Al}$ and $p + \text{Au}$ collisions. The 2015 $p + p$ data is consistent with the previous result of $A_N^{J/\psi}$ from the 2006 and 2008 data [7] within one-standard-deviation. The 2015 $p + p$ data favor a positive asymmetry (at the 2σ level) in the high- p_T bin in backward rapidity. With limited statistics, the A_N in all p_T and x_F bins for $p + \text{Al}$ collisions are consistent with zero. In $p + \text{Au}$ collisions, the asymmetry in the high- p_T bin is consistent with zero, although there is a trend to a non-zero A_N (at the 2σ level) in the low- p_T bin in both the forward and backward directions.

Figure 102 shows the $A_N^{J/\psi}$ as a function of x_F . In the $p + p$ data, it is consistent with the previous PHENIX results [7] and a $\sim 2\sigma$ positive A_N is observed in the backward higher x_F bin. The result for the other x_F bins are consistent with zero. For the $p + \text{Au}$ data, a $\sim 2\sigma$ negative A_N is observed in the forward high- x_F bin and the backward low- x_F bin. A scale uncertainty from the polarization (3%) is

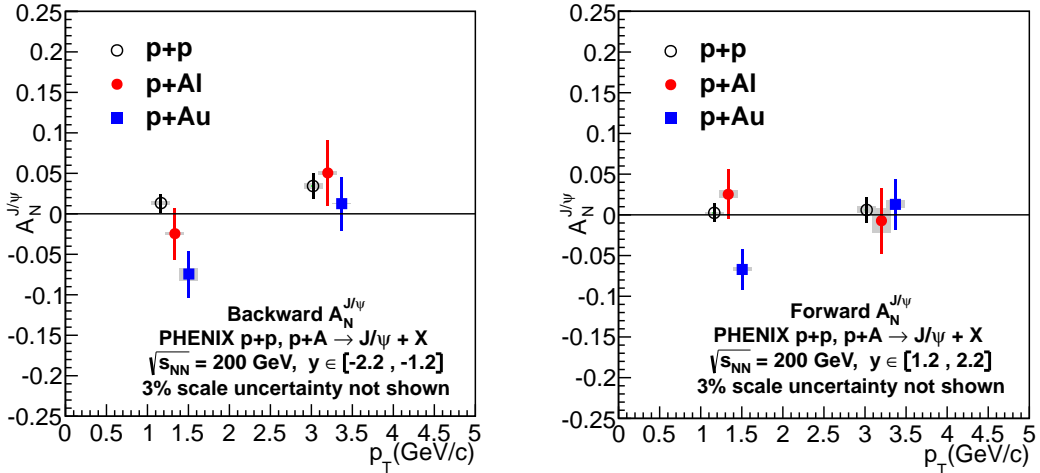


Figure 101: Backward ($x_F < 0$) and forward ($x_F > 0$) $A_N^{J/\psi}$ vs. p_T for the $p+p$, $p+Al$ and $p+Au$ collision data. The gray boxes show the systematic uncertainty. The value of p_T for $p+Al$ and $p+Au$ have been shifted horizontally for clarity.

not included in both Figure 101 and Figure 102.

4.3 Further Study on $p+Au$ data for lower p_T bin

The result for $p+Au$ data in lower p_T bin shows a negative A_N with 2 standard deviations away from zero while the A_N in high p_T bin is consistent with zero. We would like to see what causes this non-zero asymmetry in the low p_T bin. One way to do the further investigation is to split the low p_T bin into more bins. In that way, we can check specifically which bin makes the greatest contribution to the non-zero asymmetry. The other way to do it is to make binning basing on

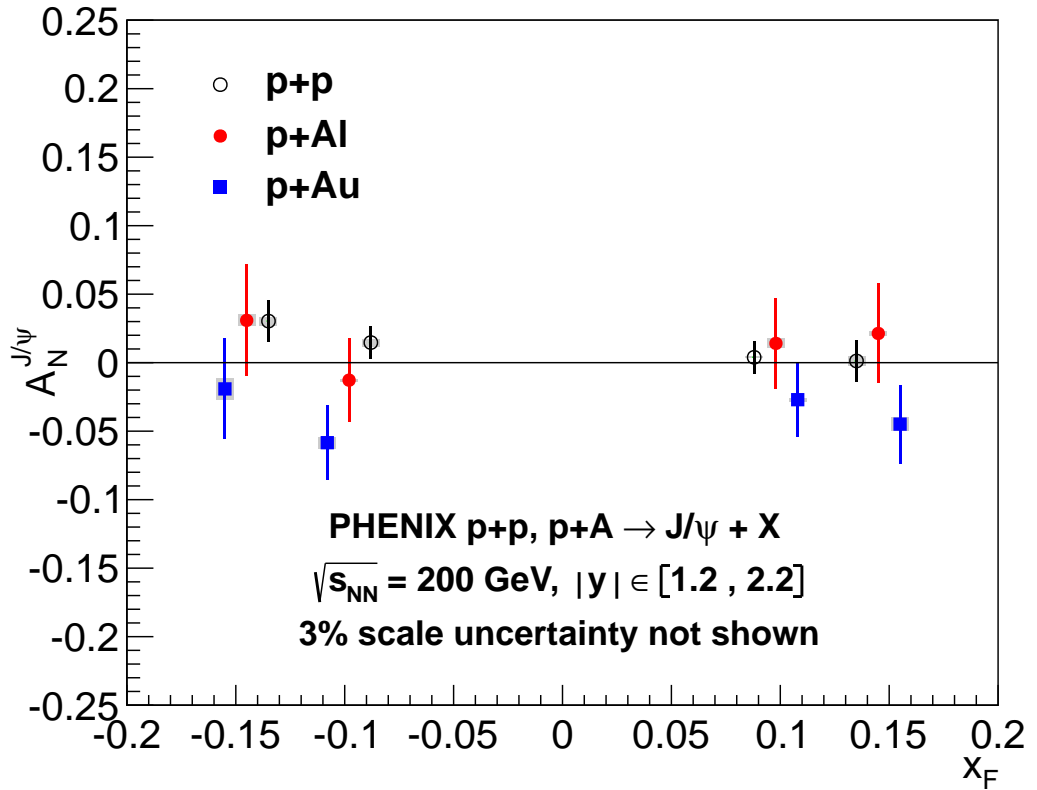


Figure 102: $A_N^{J/\psi}$ vs. x_F for the $p+p$, $p+Al$ and $p+Au$ collision data. The gray boxes show the systematic uncertainty. The value of x_F for $p+Al$ and $p+Au$ have been shifted horizontally for clarity.

Table 23: $A_N^{J/\psi}$ vs. x_F in forward and backward rapidity for $p + p$, $p + \text{Al}$ and $p + \text{Au}$ collision data.

p_T (GeV/c)	Data sample	$\langle p_T \rangle$	A_N	δA_N^{stat}	δA_N^{syst}	δA_N^{syst}
Forward ($x_F > 0$)		(GeV/c)			(source 1)	(source 2)
0.42 < p_T < 2	$p+p$	1.17	0.002	0.011	0.0006	0.0001
	$p+\text{Al}$	1.19	0.025	0.030	0.0034	0.0026
	$p+\text{Au}$	1.20	-0.067	0.025	0.0008	0.0020
2 < p_T < 10	$p+p$	3.02	0.006	0.016	0.0009	0.0041
	$p+\text{Al}$	3.07	-0.007	0.040	0.0148	0.0005
	$p+\text{Au}$	3.13	0.013	0.031	0.0045	0.0015
Backward ($x_F < 0$)						
0.42 < p_T < 2	$p+p$	1.16	0.013	0.011	0.0021	0.0002
	$p+\text{Al}$	1.18	-0.024	0.031	0.0007	0.0012
	$p+\text{Au}$	1.19	-0.074	0.029	0.0077	0.0008
2 < p_T < 10	$p+p$	3.00	0.034	0.016	0.0027	0.0015
	$p+\text{Al}$	3.03	0.050	0.041	0.0024	0.0001
	$p+\text{Au}$	3.03	0.013	0.033	0.0004	0.0004

Table 24: $A_N^{J/\psi}$ vs. x_F in forward and backward rapidity for $p+p$, $p+Al$ and $p+Au$ collision data.

x_F	Data sample	$\langle x_F \rangle$	A_N	δA_N^{stat}	δA_N^{syst}	δA_N^{syst}
				(source 1)	(source 1)	(source 2)
$0.05 < x_F < 0.11$	$p+p$	0.088	0.004	0.012	0.0001	0.0006
	$p+Al$	0.089	0.014	0.033	0.0029	0.0021
	$p+Au$	0.089	-0.027	0.027	0.0014	0.0001
$0.11 < x_F < 0.30$	$p+p$	0.135	0.001	0.015	0.0018	0.0030
	$p+Al$	0.135	0.021	0.036	0.0011	0.0013
	$p+Au$	0.136	-0.045	0.029	0.0049	0.0003
$-0.11 < x_F < -0.05$	$p+p$	-0.086	0.013	0.012	0.0026	0.0002
	$p+Al$	-0.086	-0.013	0.030	0.0007	0.0004
	$p+Au$	-0.086	-0.058	0.027	0.0040	0.0007
$-0.30 < x_F < -0.11$	$p+p$	-0.132	0.030	0.015	0.0031	0.0011
	$p+Al$	-0.132	0.031	0.041	0.0002	0.0041
	$p+Au$	-0.132	-0.019	0.037	0.0077	0.0006

the multiplicity. The multiplicity represents the impact factor for a specific event. In our analysis, the event multiplicity can be measured by the number of FVTX tracklets and the BBC centrality.

4.3.1 A_N in three and four p_T bins

In order to check whether there exist a p_T -dependent A_N , it would be helpful to make the number of p_T bin three or four rather than just two. Figures 103 and 104 show the inclusive A_N in three and four p_T bins. In the case of three p_T bins, the binning is [0 GeV, 1.2 GeV], [1.2 GeV, 2.0 GeV] and [2.0 GeV, 10 GeV]. While in the case of four p_T bins, the binning is [0 GeV, 1.0 GeV], [1.0 GeV, 1.8 GeV], [1.8 GeV, 2.8 GeV] and [2.8 GeV, 10 GeV].

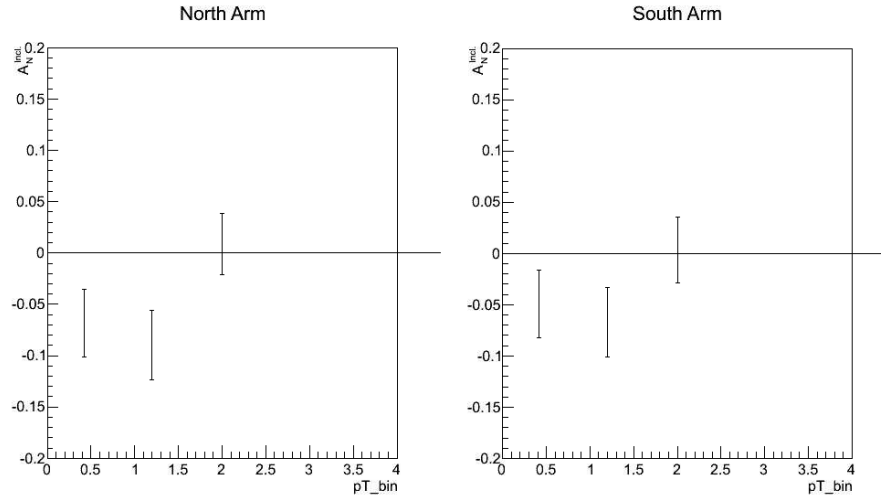


Figure 103: Inclusive A_N with three p_T bins.

From figures 103 and 104, there is no strong evidence for a p_T -dependent A_N .

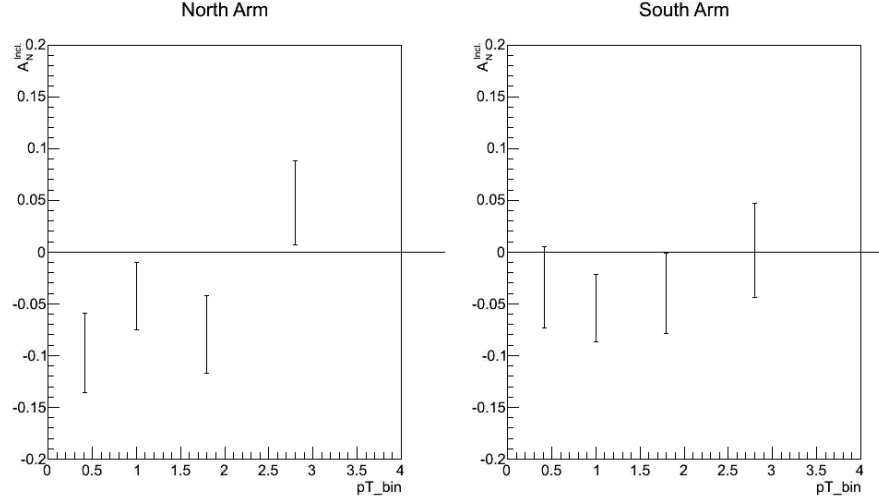


Figure 104: Inclusive A_N with four p_T bins.

The variation of A_N in each plot is consistent with statistical fluctuations.

4.3.2 A_N with binning of number of FVTX Tracklets and BBC centrality

For each dimuon that passed the dimuon event cuts, the corresponding number of FVTX Tracklets will be calculated with the data collected by the FVTX. The total number of FVTX Tracklets is already recorded in the picoDST. The FVTX Tracklets traceable to the dimuons pair, or with less than two hits in FVTX, or having FVTX $DCA_R > 1.0$, will be excluded from total number of FVTX Tracklets. Figure 105 shows the distribution of the number of FVTX Tracklets. This distribution was divided into four bins with roughly equal numbers of FVTX Tracklets. Figure 106 shows the inclusive A_N in each number of FVTX Tracklets

bins.

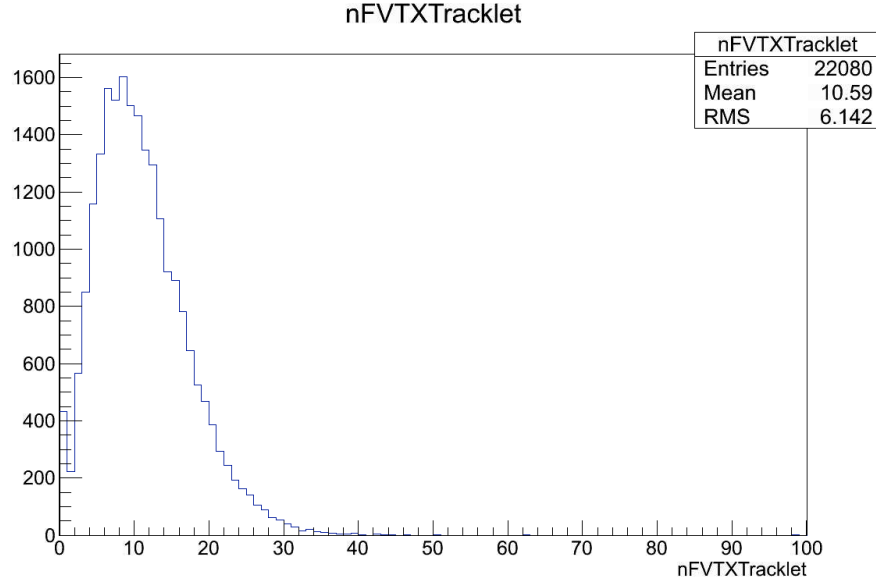


Figure 105: FVTX Tracklets distribution for the dimuons that pass the dimuon event cuts with $p + \text{Au}$ data

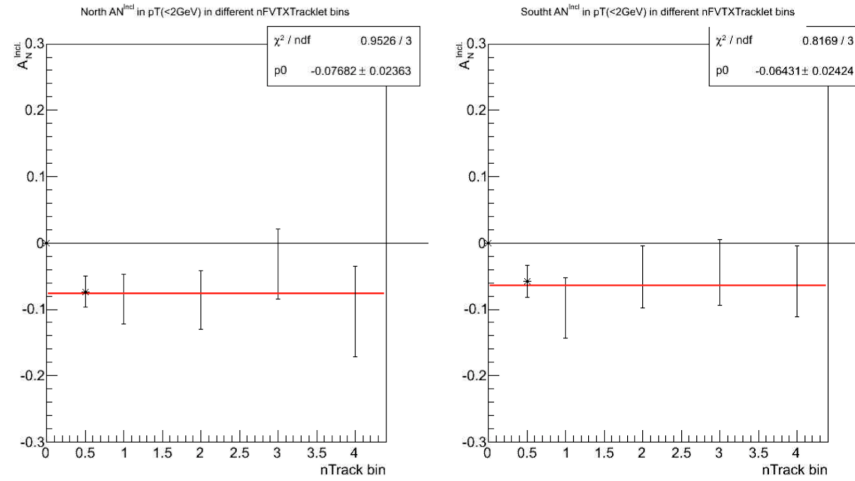


Figure 106: Inclusive A_N vs. nFVTXTracklets. The first point(star point) is the combined inclusive A_N in lower p_T bin with $p + \text{Au}$ data

Similar with number of FVTX Tracklets, THE BBC centrality distribution is obtained for the dimuons that pass the dimuon event cuts. Figure 107 is the BBC centrality distribution. This distribution was divided into four bins with roughly equal statistics.

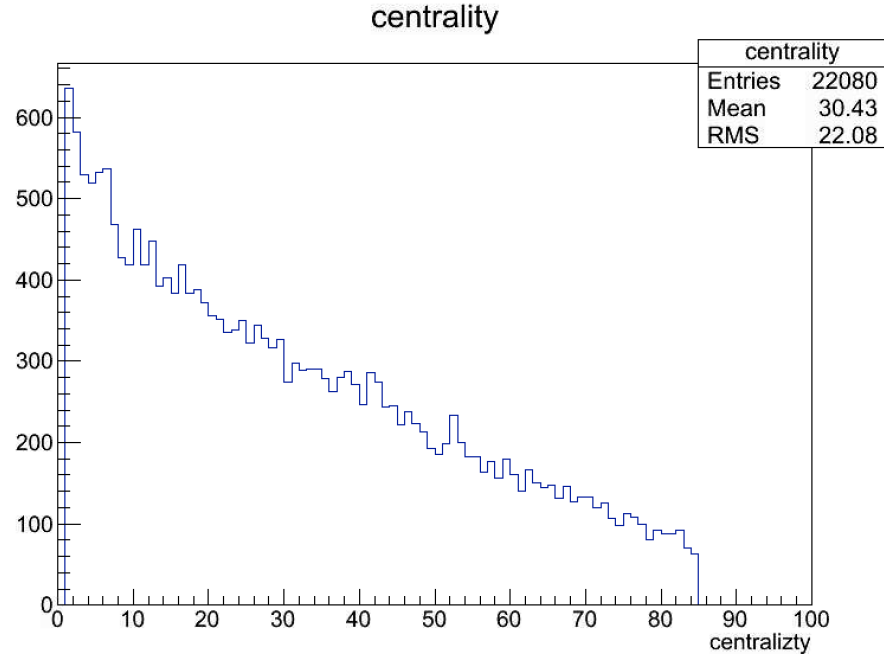


Figure 107: BBC centrality distribution for the dimuons that pass the dimuon event cuts with $p + \text{Au}$ data

Figure 108 is inclusive A_N in each BBC centrality(charge) bin. Considering that higher BBC centrality is corresponding to lower BBC charge, the BBC centrality binning in the figure is in the descending order.

Since $p + \text{Au}$ data is very statistically limited, the inclusive A_N with further

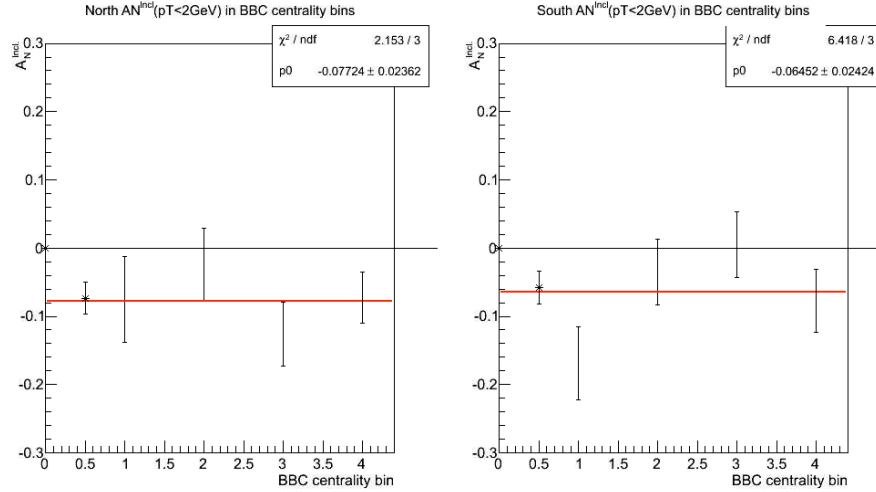


Figure 108: Inclusive A_N vs. BBC centrality. The first point (star point) is the combined inclusive A_N for the first p_T .

binning in FVTX Tracklets and centrality is consistent with each other with relatively big statistical uncertainty. We cannot find out very strong evidences to show that A_N is dependent on FVTX Tracklets or/and centrality in the $p+Au$ data.

5 Conclusion

We have reported the measurements of the transverse single-spin asymmetry in J/ψ production at forward and backward rapidity with $1.2 < |y| < 2.2$ in $p+p$, $p+Al$ and $p+Au$ collisions with transversely polarized proton beams at $\sqrt{s_{NN}} = 200$ GeV using the RHIC Run 2015 data. The results from $p + p$ collisions are consistent with previous PHENIX results. Within experimental uncertainties, the

J/ψ A_N is consistent with zero in all p_T and x_F bins in $p + \text{Al}$ collisions. For $p + \text{Au}$ collisions, the data favor negative asymmetries in all x_F bins and we have observed a non-zero A_N at the 2σ level in the lower p_T bins; however, in the higher p_T bins, it is consistent with zero. This intriguing result observed in $p + \text{Au}$ collisions could indicate possible contributions from other non-conventional mechanisms. One of the possible contributions could come from electromagnetic interactions. A recent PHENIX measurement [17] of the TSSA in forward neutron production shows that electromagnetic processes could significantly enhance A_N in $p+A$ collisions, resulting in a strong nuclear-size dependence for A_N . Further theoretical studies of A_N in J/ψ production exploring different mechanisms are needed to explain the current results.

REFERENCES

- [1] K. Abe et al. Precision determination of the neutron spin structure function $g_1(n)$. *Phys. Rev. Lett.*, 79:26–30, 1997. [,677(1997)].
- [2] K. Abe et al. Measurements of the proton and deuteron spin structure functions $g(1)$ and $g(2)$. *Phys. Rev.*, D58:112003, 1998.
- [3] B. I. Abelev et al. Forward Neutral Pion Transverse Single Spin Asymmetries in $p+p$ Collisions at $s^{**}(1/2) = 200\text{-GeV}$. *Phys. Rev. Lett.*, 101:222001, 2008.
- [4] K. Ackerstaff et al. Measurement of the neutron spin structure function $g_1(n)$ with a polarized He-3 internal target. *Phys. Lett.*, B404:383–389, 1997. [,671(1997)].
- [5] L. Adamczyk et al. Transverse Single-Spin Asymmetry and Cross-Section for π^0 and η Mesons at Large Feynman- x in Polarized $p + p$ Collisions at $\sqrt{s} = 200$ GeV. *Phys. Rev.*, D86:051101, 2012.
- [6] J. Adams et al. Cross-sections and transverse single spin asymmetries in forward neutral pion production from proton collisions at $s^{**}(1/2) = 200\text{-GeV}$. *Phys. Rev. Lett.*, 92:171801, 2004.
- [7] A. Adare et al. Measurement of Transverse Single-Spin Asymmetries for J/ψ Production in Polarized $p + p$ Collisions at $\sqrt{s} = 200$ GeV. *Phys. Rev.*, D82:112008, 2010. [Erratum: Phys. Rev.D86,099904(2012)].
- [8] A. Adare et al. Cross section and transverse single-spin asymmetry of η mesons in $p^\uparrow + p$ collisions at $\sqrt{s} = 200$ GeV at forward rapidity. *Phys. Rev.*, D90(7):072008, 2014.
- [9] A. Adare et al. Measurement of transverse-single-spin asymmetries for midrapidity and forward-rapidity production of hadrons in polarized $p+p$ collisions at $\sqrt{s} = 200$ and 62.4 GeV. *Phys. Rev.*, D90(1):012006, 2014.
- [10] K. Adcox et al. *Nuclear Instruments and Methods in Physics Research*, 499:469, 2003.
- [11] B. Adeva et al. Spin asymmetries $A(1)$ and structure functions g_1 of the proton and the deuteron from polarized high-energy muon scattering. *Phys. Rev.*, D58:112001, 1998.
- [12] B. Adeva et al. Spin asymmetries $A(1)$ of the proton and the deuteron in the low x and low Q^{**2} region from polarized high-energy muon scattering. *Phys. Rev.*, D60:072004, 1999. [Erratum: Phys. Rev.D62,079902(2000)].

- [13] S. S. Adler et al. Measurement of transverse single-spin asymmetries for mid-rapidity production of neutral pions and charged hadrons in polarized $p+p$ collisions at $s^{**}(1/2) = 200\text{-GeV}$. *Phys. Rev. Lett.*, 95:202001, 2005.
- [14] C. Adolph et al. First measurement of the Sivers asymmetry for gluons using SIDIS data. *Phys. Lett.*, B772:854–864, 2017.
- [15] E. S. Ageev et al. Spin asymmetry $A1(d)$ and the spin-dependent structure function $g1(d)$ of the deuteron at low values of x and Q^{**2} . *Phys. Lett.*, B647:330–340, 2007.
- [16] C. Aidala et al. Cross section and transverse single-spin asymmetry of muons from open heavy-flavor decays in polarized $p+p$ collisions at $\sqrt{s} = 200$ GeV. *Phys. Rev.*, D95(11):112001, 2017.
- [17] C. Aidala et al. Nuclear Dependence of the Transverse-Single-Spin Asymmetry for Forward Neutron Production in Polarized $p + A$ Collisions at $\sqrt{s_{NN}} = 200$ GeV. *Phys. Rev. Lett.*, 120(2):022001, 2018.
- [18] A. Airapetian et al. Single-spin asymmetries in semi-inclusive deep-inelastic scattering on a transversely polarized hydrogen target. *Phys. Rev. Lett.*, 94:012002, 2005.
- [19] A. Airapetian et al. Precise determination of the spin structure function $g(1)$ of the proton, deuteron and neutron. *Phys. Rev.*, D75:012007, 2007.
- [20] I. G. Alekseev et al. Analyzing power in CNI-region at AGS (experiment E950) . pages 670–673, 2000.
- [21] M. G. Alekseev et al. The Spin-dependent Structure Function of the Proton g_1^p and a Test of the Bjorken Sum Rule. *Phys. Lett.*, B690:466–472, 2010.
- [22] V. Yu. Alexakhin et al. The Deuteron Spin-dependent Structure Function $g1(d)$ and its First Moment. *Phys. Lett.*, B647:8–17, 2007.
- [23] M. Anselmino, M. Boglione, U. D’Alesio, A. Kotzinian, S. Melis, F. Murgia, A. Prokudin, and C. Turk. Sivers Effect for Pion and Kaon Production in Semi-Inclusive Deep Inelastic Scattering. *Eur. Phys. J.*, A39:89–100, 2009.
- [24] M. Anselmino, M. Boglione, U. D’Alesio, A. Kotzinian, F. Murgia, and A. Prokudin. Extracting the Sivers function from polarized SIDIS data and making predictions. *Phys. Rev.*, D72:094007, 2005. [Erratum: *Phys. Rev.* D72, 099903(2005)].

- [25] M. Anselmino, M. Boglione, U. D'Alesio, E. Leader, S. Melis, F. Murgia, and A. Prokudin. On the role of Collins effect in the single spin asymmetry A_N in $p^\uparrow p \rightarrow hX$ processes. *Phys. Rev.*, D86:074032, 2012.
- [26] M. Anselmino, M. Boglione, U. D'Alesio, S. Melis, F. Murgia, and A. Prokudin. Sivers effect and the single spin asymmetry A_N in $p^\uparrow p \rightarrow hX$ processes. *Phys. Rev.*, D88(5):054023, 2013.
- [27] P. L. Anthony et al. Deep inelastic scattering of polarized electrons by polarized He-3 and the study of the neutron spin structure. *Phys. Rev.*, D54:6620–6650, 1996.
- [28] P. L. Anthony et al. Measurement of the deuteron spin structure function $g_1(d)(x)$ for $1-(\text{GeV}/c)^{**2} \leq Q^{**2} \leq 40-(\text{GeV}/c)^{**2}$. *Phys. Lett.*, B463:339–345, 1999.
- [29] P. L. Anthony et al. Measurements of the Q^{**2} dependence of the proton and neutron spin structure functions $g(1)^{**p}$ and $g(1)^{**n}$. *Phys. Lett.*, B493:19–28, 2000.
- [30] I. Arsene et al. Single Transverse Spin Asymmetries of Identified Charged Hadrons in Polarized $p+p$ Collisions at $s^{**}(1/2) = 62.4\text{-GeV}$. *Phys. Rev. Lett.*, 101:042001, 2008.
- [31] Elke-Caroline Aschenauer et al. The RHIC SPIN Program: Achievements and Future Opportunities. 2015.
- [32] V. Bargmann, Louis Michel, and V. L. Telegdi. Precession of the polarization of particles moving in a homogeneous electromagnetic field. *Phys. Rev. Lett.*, 2:435–436, May 1959.
- [33] V. Barone and P. G. Ratcliffe. Heavy Flavour production as probe of Gluon Sivers Function. *World Scientific*, 2003.
- [34] V. Barone and P.G. Ratcliffe. *Transverse Spin Physics*. World Scientific, 2003.
- [35] J. Beringer et al. Review of Particle Physics (RPP). *Phys. Rev.*, D86:010001, 2012.
- [36] Daniel Boer, P. J. Mulders, and F. Pijlman. Universality of T odd effects in single spin and azimuthal asymmetries. *Nucl. Phys.*, B667:201–241, 2003.
- [37] V. M. Braun, A. N. Manashov, and B. Pirnay. Scale dependence of twist-three contributions to single spin asymmetries. *Phys. Rev.*, D80:114002, 2009. [Erratum: *Phys. Rev.* D86, 119902(2012)].

- [38] S. Chekanov et al. A ZEUS next-to-leading-order QCD analysis of data on deep inelastic scattering. *Phys. Rev.*, D67:012007, 2003.
- [39] J. C. Collins, A. V. Efremov, K. Goeke, S. Menzel, A. Metz, and P. Schweitzer. Sivers effect in semi-inclusive deeply inelastic scattering. *Phys. Rev.*, D73:014021, 2006.
- [40] John C. Collins. Fragmentation of transversely polarized quarks probed in transverse momentum distributions. *Nucl. Phys.*, B396:161–182, 1993.
- [41] John C. Collins, Davison E. Soper, and George F. Sterman. Transverse Momentum Distribution in Drell-Yan Pair and W and Z Boson Production. *Nucl. Phys.*, B250:199–224, 1985.
- [42] James Currie, Aude Gehrmann-De Ridder, E. W. N. Glover, and Joao Pires. NNLO QCD corrections to jet production at hadron colliders from gluon scattering. *JHEP*, 01:110, 2014.
- [43] U. D'Alesio and F. Murgia. Azimuthal and Single Spin Asymmetries in Hard Scattering Processes. *Prog. Part. Nucl. Phys.*, 61:394–454, 2008.
- [44] U. D'Alesio, F. Murgia, and C. Pisano. Towards a first estimate of the gluon Sivers function from A_N data in pp collisions at RHIC. *JHEP*, 09:119, 2015.
- [45] Ya. S. Derbenev, A. M. Kondratenko, S. I. Serednyakov, A. N. Skrinsky, G. M. Tumaikin, and Yu. M. Shatunov. RADIATIVE POLARIZATION: OBTAINING, CONTROL, USING. *Part. Accel.*, 8:115–126, 1978.
- [46] A. V. Efremov and O. V. Teryaev. QCD Asymmetry and Polarized Hadron Structure Functions. *Phys. Lett.*, B150:383, 1985.
- [47] K. O. Eyser et al. Absolute polarization measurements at RHIC in the Coulomb nuclear interference region. *AIP Conf. Proc.*, 915:916–919, 2007. [,916(2006)].
- [48] Marcel Froissart and Raymond Stora. Depolarisation d'un faisceau de protons polarisés dans un synchrotron. *Nuclear Instruments and Methods*, 7:297 – 305, 1960.
- [49] Francois Gelis, Edmond Iancu, Jamal Jalilian-Marian, and Raju Venugopalan. The Color Glass Condensate. *Ann. Rev. Nucl. Part. Sci.*, 60:463–489, 2010.
- [50] Murray Gell-Mann. A Schematic Model of Baryons and Mesons. *Phys. Lett.*, 8:214–215, 1964.

- [51] Rohini M. Godbole, Abhiram Kaushik, Anuradha Misra, Vaibhav Rawoot, and Bipin Sonawane. Heavy Flavour production as probe of Gluon Sivers Function. *Few Body Syst.*, 58(2):96, 2017.
- [52] Rohini M. Godbole, Abhiram Kaushik, Anuradha Misra, Vaibhav Rawoot, and Bipin Sonawane. Transverse Single Spin Asymmetry in $p+p^\uparrow \rightarrow J/\psi + X$. 2017.
- [53] Jeff Greensite. An introduction to the confinement problem. *Lect. Notes Phys.*, 821:1–211, 2011.
- [54] David J. Gross and Frank Wilczek. Ultraviolet Behavior of Nonabelian Gauge Theories. *Phys. Rev. Lett.*, 30:1343–1346, 1973. [,271(1973)].
- [55] R.L. Jaffe and Aneesh Manohar. The g1 problem: Deep inelastic electron scattering and the spin of the proton. *Nuclear Physics B*, 337:509 – 546, 1990.
- [56] Xiang-Dong Ji. Gauge-Invariant Decomposition of Nucleon Spin. *Phys. Rev. Lett.*, 78:610–613, 1997.
- [57] O. Jinnouchi et al. Measurement of the analyzing power of proton-carbon elastic scattering in the CNI region at RHIC. In *Spin physics. Polarized electron sources and polarimeters. Proceedings, 16th International Symposium, SPIN 2004, Trieste, Italy, October 10-16, 2004, and Workshop, PESP 2004, Mainz, Germany, October 7-9, 2004*, pages 515–518, 2004.
- [58] Gordon L. Kane, J. Pumplin, and W. Repko. Transverse Quark Polarization in Large p(T) Reactions, e+ e- Jets, and Leptoproduction: A Test of QCD. *Phys. Rev. Lett.*, 41:1689, 1978.
- [59] Zhong-Bo Kang and Jian-Wei Qiu. Single transverse-spin asymmetry for D-meson production in semi-inclusive deep inelastic scattering. *Phys. Rev.*, D78:034005, 2008.
- [60] Zhong-Bo Kang and Jian-Wei Qiu. Evolution of twist-3 multi-parton correlation functions relevant to single transverse-spin asymmetry. *Phys. Rev.*, D79:016003, 2009.
- [61] Zhong-Bo Kang, Jian-Wei Qiu, and Hong Zhang. Quark-gluon correlation functions relevant to single transverse spin asymmetries. *Phys. Rev.*, D81:114030, 2010.
- [62] Zhong-Bo Kang, Feng Yuan, and Jian Zhou. Twist-three fragmentation function contribution to the single spin asymmetry in p p collisions. *Phys. Lett.*, B691:243–248, 2010.

- [63] R. D. Klem, J. E. Bowers, H. W. Courant, H. Kagan, M. L. Marshak, E. A. Peterson, K. Ruddick, W. H. Dragoset, and J. B. Roberts. Measurement of Asymmetries of Inclusive Pion Production in Proton Proton Interactions at 6-GeV/c and 11.8-GeV/c. *Phys. Rev. Lett.*, 36:929–931, 1976.
- [64] Larry D. McLerran and Raju Venugopalan. Computing quark and gluon distribution functions for very large nuclei. *Phys. Rev.*, D49:2233–2241, 1994.
- [65] Asmita Mukherjee and Sangem Rajesh. J/ψ Production in Polarized and Unpolarized ep Collision and Sivers and $\cos(2\phi)$ Asymmetries. 2016.
- [66] H. Okada et al. Measurement of the analyzing power $A(N)$ in pp elastic scattering in the CNI region with a polarized atomic hydrogen gas jet target. 2006.
- [67] H. Okada et al. Measurement of the analyzing power in pp elastic scattering in the peak CNI region at RHIC. *Phys. Lett.*, B638:450–454, 2006.
- [68] Jian-wei Qiu and George F. Sterman. Single transverse spin asymmetries. *Phys. Rev. Lett.*, 67:2264–2267, 1991.
- [69] Jian-wei Qiu and George F. Sterman. Single transverse spin asymmetries in direct photon production. *Nucl. Phys.*, B378:52–78, 1992.
- [70] Jian-wei Qiu and Ivan Vitev. Coherent QCD multiple scattering in proton-nucleus collisions. *Phys. Lett.*, B632:507–511, 2006.
- [71] Jianwei Qiu and George Sterman. Single transverse-spin asymmetries in hadronic pion production. *Phys. Rev. D*, 59:014004, Nov 1998.
- [72] C. E. Rasmussen and C. K. I. C. K. I. Williams. *Gaussian Processes for Machine Learning*. MIT Press, 2006.
- [73] Andreas Schfer and Jian Zhou. Color entanglement for -jet production in polarized pA collisions. *Phys. Rev.*, D90(9):094012, 2014.
- [74] Andreas Schfer and Jian Zhou. Transverse single spin asymmetry in direct photon production in polarized pA collisions. *Phys. Rev.*, D90(3):034016, 2014.
- [75] Dennis W. Sivers. Single Spin Production Asymmetries from the Hard Scattering of Point-Like Constituents. *Phys. Rev.*, D41:83, 1990.
- [76] Dennis W. Sivers. Hard scattering scaling laws for single spin production asymmetries. *Phys. Rev.*, D43:261–263, 1991.

- [77] T. Skwarnicki. *A study of the radiative CASCADE transitions between the Upsilon-Prime and Upsilon resonances*. PhD thesis, Cracow, INP, 1986.
- [78] Werner Vogelsang and Feng Yuan. Single-transverse spin asymmetries: From DIS to hadronic collisions. *Phys. Rev.*, D72:054028, 2005.
- [79] A. Zelenski et al. Absolute polarized H-jet polarimeter development, for RHIC. *Nucl. Instrum. Meth.*, A536:248–254, 2005.
- [80] X. Zheng et al. Precision measurement of the neutron spin asymmetries and spin-dependent structure functions in the valence quark region. *Phys. Rev.*, C70:065207, 2004.
- [81] Jian Zhou. Color entanglement like effect in collinear twist-3 factorization. *Phys. Rev.*, D96(11):114001, 2017.
- [82] Jian Zhou. Single spin asymmetries in forward p-p/A collisions revisited: the role of color entanglement. *Phys. Rev.*, D96(3):034027, 2017.